

DAAB07-82-J009  
SUBTASK 157

(2)

FINAL REPORT

AD-A166 767

STATISTICAL ANALYSES OF DUAL-BAND  
INFRARED CLOUD IMAGERY

FEBRUARY 1984

DTIC  
ELECTED  
APR 10 1986  
S A / D  
D

DISTRIBUTION STATEMENT A  
Approved for public release;  
Distribution Unlimited

[Redacted]

[Redacted]

TELEDYNE  
BROWN ENGINEERING

Cummings Research Park • Huntsville, Alabama 35807

DTIC FILE COPY

86 4 9 110

**Best  
Available  
Copy**

## ABSTRACT

A dual-band comparison in the SWIR and LWIR atmospheric windows was made of the spatial, temporal, and radiometric statistics of clouds as observed by the Ground Based Measurements (GBM) Sensor of the Army Optical Station (AOS). The existence of the GBM archives has provided a unique opportunity to analyze the properties of cloud images simultaneously observed in the 3-5 and the 8-12 micron passbands. It is shown that the level of correlation in clutter between the two passbands is a strong function of the meteorological conditions. Through observations of reentry vehicles passing behind clouds, point measurements of the attenuation of target signatures have been achieved.

*Keywords: recording Systems; cross correlation;  
data acquisition*

Accesion For	
NTIS	CRA&I
DTIC	TAB
Unannounced	
Justification	
By <u>ltr. on file</u>	
Distribution /	
Availability Codes	
Dist	Avail and/or Special
A-1	



TABLE OF CONTENTS

	Page
1. INTRODUCTION . . . . .	1-1
1.1 Task Summary . . . . .	1-1
1.2 Synopsis of Report . . . . .	1-1
2. GBM SENSORS AND DATA BASE . . . . .	2-1
2.1 GBM Sensor System . . . . .	2-1
2.2 GBM Data Recording . . . . .	2-5
2.2.1 Analog Recorders . . . . .	2-5
2.2.2 Video Recorders . . . . .	2-7
2.2.3 Film Camera . . . . .	2-7
2.3 Meteorological Instrumentation. . . . .	2-8
3. THEORY OF STATISTICAL ANALYSIS . . . . .	3-1
3.1 Means and Variances . . . . .	3-1
3.2 Cross-Correlations . . . . .	3-1
3.3 Spectral Densities and Cross-Spectra. . . . .	3-2
3.4 Level of Significance . . . . .	3-2
3.5 Apodization . . . . .	3-3
4. RESULTS OF COMPARATIVE ANALYSIS. . . . .	4-1
4.1 Original Cloud Scene Data . . . . .	4-1
4.2 Cross-Correlations . . . . .	4-1
4.3 Power Spectral Densities and Cross-Spectra . . . . .	4-10
4.4 Estimation of Cloud Transmission Profiles . . . . .	4-1+
5. CLOUD SCENE SYNTHESIS . . . . .	5-1
5.1 Image Model . . . . .	5-1
5.2 Image Analysis. . . . .	5-2
5.3 Image Synthesis . . . . .	5-3
5.4 Temporal Propagation. . . . .	5-6

TABLE OF CONTENTS (CONCLUDED)

	Page
REFERENCES . . . . .	R-1
APPENDIX A. DATA REDUCTION . . . . .	A-1
APPENDIX B. CALIBRATION . . . . .	B-1
APPENDIX C. METEOROLOGY . . . . .	C-1
APPENDIX D. GEOMETRY. . . . .	D-1

## 1. INTRODUCTION

### 1.1 TASK SUMMARY

This report is submitted to Night Vision and Electro-Optical Laboratories as the final report for Contract Number DAAB07-82-D-J009, Subtask 157. A comparative analysis was performed to determine the level of correlation in radiometric signature that exists for clouds simultaneously observed in the LWIR and the SWIR atmospheric passbands. This comparative study was performed on nine missions of the GBM Archives (Refer to Table 2-4 of Section 2 of this report), which is the cloud data processed for Task I. From this analysis, it has been shown that in these cases clouds act as emitters in the LWIR and as scatterers in the SWIR. It was also shown that the level of correlation between passbands is a strong function of weather conditions.

A summary of the total task being performed by Teledyne Brown Engineering (TBE) in this effort is presented here to provide an understanding of the intended use of this information. This effort is divided into five tasks, and these tasks have subsequently been grouped into two phases. Phase I (Tasks I and IV) was to determine the extent of dual-band cloud data accessible from the GBM archives and to perform sufficient analysis on these data to show the level of correlation (if any) between the LWIR and SWIR passbands. Phase II (Task II, III, and V) will be a continuation of this analysis on additional cases, the development of a technique for the conversion of these data into a form comparable to a FLIR image and ultimately the development of a wide-field-of-view, dual-band cloud scene based on this statistical analysis on the GBM cloud data.

### 1.2 SYNOPSIS OF REPORT

Section 2 of this report gives a description of the GBM Data Base and the extent of cloud data it contains. Since several sensors were involved in data collection, they are also described in this

section. Section 3 is a detailed discussion of the theory of statistical analysis as incorporated in this study. Included in this section are the definitions of the statistical tools used in this study, and a discussion of the choice of the cosine roll-off apodization function applied to the raw data stream before Fourier analysis. The final choice of the 30-point cosine roll-off is shown as a compromise between high-frequency aliasing and signal amplitude error. Section 4 contains the results of the comparative analysis and a discussion of the potential use of the reentry vehicle as a calibrated source for the determination of cloud transmission profiles. Section 5 describes the cloud scene generation model developed by TBE for Night Vision and Electro-Optics Laboratories and suggests a method for the temporal propagation of simulated cloud scenes.

Appendix A of this report describes the procedure used to reduce the raw PCM data and to convert it to a digital form. This technique was originally created to reduce reentry vehicle target data but is compatible with the reduction of cloud data. Appendix B discusses the procedure for calibration of the GBM sensor during mission recording, and describes the measures taken to ensure an accurate calibration standard. Appendix C describes the extent of the supporting meteorological data obtained during the radiosonde balloon flights at the time of each GBM mission and provides temperature and dew point profiles for each of the missions listed in Table I. This appendix also describes a method for approximating the observed cloud ranges based on these profiles. Appendix D contains polar plots of the boresight tracking and Sun position for the above-mentioned missions.

## 2. GBM SENSORS AND DATA BASE

### 2.1 GBM SENSOR SYSTEM

The Ground Based Measurements (GBM) Sensor System is a passive, two-color infrared optical scanning and tracking sensor mounted on a modified NIKE-AJAX azimuth-elevation tracking pedestal. The system is located at the Army Optical Station (AOS) on Roi Namur (Figure 2-1) in the Kwajalein Atoll. The system's purpose is to obtain high-resolution infrared signatures and other temporal and spatial characteristics of reentry targets which terminate at the Kwajalein impact area.

The GBM pointing and tracking system was designed to operate in any of several modes:

- Radar command
- TV auto-track
- GBM infrared auto-track
- Manual track
- Trajectory retrace
- Console control.

These modes can be selected by means of a track-mode switch on the Operations Console.

The sensors, optics, and servo-drives are located on the tracking pedestal in the dome of the AOS building shown. The Operations Console and other electronics are located in a 34-ft instrument van.

The focal plane of the GBM sensor contains two staggered line arrays of mercury-doped, germanium detectors, which are cooled by a closed-cycle, gaseous-helium system. The two infrared bandpasses are obtained by filtering each array to a different bandpass. The system relative response for each waveband is provided in a separate document. Figure 2-2 shows the NEFD of each GBM passband as a function of focal plane irradiance. There are 31 detectors for LWIR and 21 for SWIR. Figure 2-3 displays the geometry of the two arrays. The sensor employs a dither mirror scanning bidirectionally at a rate of 15 Hz. Each detector is sampled at a rate of 25 kHz; voltages are subsequently digitized and encoded for recording. Characteristics of the GBM sensor are

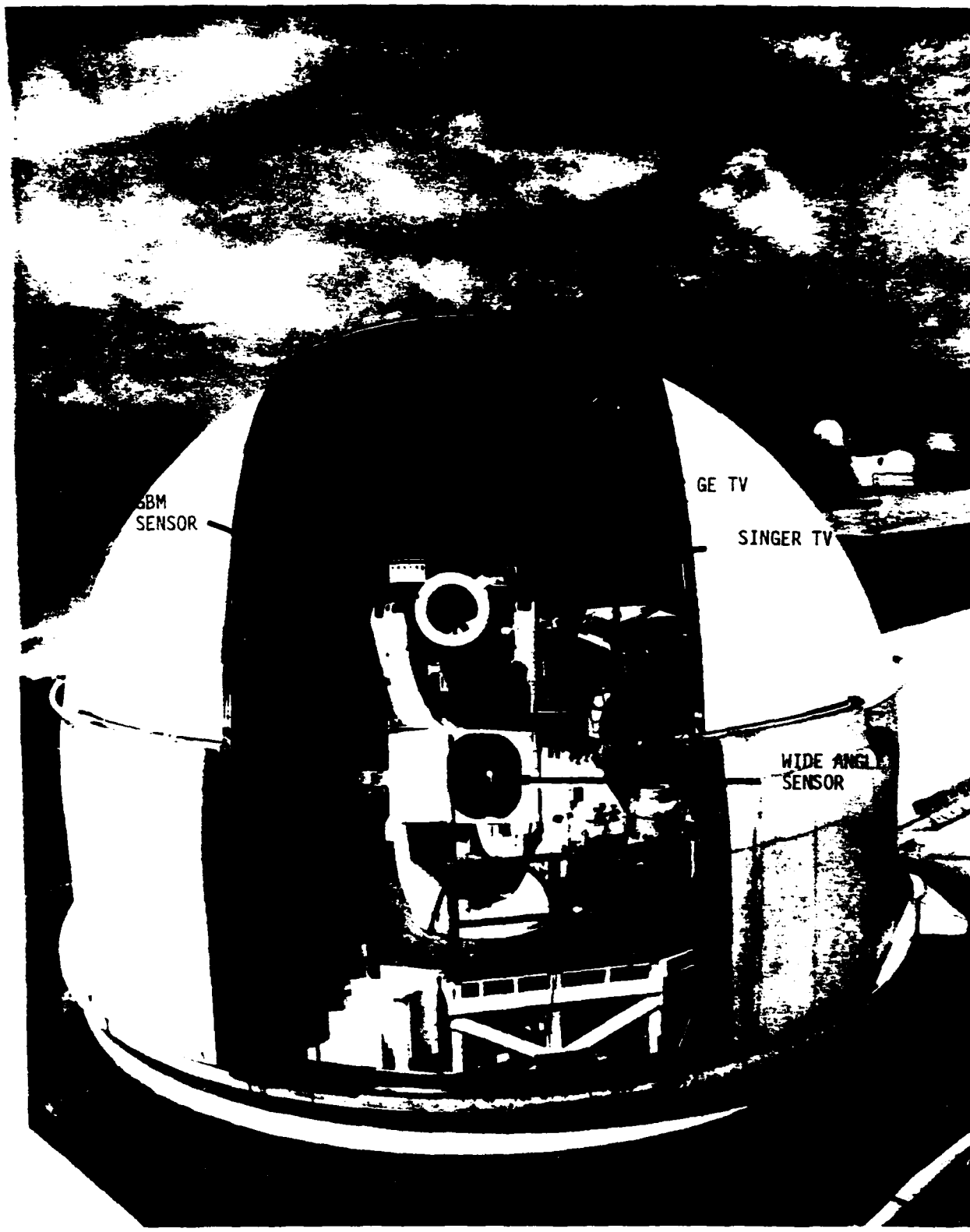


FIGURE 2-1. ARMY OPTICAL STATION, ROI NAMUR, KWAJALEIN ATOLL

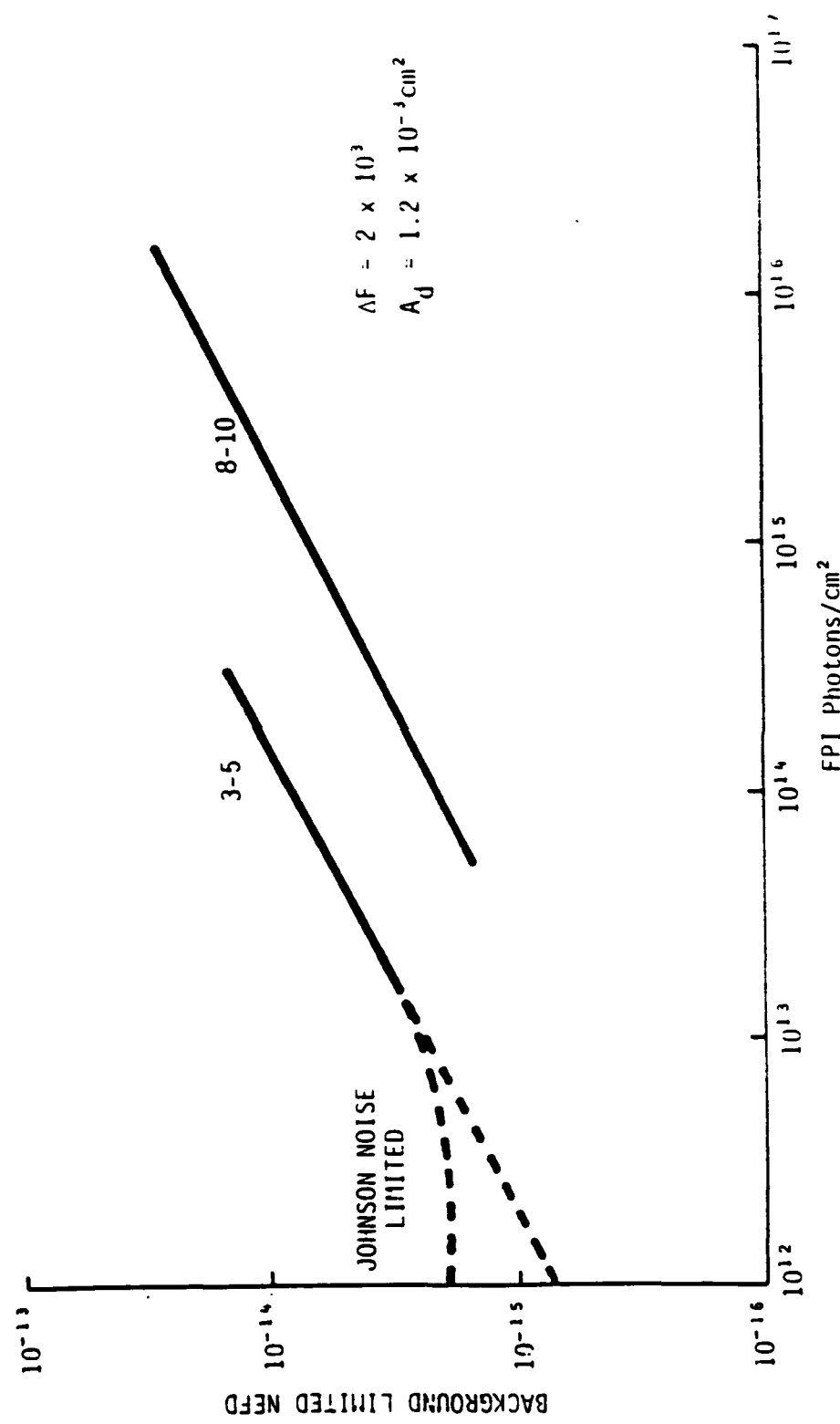


FIGURE 2-2. GBM 11 NEFD VERSUS FOCAL PLANE IRRADIANCE

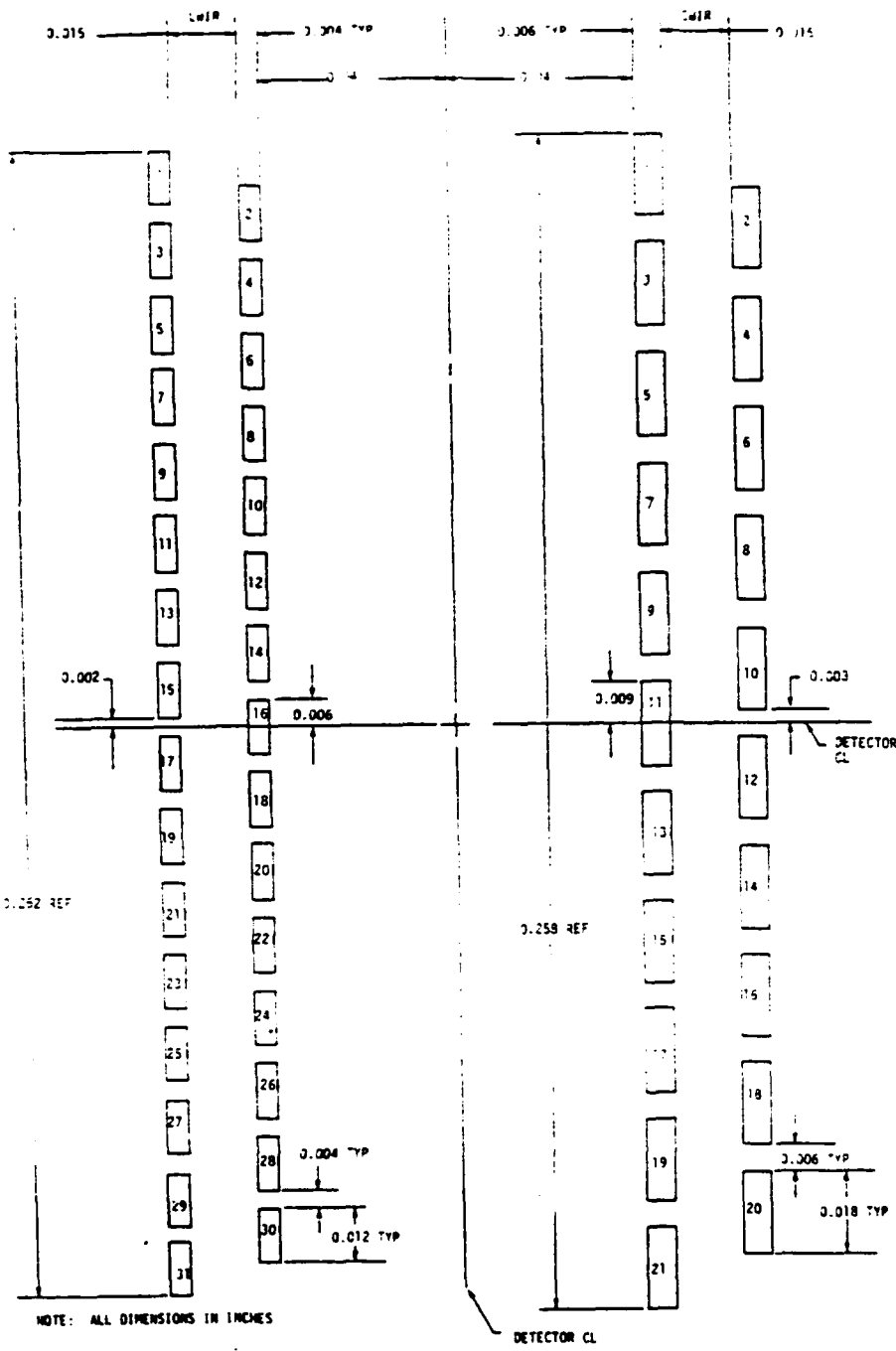


FIGURE 2-3. GBM FOCAL PLANE GEOMETRY

presented in Table 2-I. The GBM sensor focal length is estimated on the basis of initial measurements made at AOS.

TABLE 2-I. AOS SENSOR CHARACTERISTICS

	FRAME RATE (frames/sec)	FOCAL RATIO	FOCAL LENGTH (mm)	TIMING	FIELD OF VIEW (mrad)
GBM Sensor	30 scans FOV/sec	f/6.9	3,160	IRIG B IRIG A	2.2 by 5.3
GBM LLL TV	60	f/2.8	215	GMT	70, diagonal
35-mm Camera	10	f/3.7	150	IRIG B	120 by 168

## 2.2 GBM DATA RECORDING

The GBM system records data using analog recorders, video recorders, and film cameras.

### 2.2.1 Analog Recorders

The digital signal outputs for each color band are independently recorded on two Bell and Howell 14-track VR3700B tape recorders with Bell and Howell's enhanced NRZ electronics for the PCM channels. The GBM channel assignment is shown in Table 2-II. Channels 3 and 5 are used to record the prime detector data. These data consist of sampled detector outputs that have been converted 8-bit digital words. Two such data streams, and hence two recorder channels, are necessary to record all of the detector outputs and still remain below the bit rate capacity (4 Mbps at 120 ips) of the recorder.

Both PCM data channels contain a series of 29 eight-bit data words, totalling 232 bits. Three of the 29 words are sync words. The channel 3 sync word is 0000 0101 0000 11000 1101 1111. The channel 5 sync word is the ones complement of the channel 3 sync word. The first of the 26 data words for channel 3 is the output from detector A4,

TABLE C-10. GBM ANALOG RECORDER CHANNEL ASSIGNMENTS

TRACK	DATA DESCRIPTION	RECORDING MODE
Edge	Reserved for Voice A	Direct
1	Scanning Secondary Mirror Position Analog Voltage	FM WB Group II
2	Spare	TBD
3	GBM Long-Wavelength PCM Radiometric	PCM Enhanced NRZ
4	Spare	TBD
5	GBM Long-and Short-Wavelength PCM Radiometric	PCM Enhanced NRZ
6	Composite Clock (15 Hz and 15 kHz)	FM WB Group II
7	IRIG-B Time (Modified)	FM WB Group II
8	Spare	TBD
9	IRIG-A Time (Modified)	FM WB Group II
10	Spare	TBD
11	GBM Housekeeping	FM-PCM
12	Tape Servo	Direct, WB Option B
13	DC Voltage Levels, Long-Wavelength	FM WB Group II
14	DC Voltage Levels, Short-Wavelength	FM WB Group II
Edge	Voice B	Direct

and the last is A29. The channel 5 data words actually begin with the output from detectors A1, A2, and A3, then include B1 through B21, and end with A30 and A31. The PCM bit rate is 3.48 Mbps.

A time reference is provided by FM-recording IRIG-B time on channel 7 and IRIG-A time on channel 9. The IRIG-B time code contains 100 pulses per second with a carrier frequency of 1 kHz; IRIG-A contains 1,000 pulses per second with a carrier frequency of 10 kHz.

The housekeeping data are FM-recorded in PCM format on channel 11 and consist of 44 eight-bit words at a bit rate of approximately 28.16 kbps. Included is such information as the secondary scanning mirror position, pedestal azimuth and elevation position, digitized analog status signals, and digital status signals. In addition, there is a composite 15-Hz/15-kHz clock recorded on channel 6. A frequency used in tape servo compensation is direct-recorded on channel 12.

### 2.2.2 Video Recorders

The second recording subsystem consists of three IVC Model 800 video recorders which record the display from the GBM LLL TV camera attached to the GBM sensor telescope mount and boresighted with the infrared sensor, a scan-converted display of both infrared bands from the GBM sensor, and other TV signals that are displayed on the control console monitors.

The video recorders serve two main purposes. The first is to help document the conditions under which the data were taken. The second is to aid in selecting and editing the data to be formatted. Because of the large amount of recorded material obtained during a mission, editing is necessary to minimize the amount of data formatted and to time-correlate significant events.

### 2.2.3 Film Camera

Besides the video recorders, a 35-mm motion picture camera is boresighted with the sensor for additional optical recording. Characteristics of the TV and 35-mm cameras are presented in Table 2-1.

### 2.3 METEOROLOGICAL INSTRUMENTATION

The GBM Archives includes recordings of the reentry of various strategic warheads and their associated objects. These data were simultaneously recorded with several measurement instruments including radar, LLL TV, 35-mm camera, and the GBM dual-band IR sensor, which also provides for visual interpretation of clouds. In addition to direct measurements of the vehicle, atmospheric conditions during the time of reentry were measured at ground level and with radiosonde balloon flights. In most cases, the instrumentation was turned on for test runs (called nominal runs) and for calibration. During these periods, cloud data were recorded without the presence of the reentry vehicle in the FOV. The missions cover a wide variety of climatic conditions from clear sky to heavy overcast and raining. The missions are split approximately equally into day and night runs, with the average mission length at about 4 minutes.

Table 2-III gives a summary of the extent of cloud information and the respective cloud types in each mission. The column labeled Scan Conv refers to the Scan Converter for the GBM sensor and not to the GBM sensor data itself. Every mission listed in this table includes the GBM dual IR data in PCM tape format.

Table 2-IV shows the GBM missions as they appear with respect to Sun position: the boxed case numbers are those chosen for further analysis and subsequent modeling with the Extended FOV Cloud Scene Generator. These missions were chosen to maximize the variation in time of day and Sun position, and they cover a variety of climatic conditions. It is noted that a severe limitation of this data set for ground-based analysis is its maritime characteristics. As will be shown, the water vapor content significantly reduced the SWIR transmission in all but Case 60.

The designation of front-lit, side-lit, and back-lit clouds is defined as shown in Figure 2-4, in which Sun rays entering within 60 deg of the sensor boresight produce back-lit clouds; Sun rays entering between 60 and 120 deg produce side-lit clouds, and 120 to 180 deg

TABLE 2-111. INDEX OF CLOUD DATA IN GBM ARCHIVES (sheet 1 of 5)

EGEND

CLOUD INFORMATION: (1) CLEAR  
ALTITUDE: (2) HIGH CLOUDS, (3) MEDIUM CLOUDS, (4) LOW CLOUDS  
DENSITY: (5) HEAVY OVERCAST, (6) MEDIUM OVERCAST, (7) LIGHT OVERCAST  
TYPE: (8) CIRRUS, (9) CUMULUS, (10) STRATUS, (11) BROKEN CLOUDS  
(12) CLOUD TYPE, ALTITUDE, AND COVERAGE WAS NOT DETERMINED

WAS TV



TABLE 2-111. CLOUD DATA IN GBM ARCHIVES (Sheet 3 of 5)

ELEM

CLOUD INFORMATION: (1) CLEAR  
AT ALTITUDE: (2) HIGH CLOUDS (3) MEDIUM CLOUDS (4) LOW CLOUDS

**DENSITY:** (5) HEAVY OVERCAST, (6) MEDIUM OVERCAST, (7) LIGHT OVERCAST  
**WIND DIRECTION:** (2) HIGH CLOUDS; (3) MEDIUM CLOUDS; (4) LOW CLOUDS

TYPE: (8) CIRRUS, (9) CIRROSTRATUS, (10) STRATUS, (11) BROKEN CLOUDS

(12) CLOUD TYPE, ALTITUDE, AND CONTRAGE WAS NOT DETERMINED

WAS IV

TABLE 2-III. INITIAL (0) CLOUD DATA IN IBM ARCHIVES (Sheet 4 of 5)

NUMBER	SCANNING		COVERER		WEATHER		REC'D DAY		TIME OF DAY		FILM		INFORMATION			
	SINGLES	TV	COLOR	TV	MFOU	NFOU	WFOU	MFOU	WFOU	NFOU	WFOU	MFOU	TYPE	VISITABLE	DESCRIBE	CLINFO
37	X	X	X	X	X	X	4:05	N	1	CO <sub>2</sub>						
38	X	X	X	X	X	X	4:40	N	6.15	Mission Nominal	X					
39	X	X	X	X	X	X	3:25	N								
40	X	X	X	X	X	X	3:30	D	11		X					
41	X	X	X	X	X	X	3:40	D	4.7		X					
42	X	X	X	X	X	X	3:45	N	7.15	25%	X					
43	X	X	X	X	X	X	4:05	D	7	10%	X					
44	X	X	X	X	X	X	4:05	D	7	10%	X					
45	X	X	X	X	X	X	3:50	N	4.6	20%	X					
46	X	X	X	X	X	X	4:35	D	2,3,4,5	70%	X					
47	X	X	X	X	X	X	3:25	D	4.11		X					
48	X	X	X	X	X	X	3:50	N	2,3,6,11	40%	X					
							2:30	N	12	30%	X					
							3:40	N	5,15		X					

FFEND

CONFIDENTIAL INFORMATION: (1) CLE

AN ATTITUDE: (2) HIGH CLOUDS (3) MEDIUM CLOUDS (4) LOW CLOUDS

DENSITY: (5) HEAVY OVERCAST (6) MEDIUM OVERCAST (7) LIGHT OVERCAST

(TYPE: (8) CIEBRIIS (9) CHINNIS (10) STRAUNIS (11) BROKEN CLOUDS

111 SIGHTS AND SOUNDS IN THE BIRDS OF THE WORLD

MAC TV

TABLE 2-III. CLOUD DATA IN IBM ARCHIVES (Sheet 5 of 5)

NUMBER	SCM COMPETE <sup>GE-L3-TV</sup>		SCM COMPETE <sup>GE-L3-TV</sup>		SCM COMPETE <sup>GE-L3-TV</sup>		SCM COMPETE <sup>GE-L3-TV</sup>		SCM COMPETE <sup>GE-L3-TV</sup>		SCM COMPETE <sup>GE-L3-TV</sup>	
	STINGER L3-TV	COL-OP	WEATHER	RECORDUATION	TIME OF DAY	VISIBILITY	RECORDUATION	TIME OF DAY	VISIBILITY	RECORDUATION	TIME OF DAY	VISIBILITY
49	X	X	X	X	3:50	D	4,7		X	X		
50	X	X	X	X	~3:30	N	12	80%	X	X		
51	X	X	X	X	~3:30	D	2,4,8,11	30%	X	X		
52	X	X	X	X	~3:30	N	3,6,14	30%	X	X		
53	X	X	X	X	3:25	N	12		X	X		
54	X	X	X	X	3:30	N	2,3,4,11	30%	X	X		
55	X	X	X	X	7:00	N	7		X	X		
56	X	X	X	X	3:40	D	2,11		X	X		
57	X	X	X	X	3:30	N	12					
58	X		X	X	3:25	D	2,9					
59	X	X	X	X	3:30	N	3	60%	X	X		
60	X		X	X	1:50	D	3,6	50%	X	X		

EEND

CLOUD INFORMATION: (1) CLEAR  
ALTITUDE: (2) HIGH CLOUDS, (3) MEDIUM CLOUDS, (4) LOW CLOUDS  
DENSITY: (5) HEAVY OVERCAST, (6) MEDIUM OVERCAST, (7) LIGHT OVERCAST  
TYPE: (8) CIRRUS, (9) CUMULUS, (10) STRATUS, (11) BROKEN CLOUDS  
(12) CLOUD LYPT. ALTITUDE, DENSITY AND OVERAGE WAS NOT DETERMINED

WAS IV

ANNEX 2-V: CIBM MISSION ANALYSIS AND SELECTION

FRONT LIT 0-60	SIDE LIT 60-120	BACK LIT 120-180		
[26]	[30] 35 42 44 45 [49] 56		[46]	
	[60]	58	25	[51]
			28	
			31	[32] 33 39 40 47 51 55
				MORNING EVENING #18.
				DAY >18°

CLOUDY	43 50 <b>52</b> 54 59
OVERCAST	38 <b>48</b> 52
NIGHT	
CLEAR	DAY <b>34</b> 37

produce front-lit clouds. The designation of evening was chosen for Sun elevations between  $\pm 18$  deg. and the designation "night" was chosen for Sun elevations below -18 deg.

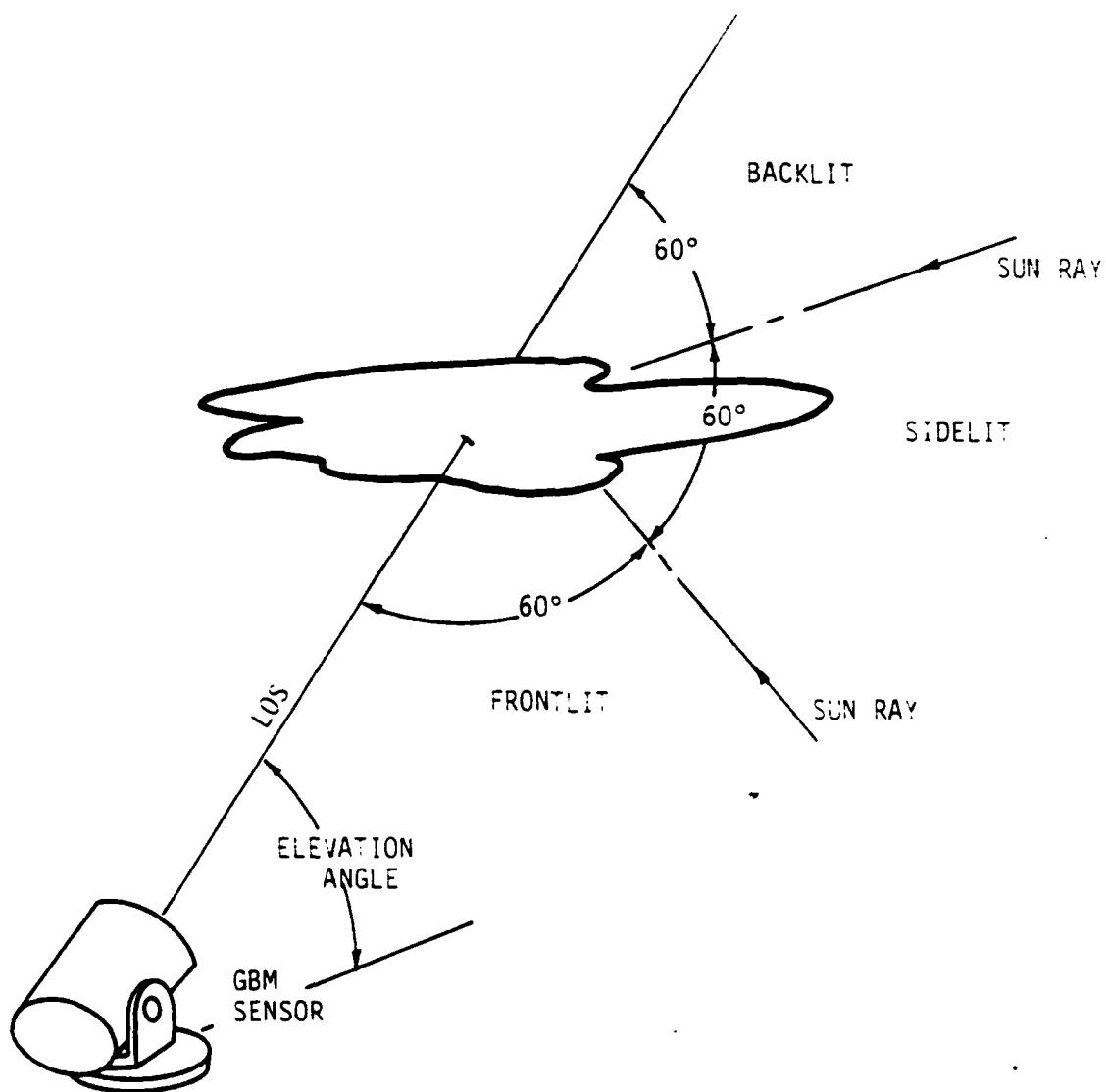


FIGURE 2-4. SUN POSITION AND SENSOR ELEVATION ANGLE

### 3. THEORY OF STATISTICAL ANALYSIS

The techniques and statistical methods used to perform the dual-band analysis in this report are defined below. Sections 3.1 through 3.4 describe standard statistical methods as found in many excellent references. Section 3.5 provides a rationale for the choice of the 30-point cosine roll-off apodization function, used on all data before Fourier analysis.

#### 3.1 MEANS AND VARIANCES

While not of primary interest in a comparative analysis, the determination of means and variances of the input data is required for other analysis functions such as cross-correlation. For a series of N observations (in this analysis N=256), the most probable estimate of the mean  $\mu$  is given by,

$$\mu = \frac{1}{N} \sum_{i=1}^N X_i$$

where  $X_i$  is the ith data element of the N sampled data points.

The best estimate of the variance  $s^2$  is given by,

$$s^2 = \frac{1}{N-1} \sum_{i=1}^N (X_i - \mu)^2$$

where N-1 is used since this represents the number of degrees of freedom left after determining  $\mu$  from N observations.

#### 3.2 CROSS-CORRELATIONS

Given two mutually stationary N-channel time series, the cross-correlation C as a function of phase lag is computed by the formula,

$$C(k, j, i+1) = \sum_{t=j+1}^N \left[ (x_t^{(k)} - \bar{x}^{(k)})(y_{t-i}^{(j)} - \bar{y}^{(j)}) \right] / N$$

where  $k, j = 1, 2, \dots, N; i = 0, 1, \dots, L$ ;  $L$  = the maximum number of lag points;  $x_t^{(k)}$  is channel  $k$  of the first time series;  $y_t^{(j)}$  is channel  $j$  of the second time series; and  $\bar{x}^{(k)}$  and  $\bar{y}^{(j)}$  are the corresponding means.

### 3.3 SPECTRAL DENSITIES AND CROSS-SPECTRA

The spectral densities  $S$  and cross-spectra  $C_s$  based on the corresponding cross-correlation function are calculated from the formulas

$$S(m\Delta\omega) = \frac{\Delta t}{2\pi} \left[ r_a(0) + 2 \sum_{q=1}^{m-1} r^*(q\Delta t) \cos mq\Delta t \Delta\omega + r^*(m\Delta t) \cos m\Delta t \Delta\omega \right]$$

where  $r_a(0)$  is the auto correlation function at zero phase lag,  $\Delta t$  is the interval between samples, and  $r^*$  is the correlation function filtered by the Bartlett Method,

$$r^*(k\Delta t) = (i - \frac{k}{m}) r(k\Delta t),$$

and

$$C_s(\omega) = \sum_{m=1}^{N-1} C(m) e^{-im\omega}$$

where  $C(m)$  represents the cross-correlation between data sets and  $\omega$  is the spatial or temporal frequency in samples per data interval.

### 3.4 LEVEL OF SIGNIFICANCE

In the interpretation of cross-correlation coefficients and subsequently cross-spectra, it is important to determine whether the coefficient values are likely to reflect a predictable relationship between data sets. A useful distribution for this determination is the probability  $P(r, N)$  that a random sample of  $N$  uncorrelated experimental data points would yield an experimental linear-correlation coefficient as large as or larger than the observed value of  $|r|$ . This probability function  $P(r, N)$  can be computed by

$$P(r, N) = 1 - \frac{2}{\sqrt{\pi}} \frac{[(V+1)/2]}{r(V/2)} \left\{ \sum_{i=0}^I (-1)^i \frac{i!}{(I-i)! i!} \frac{|r|^{2i+1}}{2i+1} \right\}$$

for even values of  $v$ , where  $v = N - 2$  and  $I = 0.5(v - 2)$ . This technique was used to determine the levels of significance discussed in Section 4.

### 3.5 APODIZATION

Because of the finite nature of data sets and the manner in which Fourier transform routines interpret the end points of these sets, it is necessary to smoothly bring the end points to zero amplitude if high-frequency aliased noise is to be avoided. The standard technique used to smoothly terminate data strings is to multiply them by an apodization window. The form of the window chosen for this study was the cosine roll-off in which the  $M$  samples at each end of the data set are multiplied by a factor from one to zero according to a cosine relationship. The following discussion gives the rationale for the choice of  $M = 30$ .

Figure 3-1 shows the Fourier transform of a 6-cycle-per-data interval sine wave having been filtered by a cosine roll-off apodization window of the indicated width. The first chart of this figure ( $M = 0$ ) corresponds to a boxcar window or no apodization beyond starting and stopping the data string to define the sampled data set. As the extent of the cosine roll-off increases, the high-frequency lobes or feet on the transform spike begin to reduce, but as this occurs the aliased dc noise level begins to increase in amplitude and spectral width. Figure 3-2 illustrates the increase in dc noise level with increasing  $M$ . Figure 3-3 shows the same relationship of the percent error in transform peak amplitude. Given these two contributions alone, the optimum condition occurs for no apodization or  $M = 0$ . However, the purpose of apodization is to remove the "feet" produced by the sudden termination of a data string. Therefore, it is necessary to look at the upper lobe peak amplitude as a function of apodization since these lobes will be added to any real transform data occurring at the same frequency. Figure 3-4 plots the relative upper lobe peak amplitude as a function of  $M$ . Taking all three factors into account, a bounded optimum value of  $M = 30$  is obtained, based on an upper limit of 2% peak error and 5% dc noise.

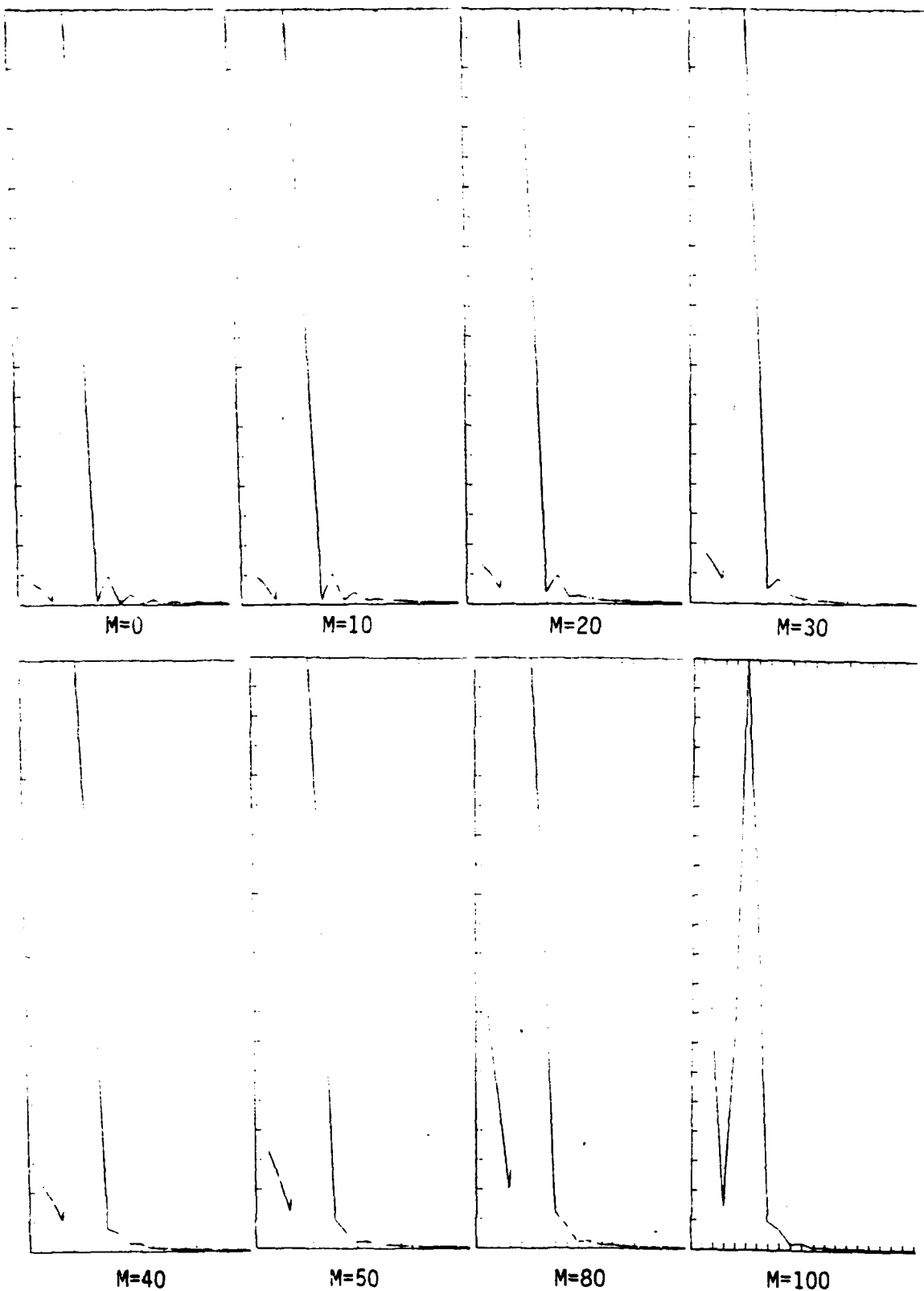


FIGURE 3-1. EFFECT OF APODIZATION ON 6 CYCLE PER INTERVAL SINE WAVE

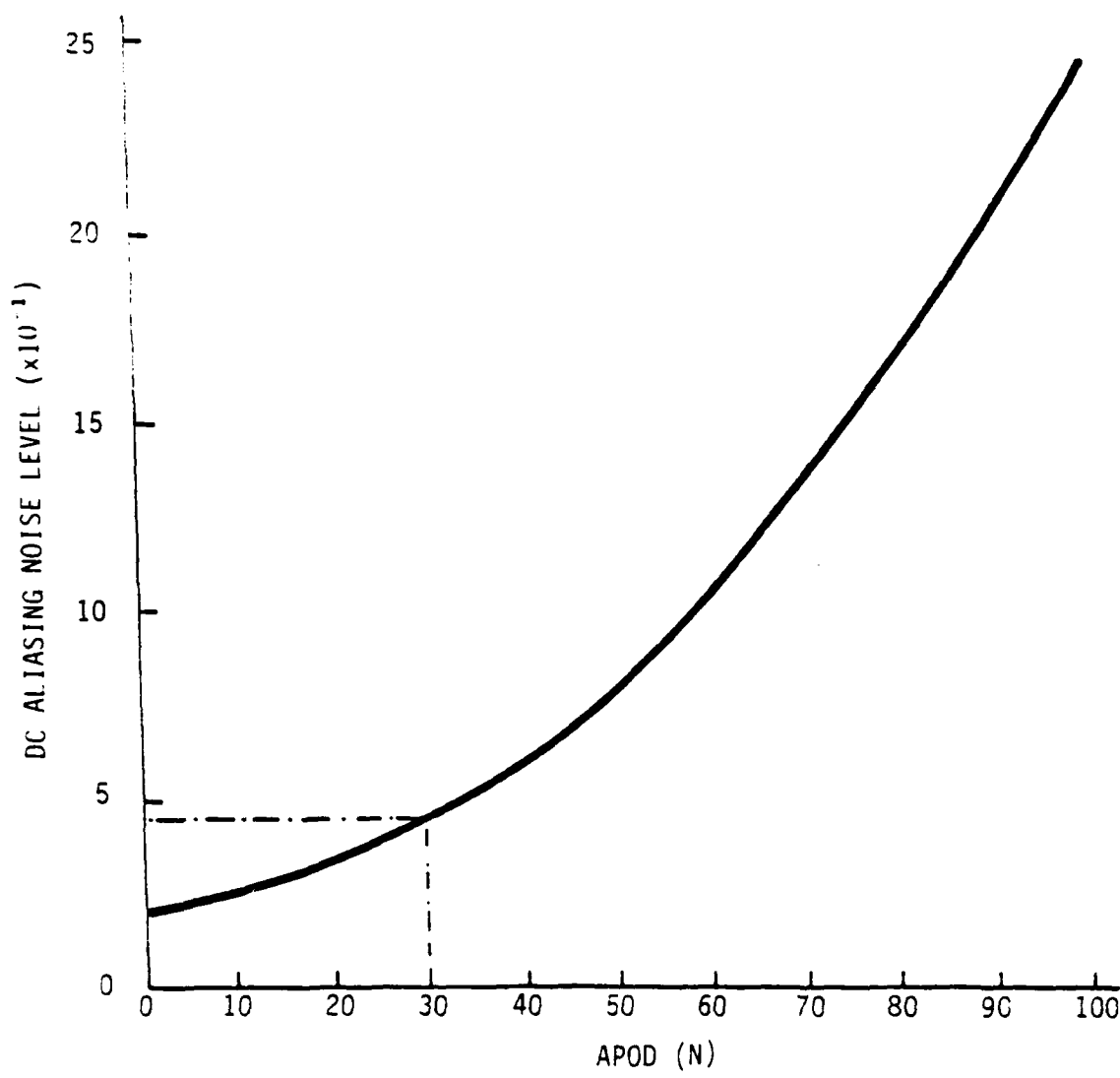


FIGURE 3-2. DC NOISE LEVEL VERSUS APODIZATION

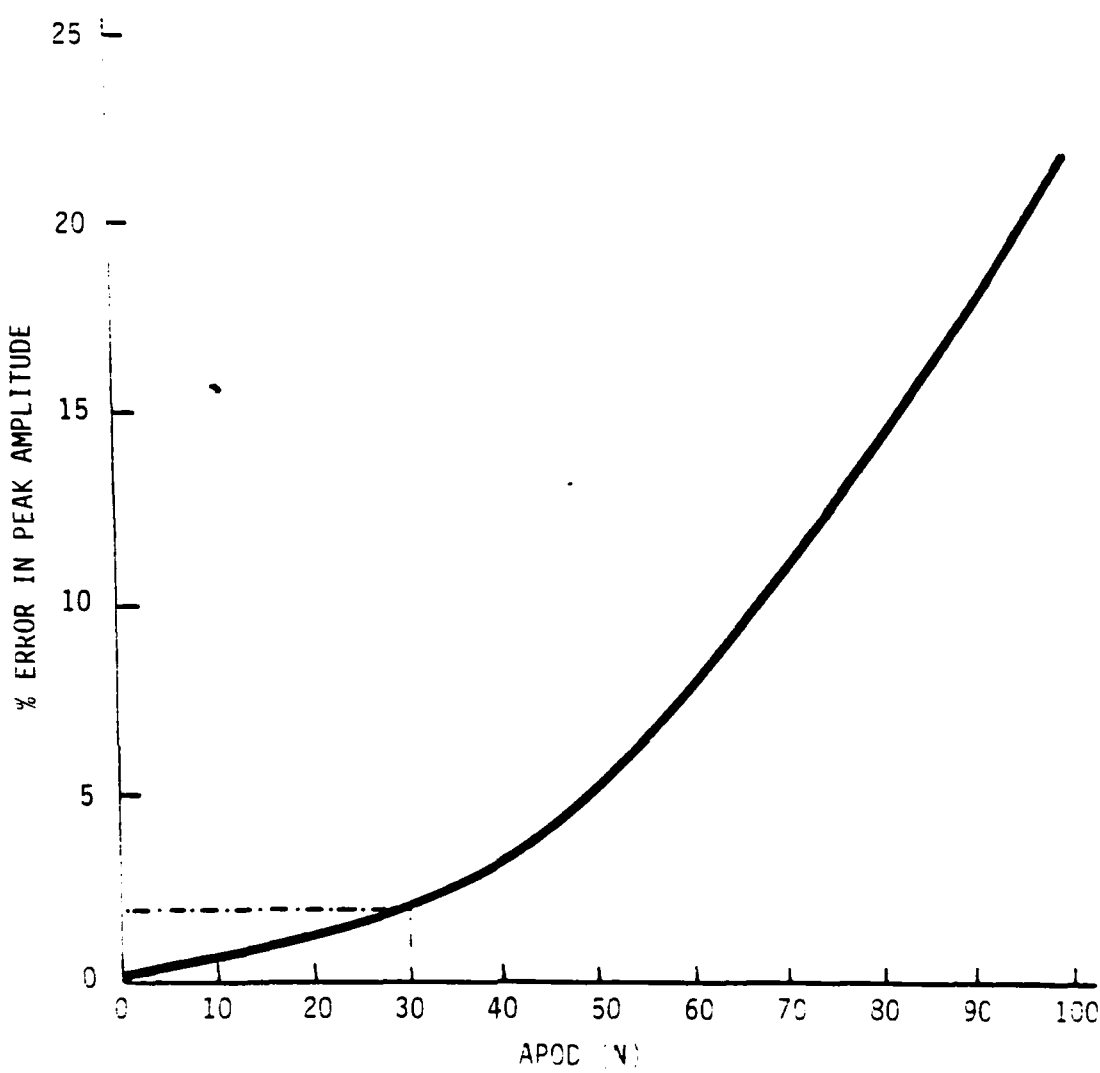


FIGURE 3-3. PERCENT ERROR IN AMPLITUDE VERSUS APODIZATION

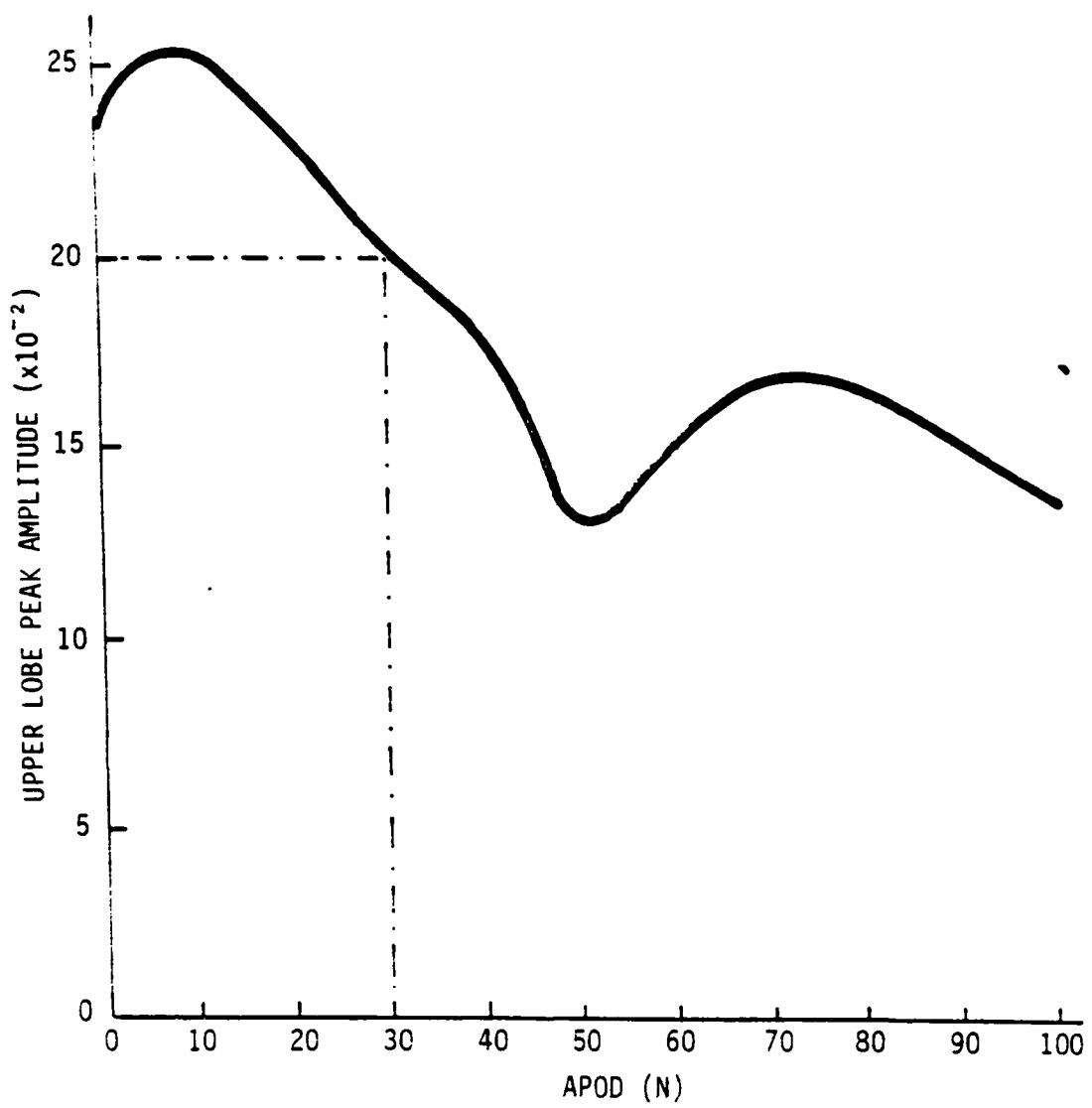


FIGURE 3-4. RELATIVE UPPER LOBE AMPLITUDE VERSUS APODIZATION

#### 4. RESULTS OF COMPARATIVE ANALYSIS

The cloud images of the cases chosen from the GBM data base were analyzed to determine the results given in this report. The example scanned fields-of-view shown in the illustrations and described below represent a set of the extremes observed in these analyses. These data were studied in the image plane using the cross-correlation function and in the Fourier plane using power spectral densities and cross-spectra functions.

##### 4.1 ORIGINAL CLOUD SCENE DATA

The original cloud data, once digitized, can be manipulated by the computer and displayed in many ways. Typically, the GBM mission data has been viewed in the form of a three-dimensional plot in which the voltage output from each detector is displayed as a section of a plane. These planes are then plotted and overlayed into a three-dimensional representation of the scanned field of view. Figures 4-1 and 4-2 are three-dimensional plots of the clouds scenes chosen as examples for this report. Another mode of display more nearly applicable for the purposes of illustrating clutter data is the contour plot. Figures 4-3 and 4-4 illustrate the same cloud data in a seven-level contour plot. Additionally, the computer allows the plotting of the detector output level along any line passing through the field of view. Figures 4-5 and 4-6 are such plots of longitudinal cuts through the contour plots, as indicated by the labeled lines. This technique greatly reduces the time and effort required to analyze these clutter scenes.

##### 4.2 CROSS-CORRELATIONS

The nine cases containing cloud scenes were compared between the LWIR and SWIR bands in the image plane through the cross-correlation functions, even though clouds were observed only in the LWIR passband in all but Case 60. The correlations were performed between zero lag and a positive lag of 50. This was done so that any misalignment between the two passbands could be detected by a shifted correlation peak. The solid line in Figures 4-7 through 4-10 represents the cross-correlation

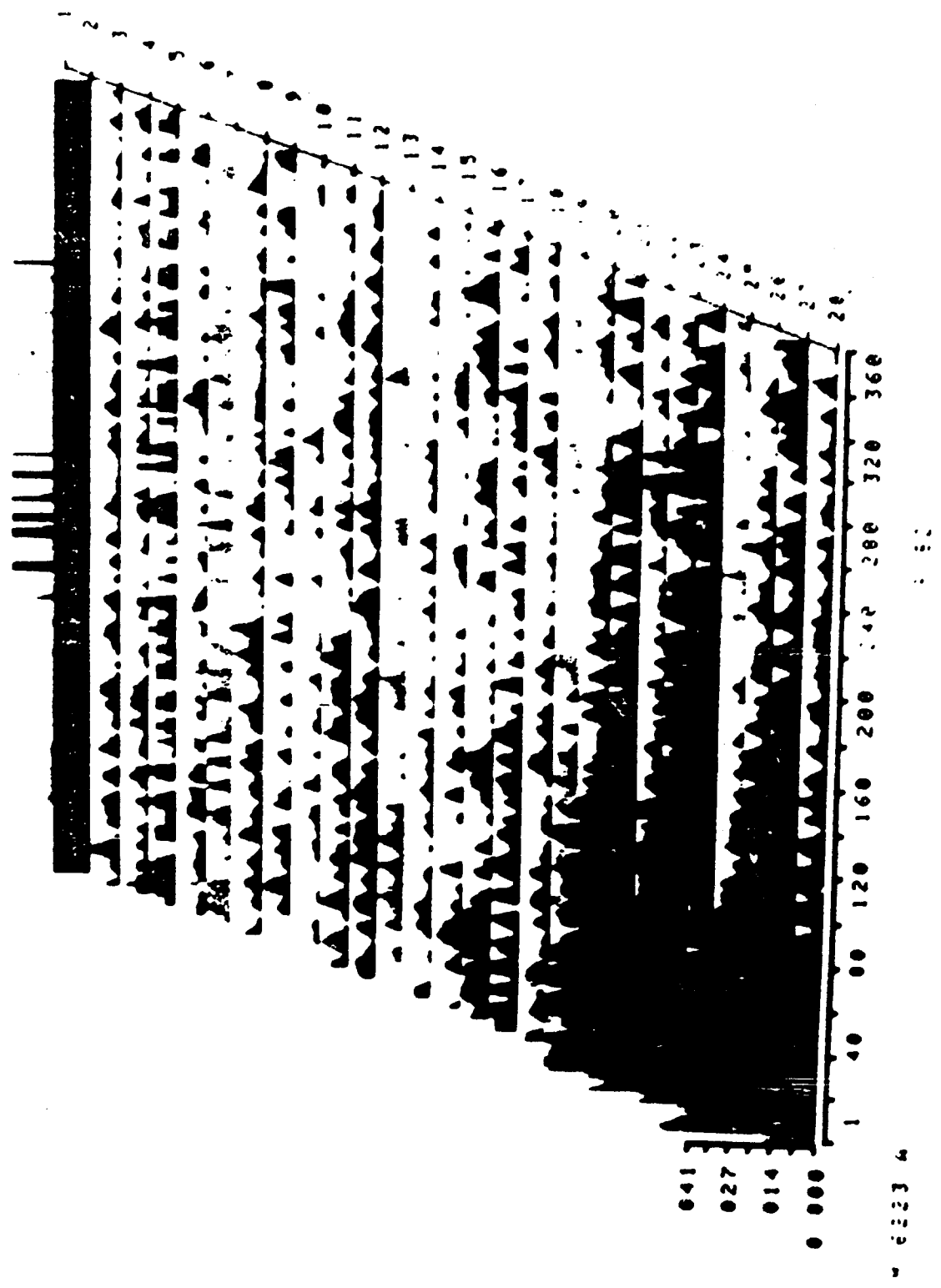


FIGURE 4-1. 3-D PLOT, CASE 49, LWIR, SF0V 603

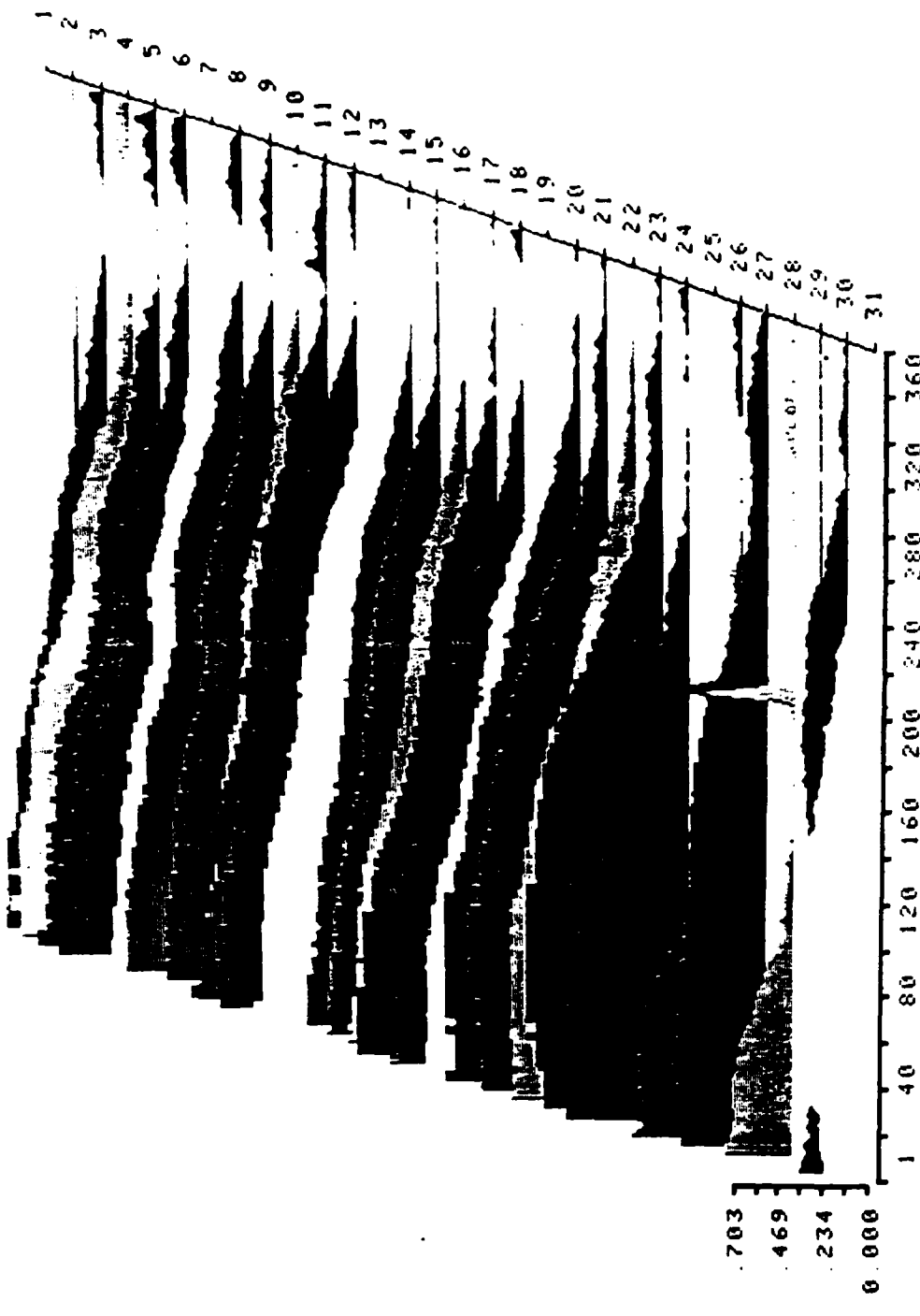
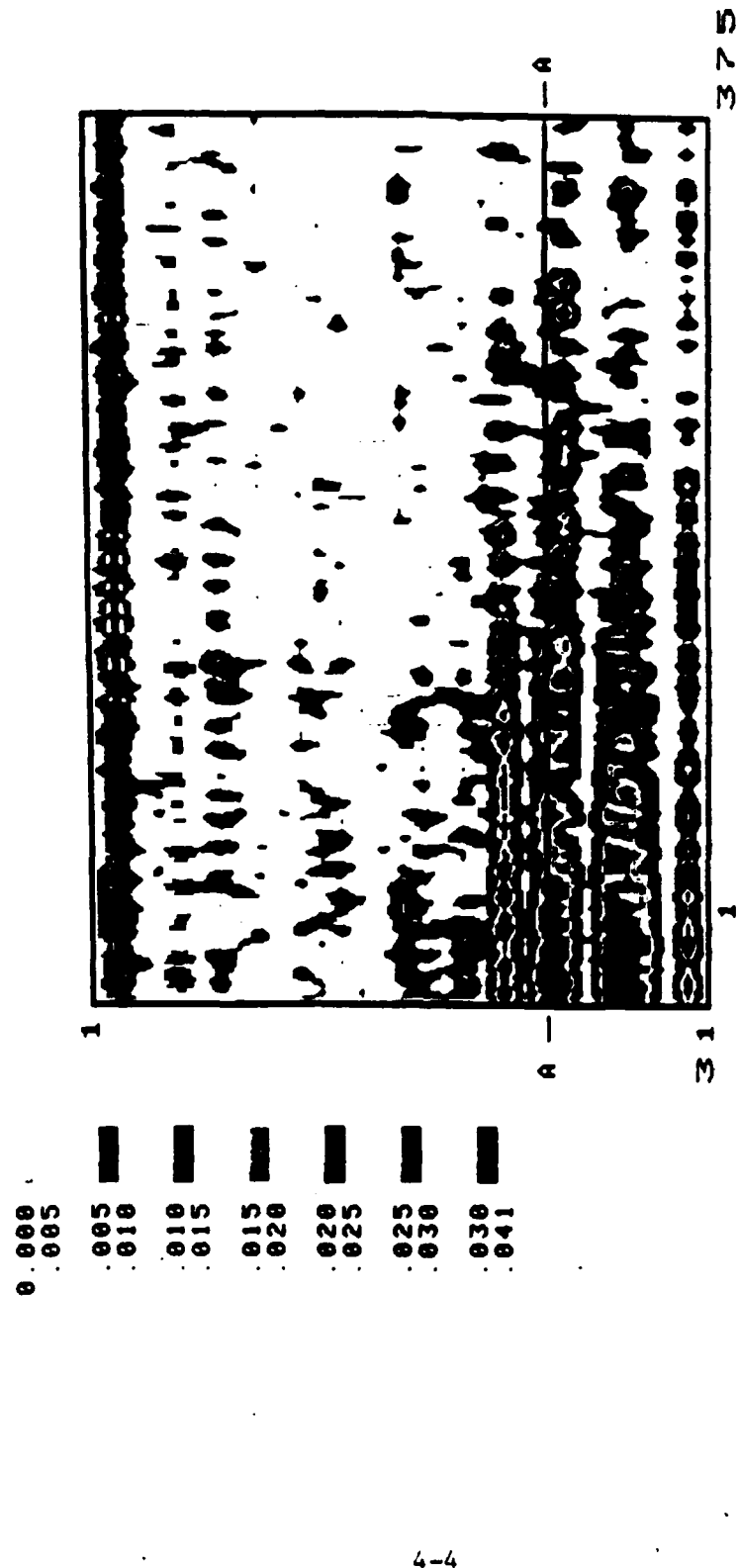


FIGURE 4-2. 3-D PLOT, CASE 60, LWIR, SF0V 131

FIGURE 4-3. EONTOUR PLOT, CASE 49, LWIR, SFOV 603



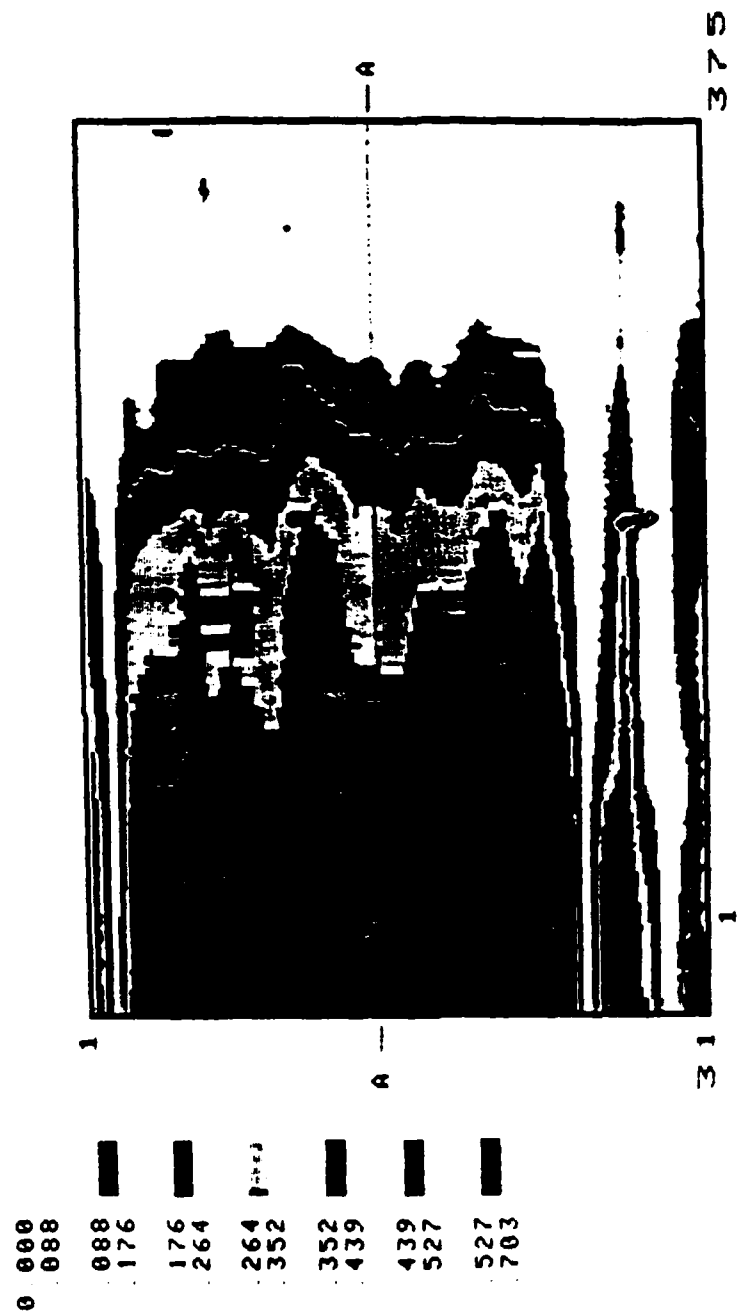


FIGURE 4-4. CONTOUR PLOT, CASE 60, LWIR, SFOV 131

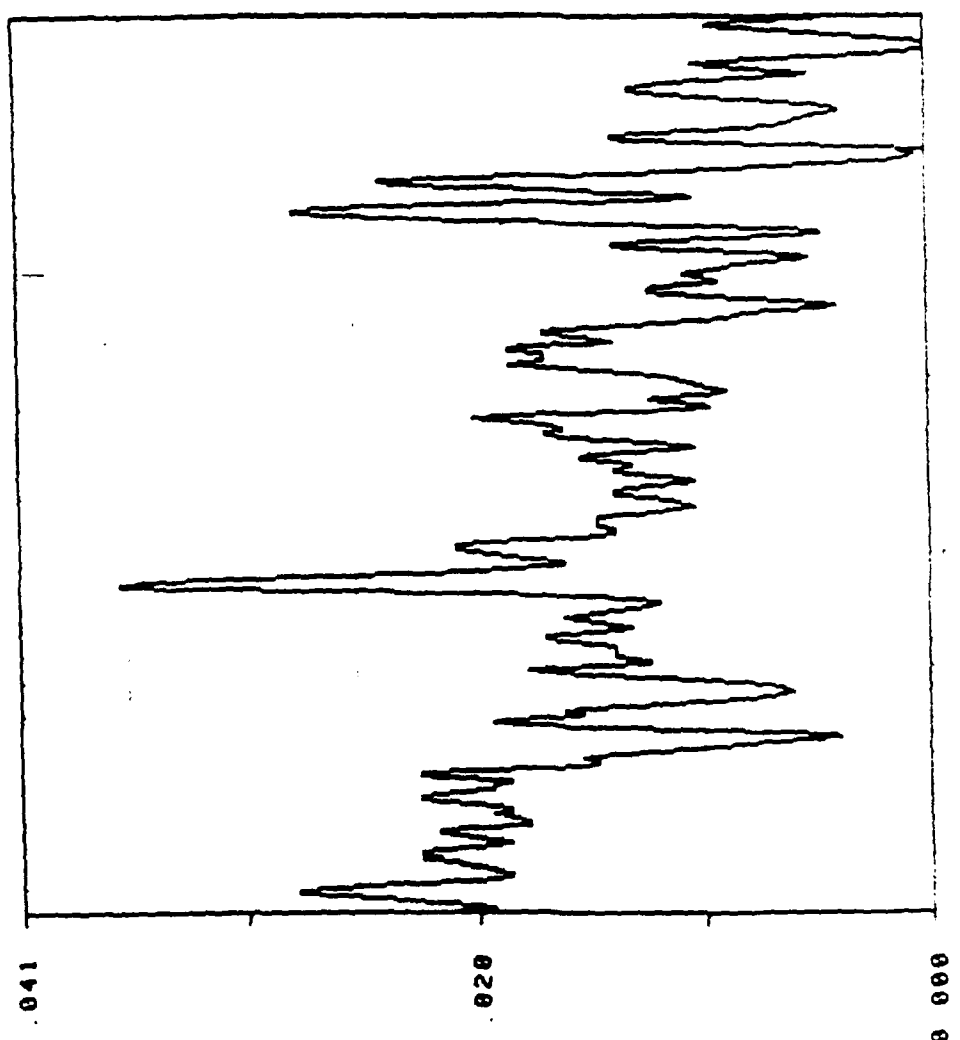
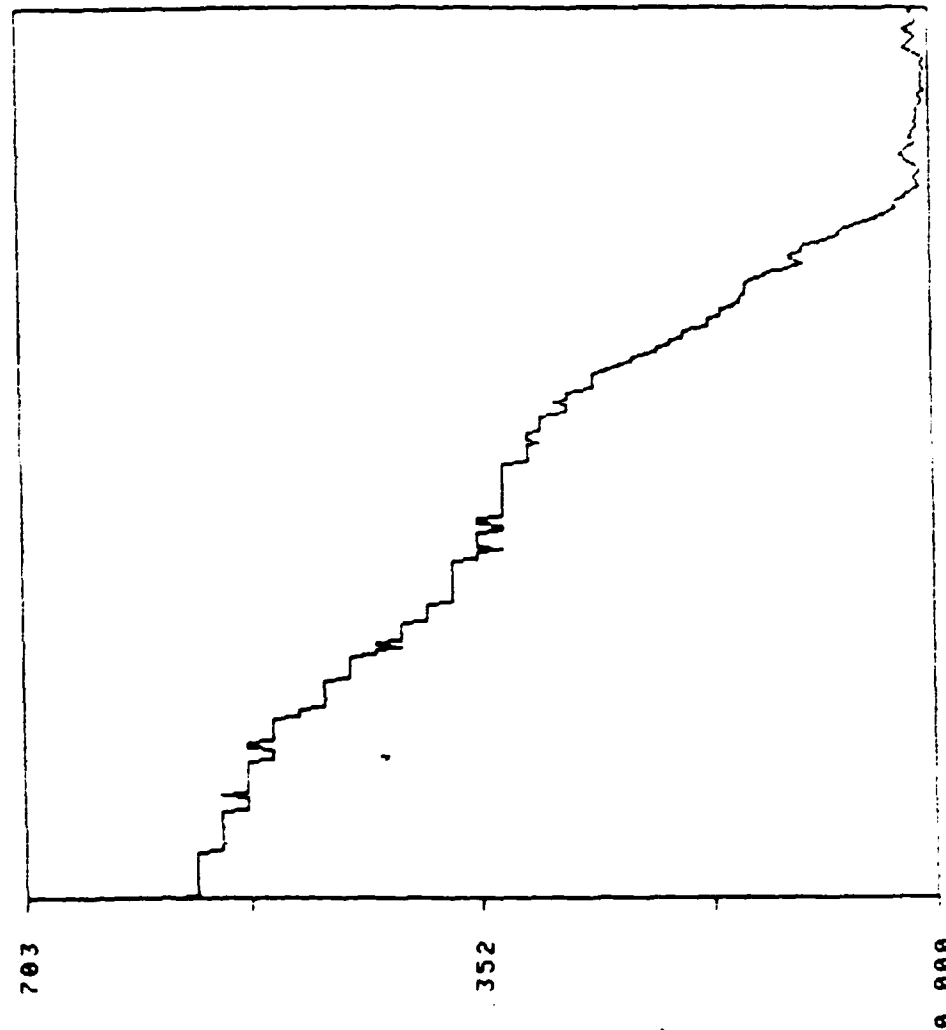


FIGURE 4-5. LONGITUDINAL CUT A-A, CASE 49, LWIR, SFOV 603

FIGURE 4-6. (U) LONGITUDINAL CII A-A, CAST 60, IWIR, SHOV 131



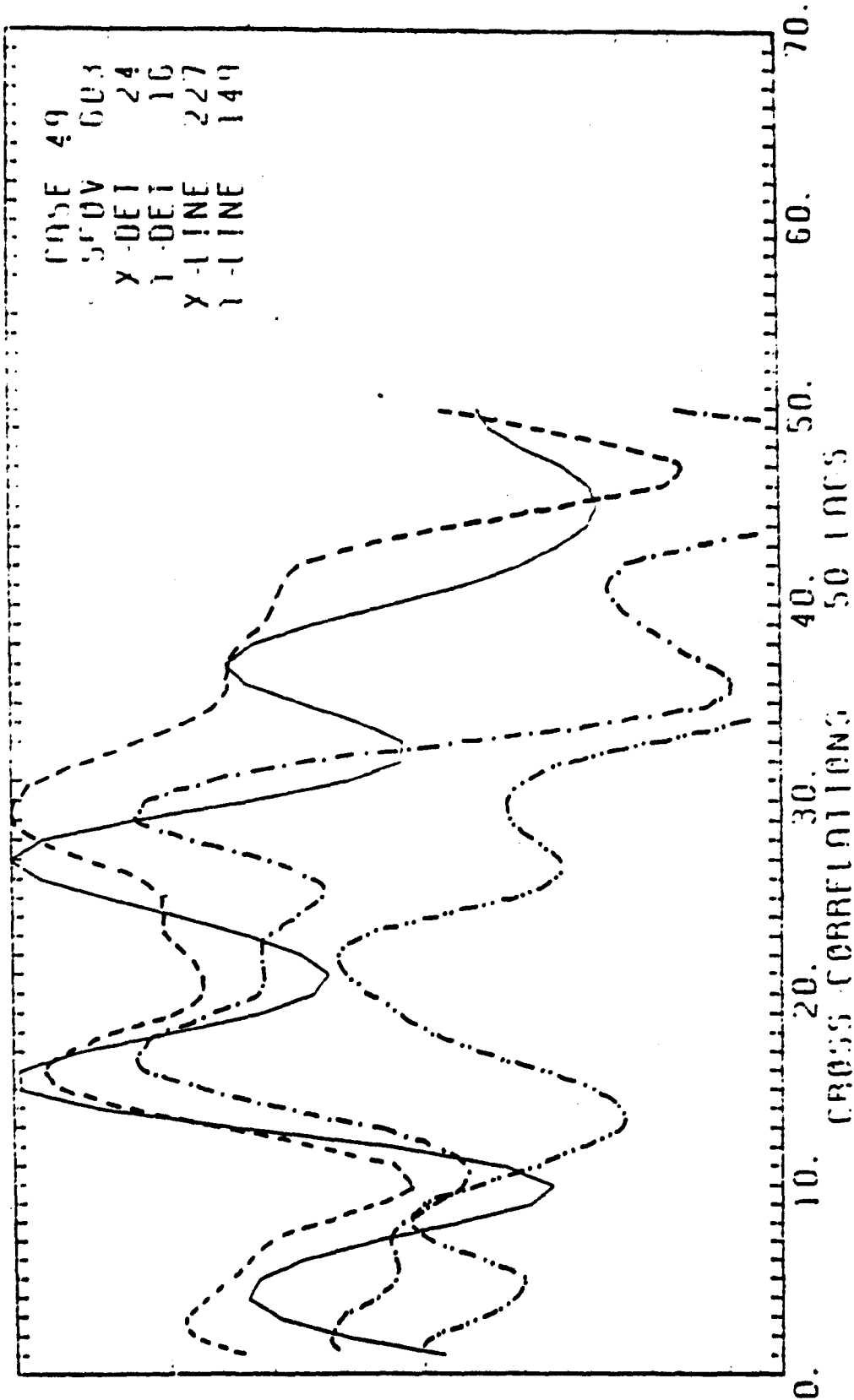


FIGURE 4-7. (U) CROSS-CORRELATION, CASE 49, SF0V 603

00-36007 \* 3165

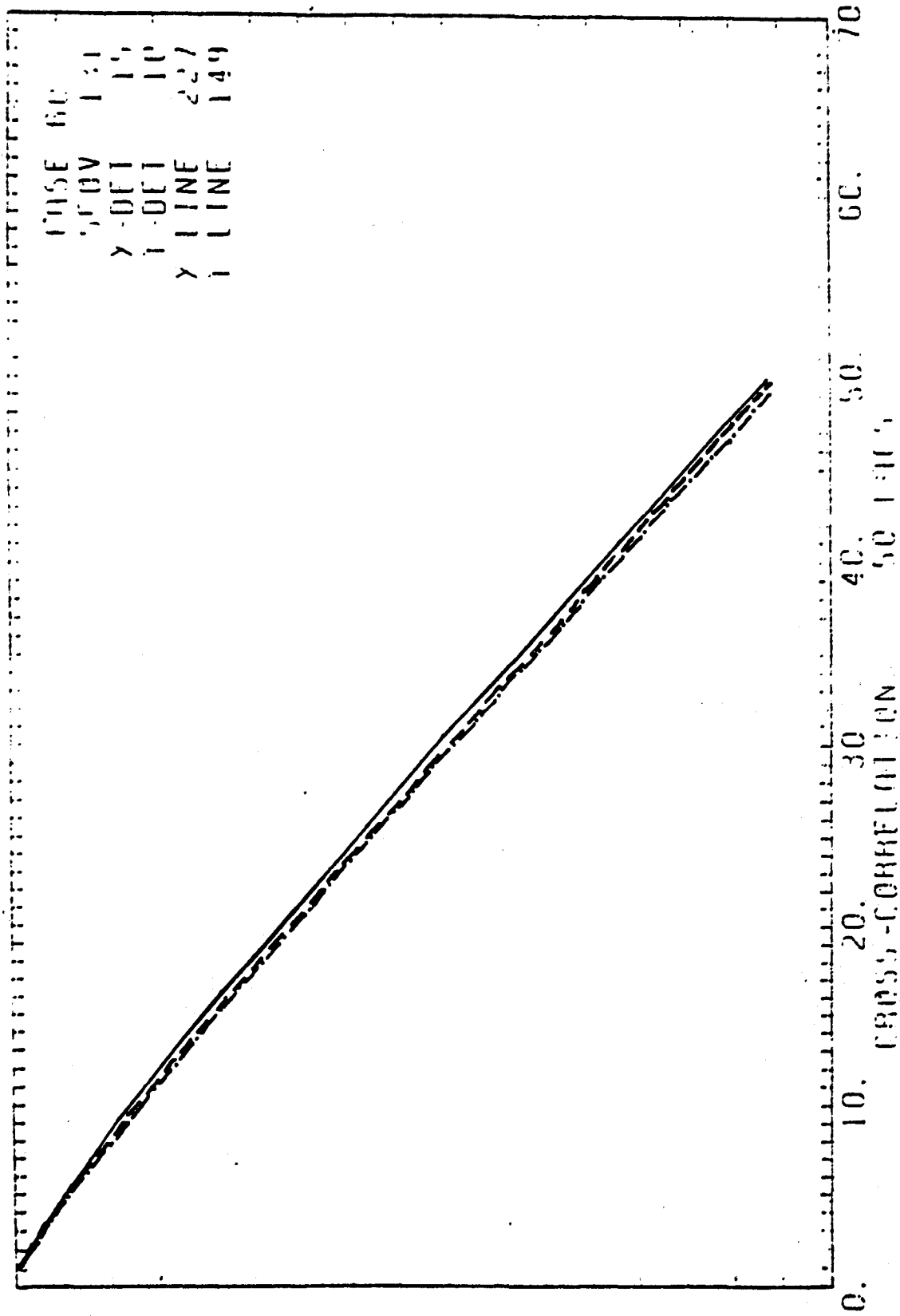


FIGURE 4-8. CROSS-CORRELATION, CASE 60, SFOV 131

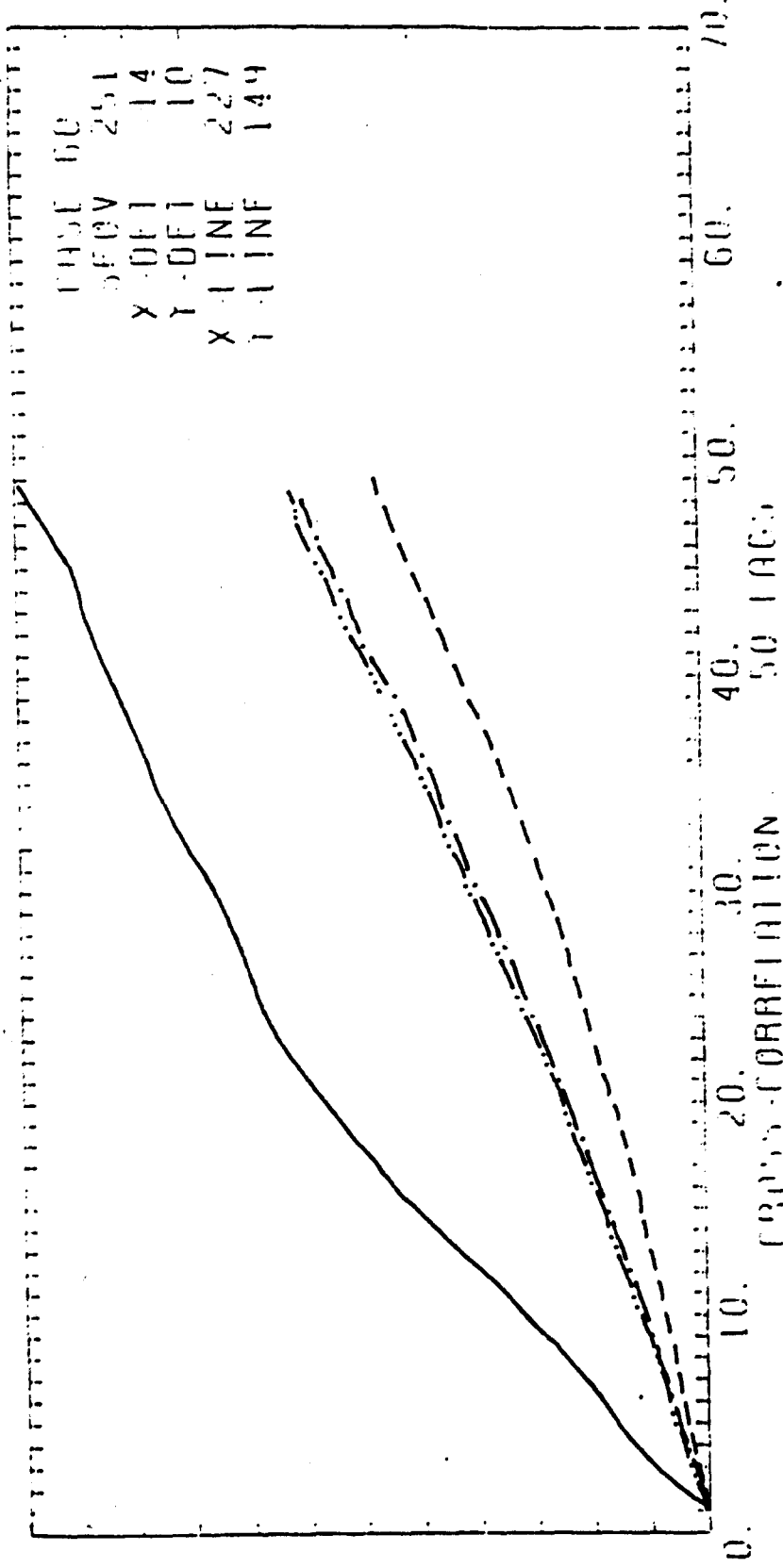


FIGURE 4-9. CROSS-CORRELATION, CASE 60, SFOV 251

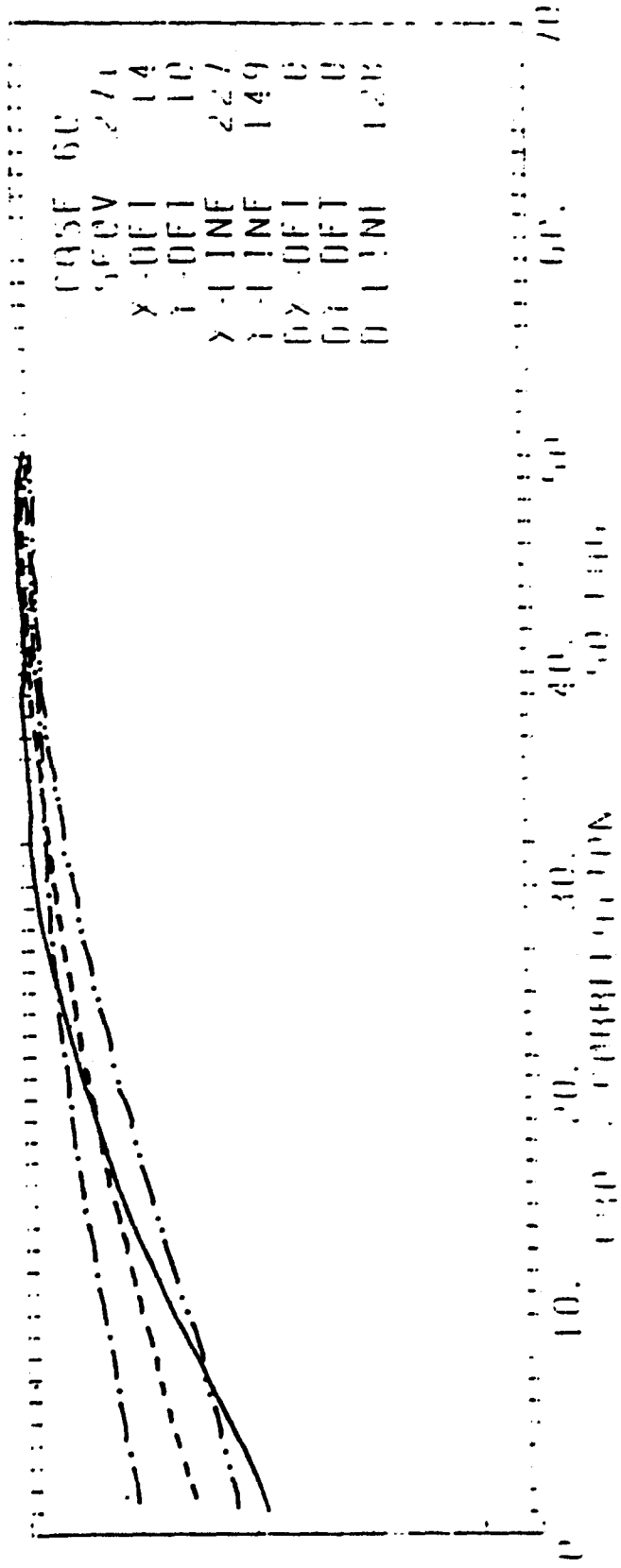


FIGURE 4-10. CROSS-CORRELATION, CASE 60, SFOV 271

between the two passbands for a single detector output. The dashed line illustrates the same cross-correlation except that the output of three adjacent detectors in the SFOV have been averaged. The dash/dot line and the dash/double-dot line represent cross-correlations for five and seven detectors, respectively. The purpose of this averaging is to determine the effect on the correlation level of a varying detector size, or a reduced optical resolution. It is noted that for the uncorrelated cases, the combination of additional detectors produced significant variations in the cross-correlation function, while for Case 60 little change was seen. This is accounted for by the fact that the low spatial frequencies of the cloud scenes are the major contributors to the correlation level in the majority of cases. This effect will be discussed in more detail in Section 4.3.

Case 60 produced significant levels of correlation between bands similar to the example given in Figure 4-8 in approximately 87% of the frames. Figure 4-9 illustrates an interesting negative correlation which was observed in one portion of the sky of Case 60. Figure 4-10 illustrates a phase lag of approximately 40 sampled units exists between the LWIR and SWIR radiometric profiles. It has been determined that this is not due to a misalignment of the two SFOVs as was first suspected, but rather is a phenomenon of the cloud itself. These scenes and possible scenes showing negative correlation are indicative of a shift in radiometric profile in clouds between the LWIR and SWIR passbands.

#### 4.3 POWER SPECTRAL DENSITIES AND CROSS-SPECTRA

The power spectral densities of single- and multiple-detector combinations, as shown in the example of Figure 4-11, were calculated for each of the chosen cases; in general, the frames in which clouds are present exhibit 1/f type spectral densities in agreement with previous investigations. That is, the relative amplitude of the power spectral density curve is inversely proportional to the spatial (or temporal) frequency.

This spectral analysis has shown that in those cases for which clouds appear in both passbands, the LWIR is of a higher overall

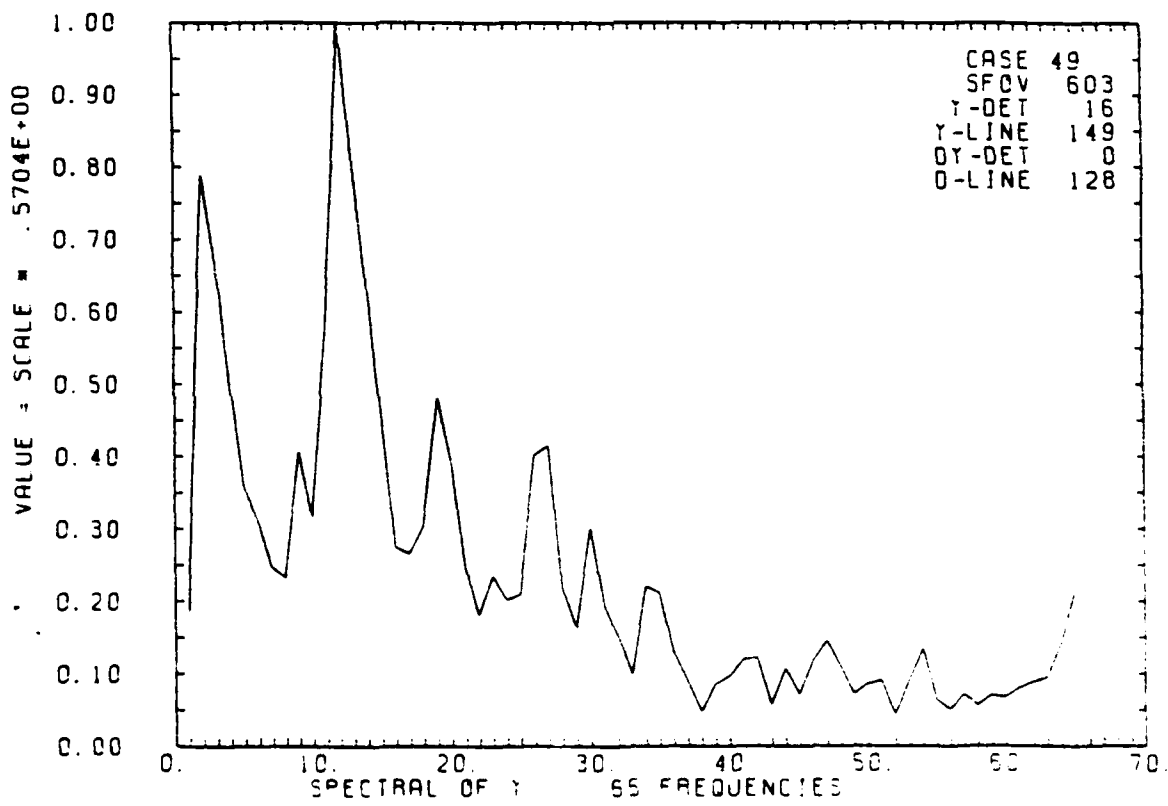
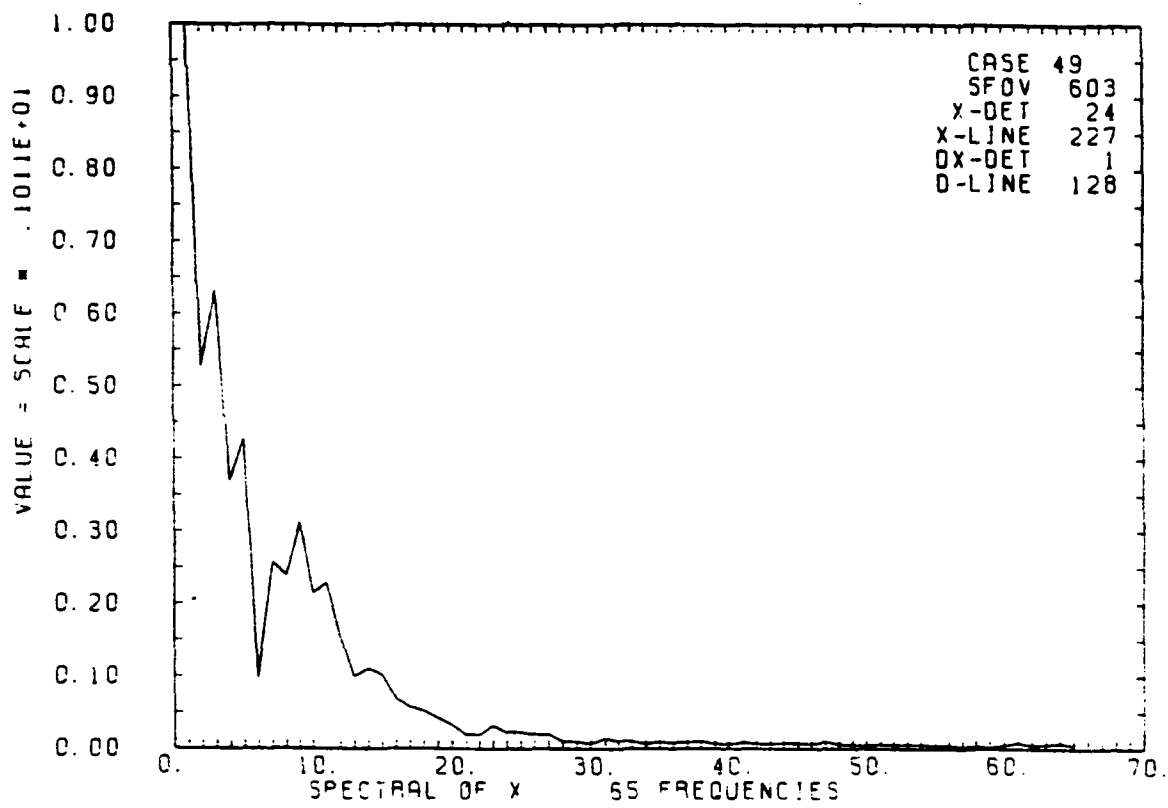


FIGURE 4-11. SPECTRAL DENSITY, CASE 49, SFOV 603, NDET=3, LWIR/SWIR

amplitude while the SWIR exhibits a greater high-spatial-frequency content. In those cases for which distinct clouds are visible only in the LWIR, the noise level in the SWIR band in the region on the cloud did increase about a factor of 3 above the clear ambient. As the density of the cloud increases, the SWIR begins to perceive many point-source spikes that are essentially uncorrelated in time to the observable limit for the GBM data (i.e., 15 Hz). At still greater cloud densities, isolated spots of the cloud formation begin to grow in the SWIR band until a total cloud is detectable. Unfortunately, this phenomenon is reduced in most of the GBM mission due to severe attenuation in the SWIR passband.

The cross-spectra analyses have indicated that the major portion of the correlation occurs at the lower spatial frequencies. As expected, the overall shape of the cloud, when observed in both bands, is similar, but fine structure of the clouds is totally independent between bands. This is a most important result since it suggests that only empirical models of atmospheric clutter can be made to adequately represent the same cloud in both the SWIR and the LWIR passbands, and that no deterministic models can be developed which will predict the radiometric profile of a cloud in one passband when given the radiometric profile of the cloud in the other.

#### 4.4 ESTIMATION OF CLOUD TRANSMISSION PROFILES

The GBM mission was to record the radiometric signatures of reentry vehicles as they passed through the atmosphere. A detailed model exists which was used to determine the expected radiometric signature of a heated RV. In addition, actual measurements of identical RV signatures from clear-sky missions can be accessed. All this leads to the use potential of the reentry vehicle as a calibrated IR source. The missions for which the RV passes behind clouds (there are many) provide a unique opportunity to measure the transmission profiles of example clouds. Figures 4-12 and 4-13 illustrate this capability. The solid lines represent the RV irradiance in each band as measured by the GBM sensor, while the open boxes trace the measured RV signature in clear-sky conditions. As in the cross-spectra, the SWIR shows a reduced overall degradation but a higher spatial frequency variation in signal.

## IRRADIANCE - COLOR A

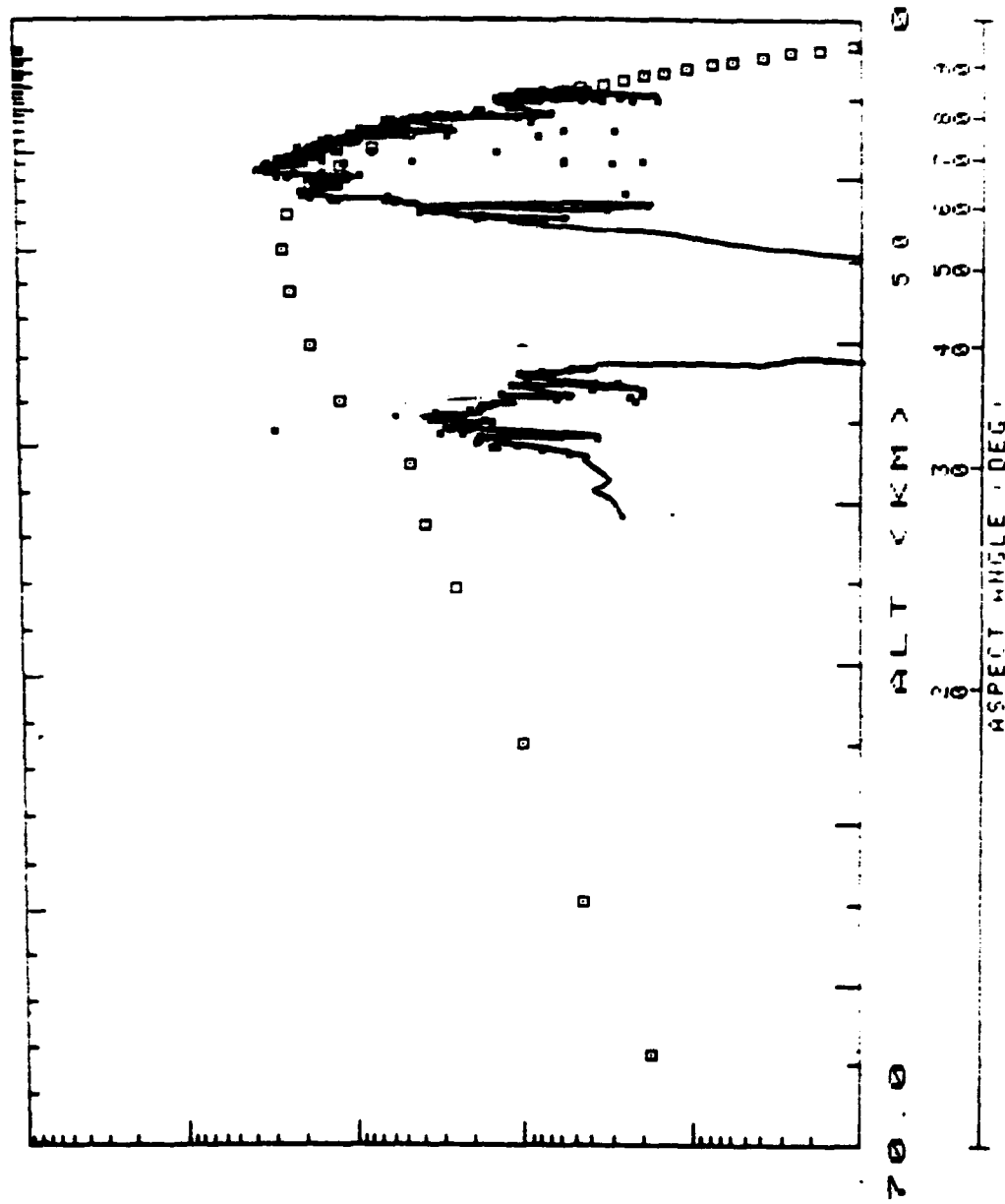


FIGURE 4-12. TRANSMISSION PROFILE, LWIR, RV REENTRY

IRRADIANCE - COLOR

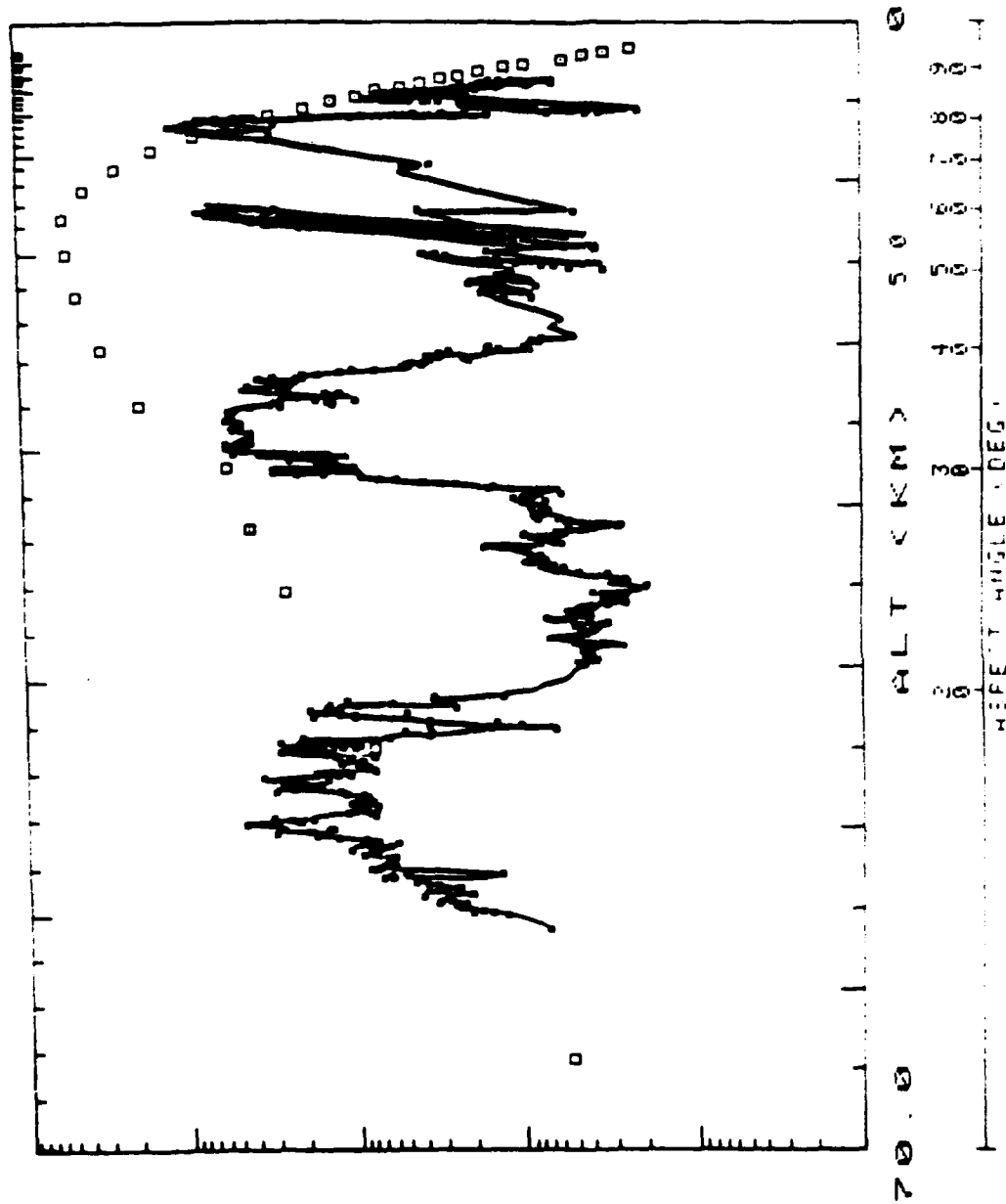


FIGURE 4-13. TRANSMISSION PROFILE, SWIR, RV REENTRY

Similar measurements could be used to develop a cloud attenuation data-base from the GBM mission archives.

## 5. CLOUD SCENE SYNTHESIS

### 5.1 IMAGE MODEL

The generation of synthetic imagery to simulate measured infrared cloud imagery requires the use of a suitable mathematical model. Since cloud structure is highly variable and unpredictable, it is natural to choose for this purpose some type of stochastic model. Although clouds are inherently three-dimensional objects and three-dimensional stochastic models might be considered for their representation, it seems more efficient to attempt to represent the two-dimensional cloud images directly rather than to obtain them by projection of three-dimensional cloud structure onto a plane. This approach affords a choice from among a large number of two-dimensional stochastic models which have been developed for purposes of texture analysis and texture synthesis in the fields of digital image processing and computer image generation.

The literature of texture analysis and texture synthesis was surveyed at some length in an effort to identify a stochastic model which combines the attributes of simplicity of implementation and adequate fidelity of modeling. Since these requirements are obviously mutually antagonistic, a compromise is to be expected in selection of the model.

Study of the literature suggested that a simple two-dimensional autoregressive model should satisfy the requirements, particularly since it has been used with success by others to model cloud imagery (Ref. 1). For this model (as for most others), the image is regarded as a two-dimensional rectangular array of discrete elements (pixels), each of which is described by a pair of indices specifying its location within the array and a value corresponding to the image "brightness" or "gray level" at the point represented. Using the notation  $u_{i,j}$  to represent the gray level of the pixel in the  $i$ th row and  $j$ th column of the array, the general first-order autoregressive model may be written as

$$u_{i,j} = a_1 u_{i-1,j} + a_2 u_{i,j-1} + a_3 u_{i-1,j-1} + \epsilon_{i,j} \quad (5-1)$$

where  $a_1, a_2$  and  $a_3$  are constants, and  $\epsilon_{i,j}$  is a white noise process such that  $E[\epsilon_{i,j}\epsilon_{i+k,j+l}] = \beta^{|k|}\delta_{k,l}$ . Here  $\beta$  is a constant, and  $\delta_{m,n}$  represents the Kronecker delta function.

The constants  $a_1, a_2$  and  $a_3$  determine the autocorrelation characteristics of the process defined by  $u_{i,j}$ . In this study, it is assumed that the structure of cloud imagery is approximately isotropic. Although the simple autoregressive model of Equation 1 is inherently anisotropic, it can be made to approximate the isotropic ideal by choosing  $a_1 = a_2 = \rho$  with  $a_3 = -\rho^2$ . In this case,  $\beta = 1 - \rho^2$ . Thus, a quasi-isotropic form of the model of Equation 5-1 is

$$u_{i,j} = \rho u_{i-1,j} + \rho u_{i,j-1} - \rho^2 u_{i-1,j-1} + (1 - \rho^2) \epsilon_{i,j} \quad (5-2)$$

In this model,  $u_{i,j}$  and  $\epsilon_{i,j}$  exhibit the same variance.

It can be shown that the process  $u_{i,j}$  generated by the model of Equation 5-2 has an autocovariance function of the form

$$R(k, l) = E[u_{i,j}u_{i-k,j+l}] = \sigma^2 \rho^{|k| + |l|} \quad (5-3)$$

where  $E[\cdot]$  denotes the expected value of the enclosed random variable, and  $\mu = E[u_{i,j}]$ , independent of  $i$  and  $j$ . The corresponding spectral density function is

$$S(\xi, \eta) = \frac{(1 - \xi^2)^2}{[1 - \rho\xi - \rho\eta + \rho^2\xi\eta][1 - \frac{\xi}{\eta} - \frac{\rho}{\eta} + \frac{\rho^2}{\xi\eta}]} \quad (5-4)$$

## 5.2 IMAGE ANALYSIS

To employ the model of Equation 2 to synthesize imagery representative of a given cloud type, it is necessary to supply numerical values for the model parameters  $\rho$  and  $\sigma$  defined in the previous section. These values are most easily determined in the present instance by empirical means using the available measured data. It is necessary only to compute values of the autocovariance function  $R(k,0)$  as defined in Equation 3 for a range of values of the lag parameter  $k$  and then to select values for  $\rho$  and  $\sigma$  which give the best fit of Equation 3 to the

computed autocovariance function. The value of  $\sigma^2$  may be read off directly as  $r(0,0)$ , and  $\rho$  may then be identified with  $R(1,0)/\sigma^2$ . Alternatively, the value of  $\rho$  may be taken to be  $\exp(-1/k')$ , where  $k'$  is the value of the lag such that  $R(k',0)/\sigma^2 = \exp(-1)$ .

The autocovariance function  $R(k,0)$  was computed on selected GBM images, suitably filtered to resemble data as it would appear if recorded by the IRST sensor. (See Section \_\_\_\_). For this purpose a standard statistical subroutine (FTAUTO) from the IMSL Library of mathematical applications routines was employed. The autocovariance of the signal from each of several selected detectors was computed for each detector separately, and then an average over detectors was performed to yield a composite value for  $R(k,0)$ ,  $k = 1,2,\dots,80$ . The resulting composite values were plotted against the lag,  $k$ . The plot was then used to read off values of  $\rho$  and  $\sigma$  as outlined above.

### 5.3 IMAGE SYNTHESIS

Inspection of the autoregressive model of Equation 5-2 reveals that samples of the process  $u_{i,j}$  may be generated recursively provided that values of  $u_{1,j}$ ,  $j = 1,2,\dots,J$  and  $u_{i,1}$ ,  $i = 1,2,\dots,I$  are available. That is, given values of  $u_{i,j}$  for all pixels in the first row and the first column of the image array, the values of all remaining pixels may be directly determined by successive application of Equation 5-2. The remaining problem is then to provide values for pixels in the first row and first column of the array.

The approach taken in this study is to supply the required pixel values from a combination of measured data and synthesized values as follows. A typical sample of data from a single GBM detector (suitably filtered to simulate IRST data) consisting of a sequence of 93 successive pixels is used as the input "time series" to SUBROUTINE FTCMP of the IMSL Library. This routine performs an analysis of a time series based on a stochastic autoregressive integrated moving average (ARIMA) model. It develops values of required model parameters from the given time series and then uses these values to synthesize a continuation of the stochastic process for future time. With the 93-pixel sample as input, FTCMP was used to extrapolate the sequence to give a total of 512

samples. These 512 samples were then used as the values of  $u_{1,j}, j = 1, 2, \dots, 512$  and again as values of  $u_{i,1}, i = 1, 2, \dots, 512$ . A straightforward application of Equation 2 using values of  $\rho$  and  $\sigma$  obtained as described in the preceding section then permitted filling of the remainder of the array.

The procedure described above may be used to synthesize homogeneous cloud images, but of greater interest in the present application are celestial scenes containing a mixture of cloud and clear sky. The approach used in this study to generate such images is sometimes referred to as the Background-Foreground model. In this model, the image array is suitably partitioned into regions of two types. Although the terms "background" and "foreground" are conventionally used to label these regions, "sky" and "cloud" will serve better here. Homogeneous images of sky and cloud are generated as described above, and the partitioned array is used as a guide in constructing a composite image using the following simple algorithm. Pixels in the partitioned image are examined sequentially, and their type ("sky" or "cloud") is noted. If the pixel type is "sky," the value of the pixel at the corresponding location in the homogeneous sky image is inserted into the composite image at the corresponding location. Similarly, if the type "cloud" is noted, the pixel at the corresponding location in the composite image is assigned the value of the pixel at the corresponding position in the homogeneous cloud image.

Use of the Background Foreground approach introduces two new problems: How is the partitioning to be accomplished to give a realistic (irregular) boundary line separating "cloud" and "sky" regions? How can the abrupt transition which will occur at the boundary be made more realistic without additional processing?

The partitioning problem is solved by employing stochastic interpolation schemes proposed by Fournier, Fussell, and Carpenter (Ref. 2) to approximate fractal curves. It has been shown (Ref. 3) that cloud perimeters are fractal curves of fractal dimension  $D = 1.35$ . The method of Reference 2 permits the generation of a fractal curve of the appropriate fractal dimension between any pair of points in a plane. In the present application, one of these points is chosen to lie on the

upper boundary of the image plane, while the second point is chosen to lie on the lower boundary. The fractal curve connecting these two points thus divides the image roughly into left and right regions which may be identified with "sky" and "cloud", respectively. A slight modification of the method of Reference 2 permits the introduction of a controlled degree of convexity into the generated curve to simulate the "fluffy" appearance of clouds. Without this feature, any curves generated would be statistically symmetrical, and the assignment of "sky" and "cloud" values to left and right regions would be completely arbitrary. The convexity parameter introduced is simply a constant bias value added to the random variable used in the stochastic interpolation algorithm of Reference 2. Since no empirical value for this bias has been reported, a value (0.02) was selected which appears visually to yield credible cloud contours.

Plots of infrared cloud data for scans which intersect cloud boundaries typically exhibit a gradual decrease in cloud radiance as the cloud-sky boundary is approached from the "cloud" side. In addition, as the cloud becomes more tenuous near the boundary, there may be "holes" in the cloud through which the sky may be seen. To represent these effects, the "cloud" portion of the image is modified as follows.

Let  $C(x,y)$  and  $S(x,y)$  represent the cloud and sky radiances at point  $(x,y)$  in the two homogeneous regions, respectively. Consider a single horizontal scan line (row of pixels) from the image corresponding to a constant value of  $y$ , and suppose that the cloud boundary intersects this scan line at the point  $(x_1, y)$  with "cloud" corresponding to  $x > x_1$ , "sky" to  $x < x_1$ . We define a modified cloud radiance  $C'(x,y)$  for  $x > x_1$  by  $C'(x,y) = \text{greater of } (S(x,y) \text{ and } C(x,y) - C(x_1,y) \exp(-(x-x_1)/d))$ . Here,  $d$  is a characteristic length, determined empirically, which provides a measure of the rate of decrease of cloud radiance as the cloud-sky boundary is approached. In the case where the horizontal scan line,  $y$ , intersects the boundary at two points,  $x_1$  and  $x_2$ , with the interval  $(x_1, x_2)$  corresponding to "cloud", the expression for  $C'(x,y)$  with  $x_1 < x < x_2$  is  
$$C'(x,y) = \text{greater of } (S(x,y) \text{ and } C(x,y) - C(x_1,y) \exp(-(x-x_1)/d) - C(x_2,y) \exp(-(x_2-x)/d)).$$

Figures 5-1 through 5-7 are graphic representations of cloud scenes generated using the above method. Figures 5-1 and 5-2 represent clouds generated based on the data for Case 60 for the LWIR and SWIR passbands, respectively. Figure 5-3 is also based on Case 60 SWIR data but for a reduced sensor sensitivity and resolution.

#### 5.4 TEMPORAL PROPAGATION

In addition to the ability to synthesize textures resembling the spatial distribution of infrared radiation observed in clouds, it is also desirable to be able to simulate the evolution of these distributions in time. Given a synthetic radiance distribution at time  $t = t_a$  represented by an array of pixels  $a_{i,j}$ , such a model would be capable of providing a credible distribution  $b_{i,j}$  over the same set of pixels at a later time  $t = t_b$ . Any model proposed for generating the array  $b_{i,j}$  should exhibit certain statistical characteristics. Thus, in general, the array  $b_{i,j}$ , while differing in a random manner from  $a_{i,j}$ , should nevertheless be correlated with  $a_{i,j}$  to a degree dependent on the value of the time difference  $t_b - t_a$ . In particular, when  $t = t_a$ , the model must predict  $b_{i,j} = a_{i,j}$  for all  $i$  and  $j$ . For  $t_b$  greater than  $t_a$ , the model should predict a monotonically decreasing value of the quantity  $E[a_{i,j}b_{i,j}]$  as the difference  $t_b - t_a$  increases, and in the limit as  $t_b$  approaches infinity, the expected value  $E[a_{i,j}b_{i,j}]$  should approach zero. In addition, the spatial covariance properties of the  $b$ -array should be identical to the corresponding properties of the  $a$ -array for all values of  $t_b$  and  $t_a$ , at least for time differences  $t_b - t_a$  on the order of a second. In particular, we must have  $E[b_{i,j}] = E[a_{i,j}]$  and  $E[b_{i,j}b_{i+h,j+k}] = E[a_{i,j}a_{i+h,j+k}]$  for all integral values of  $i$ ,  $j$ ,  $h$ , and  $k$ .

Consider a model for  $b_{i,j}$  of the form

$$b_{i,j} = p a_{i,j} + \sqrt{1-p^2} c_{i,j}$$

FIGURE 5-1. SYNTHETIC IMAGE CASE 60, LWIR



FIGURE 5-2. SYNTHETIC IMAGE CASE 60, SWIR



FIGURE 5-3. SYNTHETIC IMAGE CASE 60, SWIR, REDUCED MTF



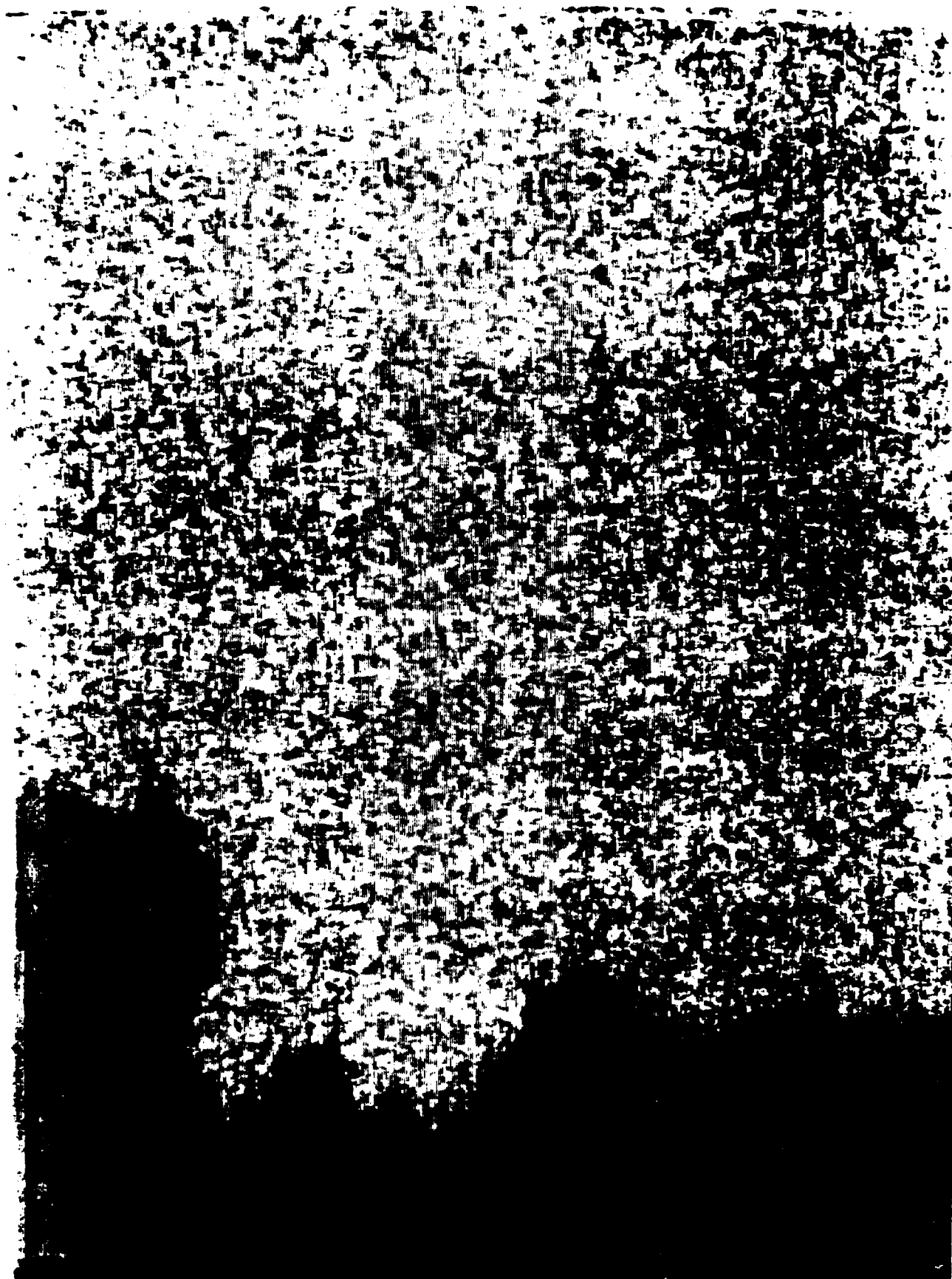
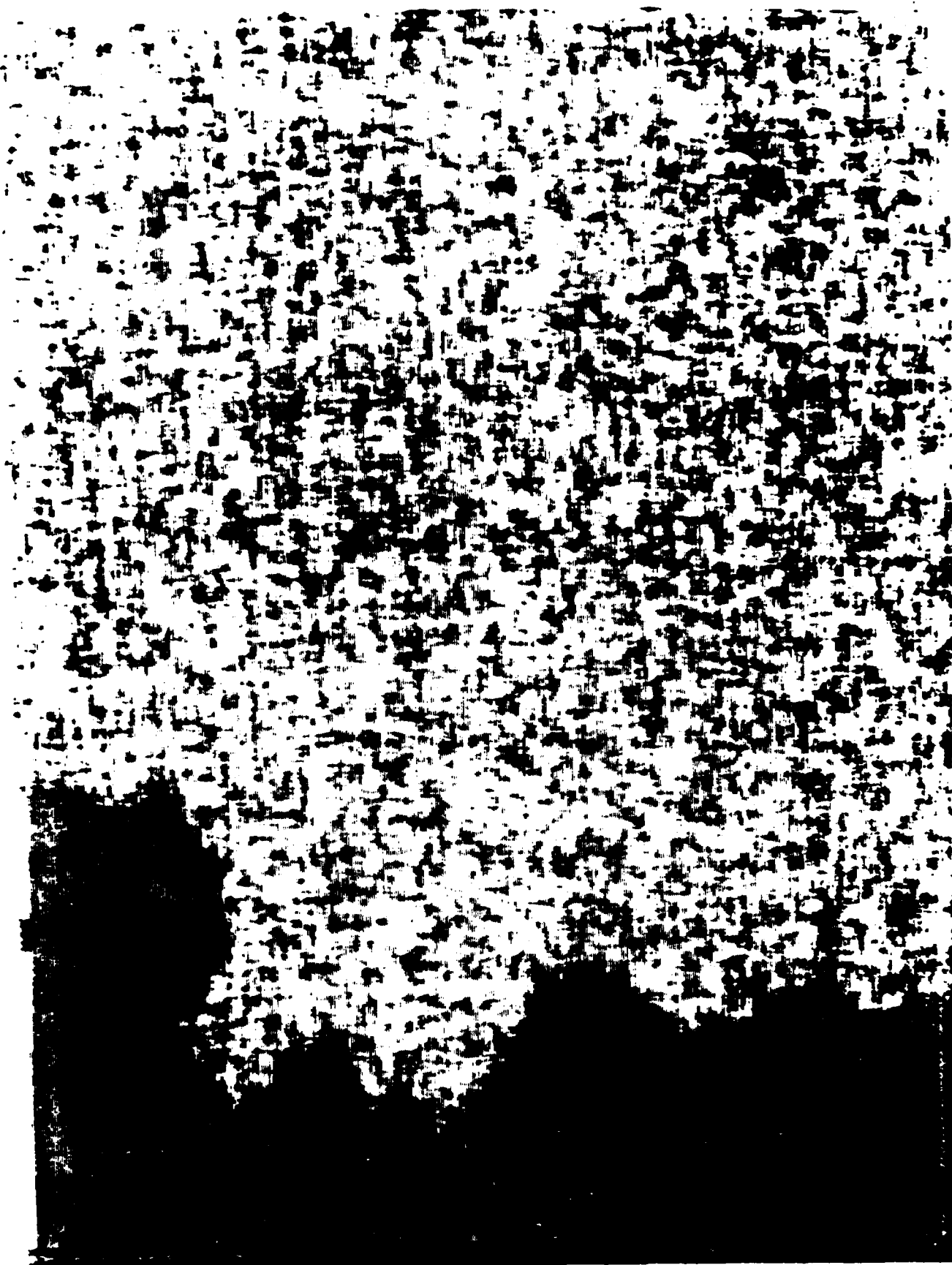


FIGURE 5-4. SYNTHETIC IMAGE CASE 32, LWIR

FIGURE 5-5. SYNTHETIC IMAGE CASE 42, LWIR



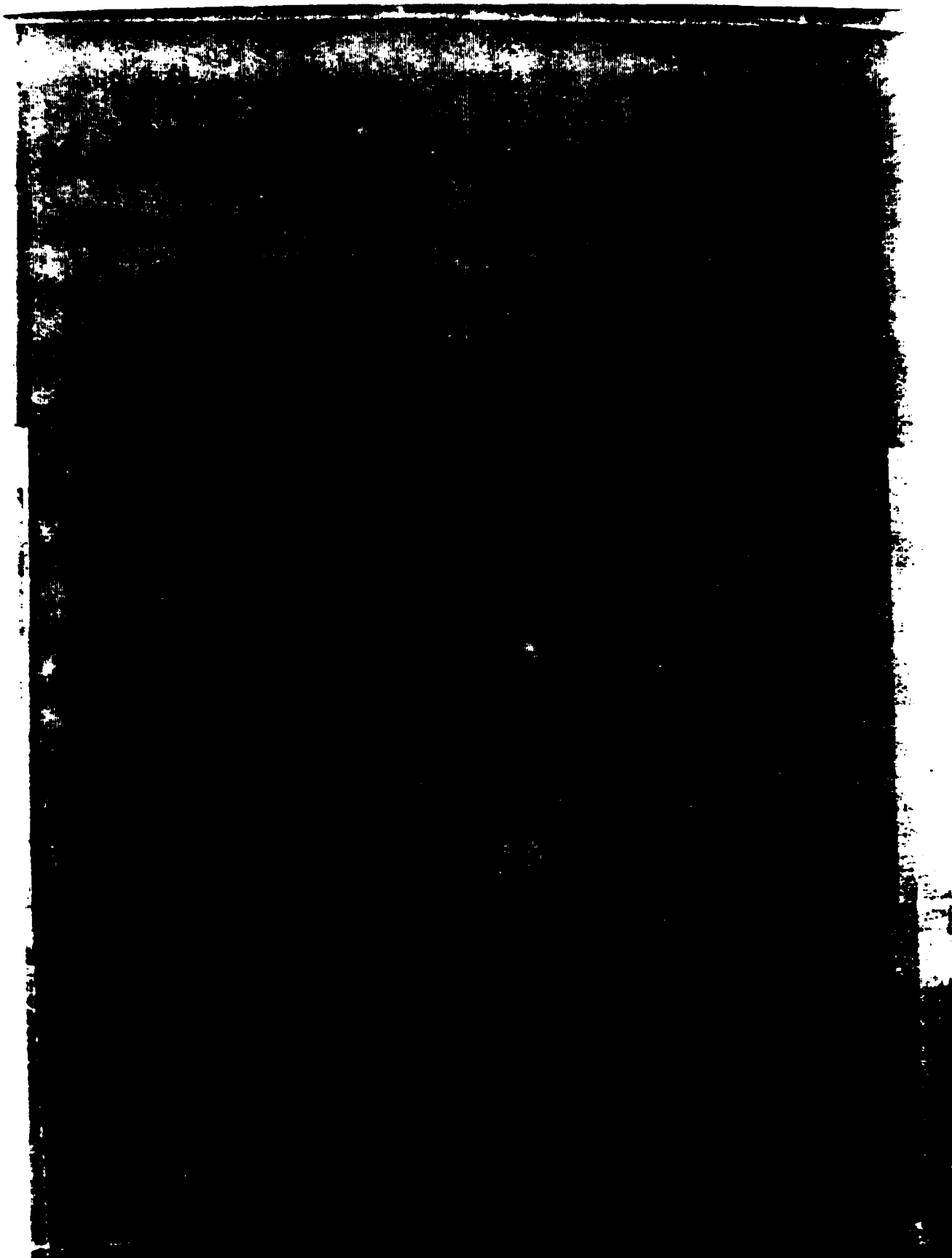
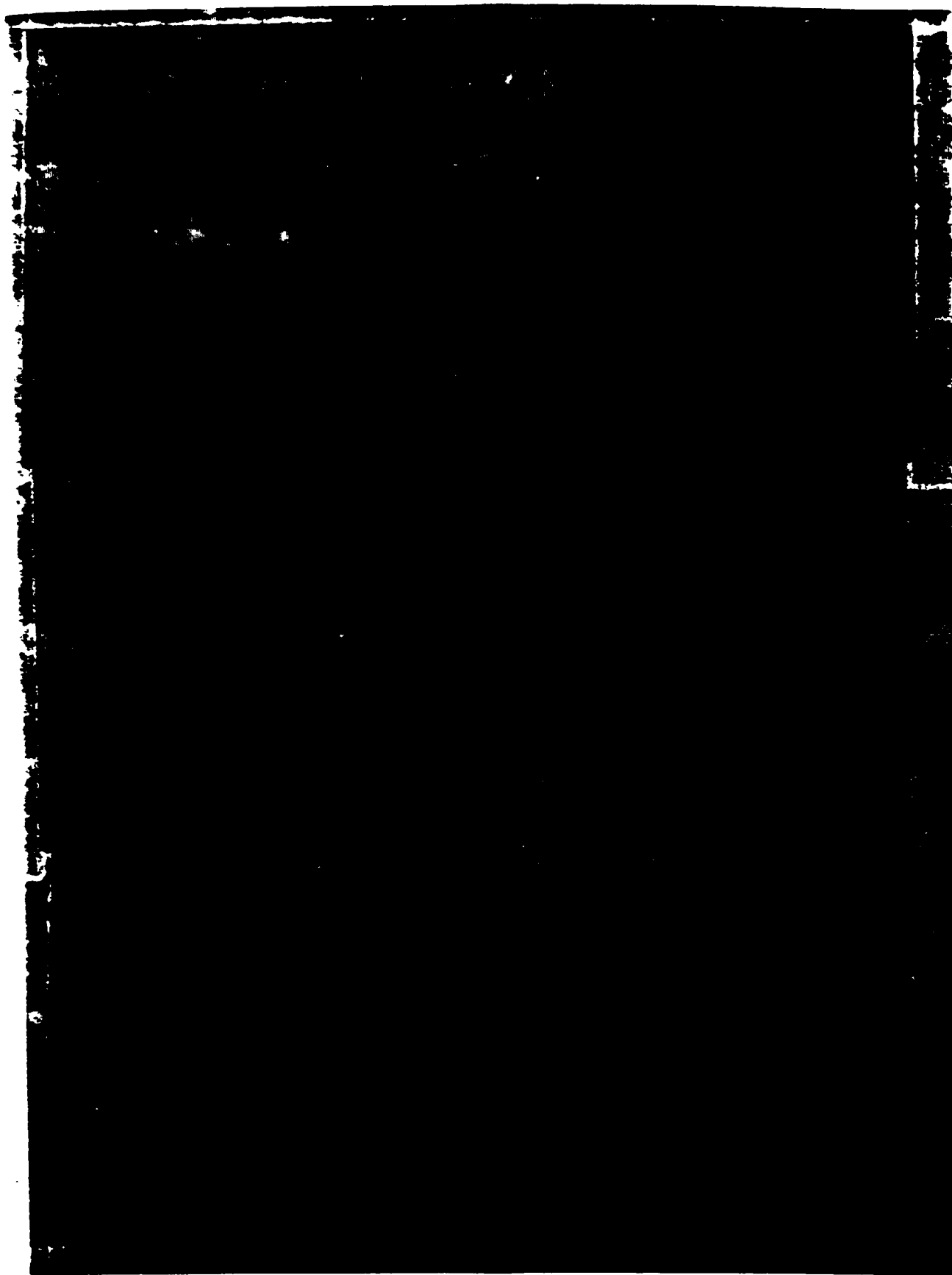


FIGURE 5-6. SYNTHETIC IMAGE CASE 30, LWIR

FIGURE 5-7. SYNTHETIC IMAGE CASE 26, LWIR



The parameter  $p$  is a function of the time  $t_b$  at which the distribution is given by  $b_{i,j}$ . The array  $c_{i,j}$  may be thought of as the radiance distribution existing after an infinite time has elapsed following observation of the distribution  $a_{i,j}$  at time  $t_a$ . A reasonable model for the dependence of  $p$  on the time difference  $t_b - t_a$  is

$$p(t_b - t_a) = \exp[-(t_b - t_a)/\tau]$$

where  $\tau$  is the characteristic time associated with the evolution of the radiance distribution. The value of  $\tau$  could be determined empirically. With this expression for  $p$ , the model for  $b_{i,j}$  becomes

$$\begin{aligned} b_{i,j} &= \exp(-(t_b - t_a)/\tau) a_{i,j} \\ &+ \sqrt{1 - \exp(-2(t_b - t_a)/\tau)} c_{i,j} \end{aligned}$$

which satisfies the requirements discussed above.

where  $E[a_{i,j}] = 0$ , and  $c_{i,j}$  is a new array generated using the same stochastic process as that used in generating the  $a$ -array but statistically completely independent of the  $a$ -array. That is,

$$E[a_{i,j}a_{i+h,j+k}] = E[c_{i,j}c_{i+h,j+k}]$$

for any  $i, j, h$ , and  $k$ , but

$$E[a_{i,j}c_{i+h,j+k}] = 0$$

for all  $i, j, h$ , and  $k$ . Then we have

$$\begin{aligned} E[b_{i,j}b_{i+h,j+k}] &= p^2 E[a_{i,j}a_{i+h,j+k}] \\ &+ (1-p^2) E[c_{i,j}c_{i+h,j+k}] = E[a_{i,j}a_{i+h,j+k}]. \end{aligned}$$

#### REFERENCES

- J. Malik, "Strategic Electro-Optical Systems Availability," SRI Project 1769, August 1982. (AD-E500526)
- A. Fournier, D. Fussell, and L. Carpenter, "Computer Rendering of Stochastic Models," Communications of the ACM, Vol. 25, No. 6, June 1982. p. 371.
- S. Lovejoy, "Area-Perimeter Relation for Rain and Cloud Areas," Science, Vol. 215, 9 April 1982.

## **APPENDIX A. DATA REDUCTION**

This appendix outlines the salient features of the data reduction procedures only to the extent required to appreciate the significance of the data presented in the main body of this report.

### **A.1      TIME CONVERSION**

Throughout the data reduction process, TALO was used exclusively, in particular to merge data from multiple independent data streams. TALO was obtained by subtracting launch time from Greenwich Mean Time (GMT) recorded on the original analog tape. GMT times recorded with IRIG B were used.

### **A.2      RECORDED VOLTAGES**

The detector output voltages are recorded as eight-bit binary words, each of which can assume at most  $2^8$ , or 256, distinct values. The quantizing associated with this recording is designed to remain at less than 5% over the system's dynamic range by use of a piecewise linear compression scheme.

### **A.3      FILTERS**

The decoded PCM data from each detector may be filtered to eliminate noise. The characteristics of the filters used depend on the nature of the noise.

### **A.4      PEAK DETECTION**

Detection of pulses arising from the presence of point sources in the field of view is based on fitting detector-dependent pulse shapes derived from measurements of a calibration point source. The method of least squares is used to determine three free parameters: 1) the pulse amplitude, 2) the local baseline level, and 3) the slope of the local baseline. The variance of the fit is computed and is used as a detection criterion.

When a local maximum in amplitude is detected that exceeds a preset threshold and is coincident (to within a specified tolerance)

with a minimum in standard deviation, a preliminary detection is declared. Following preliminary detection, additional constraints are imposed, as needed, to ensure elimination of noise or radar-induced false targets while retaining the true target.

#### A.5 CONVERSION OF PULSE AMPLITUDE TO PHYSICAL UNITS

Application of the system calibration to target measurements is based on the assumptions that 1) most of the energy in a point source image is distributed over a detector triplet (three adjacent detectors) and 2) the distribution of energy in the focal plane is the same for both target and calibration source images. When more than three adjacent detectors record pulses from a single target, then the detector triplet selected is the one for which the combined pulse is the strongest. However, if fewer than three detectors record pulses (adjacent detector(s) having zero amplitude), the detector registering the larger pulse is selected as the center detector of the triplet.

The three amplitudes of the target pulse are compared to each triplet of the same detector set in the calibration table (refer to Appendix G), and a calibration triplet is selected. The selection is based on how closely the amplitudes of the calibration triplet resemble the target triplet of the same detector set. This criterion ensures that the calibration applied to the target measurements is the one for which the distribution of calibration irradiance over the three detectors most closely matches, within measurement uncertainties, the distribution of target irradiance over the same set of detectors.

The effective irradiance of the target at the GBM system is estimated by the ratio of the measured target triplet pulse to the selected calibration triplet pulse times the calibration source irradiance at the time of the recorded calibration.

#### A.6 COMPUTATION OF RADIOMETRIC PARAMETERS

##### A.6.1 Intensity from Irradiance

The spectral irradiance at an aperture by a source can be given as

$$I_\lambda(\lambda, T) = \frac{a \epsilon(\lambda)}{R^2} N_{bb\lambda}(i, T) \tau(\lambda) , \quad (A-1)$$

where

- a = projected area of the source, assumed to be uniformly heated to temperature T
- R = line-of-sight range to the source (dimensions of length)
- $\epsilon(\lambda)$  = emissivity of the surface of the source, assumed uniform over the area a (dimensionless)
- $N_{bb\lambda}(\lambda, T)$  = spectral radiance of a blackbody at wavelength  $\lambda$  and temperature T as given by the familiar theoretical expression of Planck (dimensions of power · area<sup>-1</sup> · solid angle<sup>-1</sup> · wavelength<sup>-1</sup>)
- $\tau(\lambda)$  = transmission along the line of sight as a function of wavelength (dimensionless)

(U) The effective in-band irradiance (in either band, b),  $\mathcal{H}_{eff_b}$ , is defined as

$$\mathcal{H}_{eff_b} = \int_0^{\infty} \mathcal{H}_{\lambda}(\lambda, T) {}^1R_b(\lambda) d\lambda , \quad (A-2)$$

where  ${}^1R_b(\lambda)$  is a system normalized responsivity of band b at wavelength  $\lambda$ . (This is the total spectral responsivity of the detector as installed in the system and includes the effect of the detector, optics, filter, etc.) The in-band radiant intensity from a source is defined as

$$J_{eff_b}(T) \equiv \int_0^{\infty} J_{\lambda}(\lambda, T) {}^1R_b(\lambda) d\lambda , \quad (A-3)$$

where  $J_{\lambda}(\lambda, T)$  is the spectral radiant intensity of the source at wavelength  $\lambda$ ; and the spectral irradiance is

$$\mathcal{H}_{\lambda} = \frac{J_{\lambda} \tau(\lambda)}{R^2} . \quad (A-4)$$

Therefore, by combining Equations A-3 and A-4,

$$J_{eff_b}(T) = \int_0^{\infty} \frac{\mathcal{H}_{\lambda} R^2}{\tau(\lambda)} {}^1R_b(\lambda) d\lambda . \quad (A-5)$$

Since GBM is a two-color system and cannot make spectral measurements, the effective in-band irradiance,  $\mathcal{H}_{\text{eff},b}$ , is extracted using the method described in Section A.5 rather than  $\mathcal{H}_\lambda$  being measured directly. In order to evaluate Equation A-5,  $\tau(\lambda)$ , as weighted by  $\mathcal{H}_\lambda$  and  $^1R_b(\lambda)$ , must be estimated. The atmospheric transmittance  $\bar{\tau}_b(T)$  is estimated by a wavelength-independent quantity  $\bar{\tau}_b(T)$  defined as

$$\bar{\tau}_b(T) \equiv \frac{\int_0^\infty J_\lambda(\lambda, T) \tau(\lambda) ^1R_b(\lambda) d\lambda}{\int_0^\infty J_\lambda(\lambda, T) ^1R_b(\lambda) d\lambda} , \quad (\text{A-6})$$

where

$J_\lambda(\lambda, T)$  = spectral radiant intensity of the source as predicted by the OSC

$\tau(\lambda)$  = atmospheric transmission as calculated using LOWTRAN 4

By substituting  $\bar{\tau}$  for  $\tau(\lambda)$  in Equation A-5

$$J_{\text{eff},b}(T) = \frac{R^2}{\bar{\tau}} \int_0^\infty \mathcal{H}_\lambda ^1R_b(\lambda) d\lambda , \quad (\text{A-7})$$

and by substituting Equation A-5, the working equation is obtained:

$$J_{\text{eff},b} = \frac{\mathcal{H}_{\text{eff},b}}{\bar{\tau}} R^2 . \quad (\text{A-8})$$

#### A.5.2 Two-Color Parameters

Calculation of the the two-color parameters, which are two-color temperature (T), emissivity area (ea), and broadband intensity (J), is described below.

The two-color temperature is calculated from the ratio

$$r(T) = \frac{J_{\text{eff},B}}{J_{\text{eff},A}} = \frac{\int_0^\infty J(\lambda, T) ^1R_B(\lambda) d\lambda}{\int_0^\infty J(\lambda, T) ^1R_A(\lambda) d\lambda} , \quad (\text{A-9})$$

where the subscript B refers to the SWIR band and the subscript A refers to the LWIR band.  $J_{\text{eff}}$  is defined in Equation A-3. Substituting  $J(\lambda, T) = \epsilon(\lambda) a N_{\text{bb}}(\lambda, T)$  in Equation A-3 gives

$$J_{\text{eff}} = a \int_0^{\infty} \epsilon(\lambda) N_{\text{bb}}(\lambda, T) ^1R_B(\lambda) d\lambda \quad (\text{A-10})$$

and Equation C-9 becomes

$$r(T) = \frac{a_B \int_0^{\infty} \epsilon(\lambda) N_{\text{bb}}(\lambda, T) ^1R_B(\lambda) d\lambda}{a_A \int_0^{\infty} \epsilon(\lambda) N_{\text{bb}}(\lambda, T) ^1R_A(\lambda) d\lambda} \quad (\text{A-11})$$

There are four unknowns in Equation A-11: the emitting areas of the target in the LWIR and SWIR bands,  $a_A$  and  $a_B$ , and the spectral emittances in each band. If it is assumed that the emittance ( $\lambda$ ) is wavelength independent and that  $a_A = a_B$ , and the appropriate cancellations are made in Equation A-11,

$$r(T) = \frac{\int_0^{\infty} N_{\text{bb}}(\lambda, T) ^1R_B(\lambda) d\lambda}{\int_0^{\infty} N_{\text{bb}}(\lambda, T) ^1R_A(\lambda) d\lambda} \quad (\text{A-12})$$

The integrals appearing in Equation A-11 were evaluated numerically using 16-point Gaussian quadrature. Figure A-1 is a plot of  $r(T)$  as a function of temperature.

One determines the color-temperature from the mission data by associating the effective radiant intensities (obtained from the measured irradiances by means of Equation A-8) with the temperature in Figure A-1.

The emissivity area ( $a\epsilon$ ) is found using the two-color temperature and Equation A-10. One further assumes that the emissivity  $\epsilon(\lambda)$  is independent of the wavelength. Solving Equation A-10 for the emissivity area gives

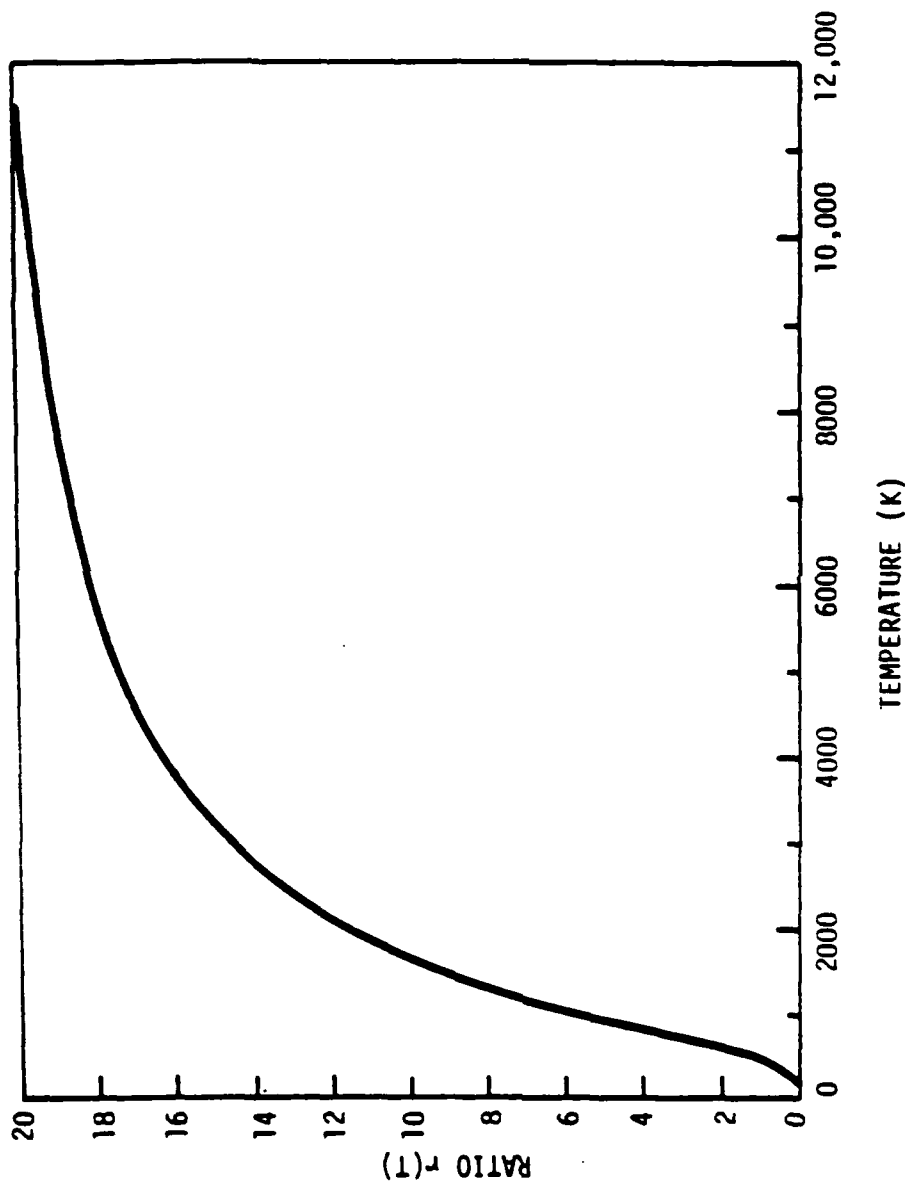


FIGURE A-1. RATIO OF EFFECTIVE INTENSITIES AS A FUNCTION OF TEMPERATURE

$$a\varepsilon = \frac{J_{\text{eff}_b}}{\int_0^{\infty} N_{bb}(\lambda, T) R_b(\lambda) d\lambda}, \quad (\text{A-13})$$

where either waveband may be used, the results being identical in the two cases.

The total broadband radiant intensity of the source is computed using the Steffan-Boltzmann law expressed by

$$J = \frac{a\varepsilon \sigma T^4}{\pi}, \quad (\text{A-14})$$

where  $\sigma$  is the Steffan-Boltzmann constant,  $a\varepsilon$  is given by Equation A-13, and  $T$  is the two-color temperature.

#### A.6.3 Smoothing Techniques

The effective irradiance and the effective radiant intensity are smoothed by a running average taken over a 0.5-sec interval of data (15 adjacent SFOVs). For this average to be calculated, at least eight SFOVs must contain valid data. For each interval, the averaged data are assigned the altitude of the midpoint of the interval. This interval is then stepped one SFOV at a time, and the procedure repeated.

#### A.6.4 Standard Deviation

For single-color parameters ( $\mathcal{H}_A$ ,  $\mathcal{H}_B$ ,  $J_A$ , and  $J_B$ ), the standard deviations are defined as

$$\pm\sigma_{\mathcal{H}_{\text{eff}_b}} = \left[ \frac{\sum (\mathcal{H}_{\text{eff}_b} - \bar{\mathcal{H}}_{\text{eff}_b})^2}{N - 1} \right]^{\frac{1}{2}} \quad (\text{A-15})$$

$$\pm\sigma_{J_{\text{eff}_b}} = \left[ \frac{\sum (J_{\text{eff}_b} - \bar{J}_{\text{eff}_b})^2}{N - 1} \right]^{\frac{1}{2}} \quad (\text{A-16})$$

where

$\bar{\mathcal{H}}_{\text{eff}_b}$  = mean value of effective irradiance

$\bar{J}_{\text{eff}_b}$  = mean value of effective radiant intensity

$N$  = number of points being averaged.

For two-color parameters, the standard deviations are defined as

$$\pm\sigma_T = f \mp Q(T) \quad (A-17)$$

where  $f$  is the function referred to in Equation A-10 and

$$Q = \frac{J_{eff_1} \pm \sigma_{J_{eff_1}}}{J_{eff_1} \mp \sigma_{J_{eff_2}}} \quad (A-18)$$

This method of defining  $\sigma_T$  propagates the  $\sigma_{Jeff_b}$  errors under a worst-case assumption. Similarly, worst-case error propagation is used in calculating the errors of  $\sigma_a$  and  $\sigma_J$ .

#### A.7 PRECISION AND REPEATABILITY

Definitions of precision and repeatability have been adapted to GBM data as follows: precision denotes the degree of scatter in each mission's data and is defined at a given altitude as

$$\sigma_A = \sqrt{\frac{\sum_{i=1}^N (X_i - u)^2}{N-1}} \quad (A-19)$$

where

- $X_i$  = the measured radiometric values
- $u$  = the average value of  $X_i$  over the 0.5-sec smoothing interval
- $N$  = the number of measurements during the smoothing interval.

Precision is expressed in percent and is the average of the precision at each altitude for the entire LWIR or SWIR data span:

$$\sigma = \sum_{A=1}^K \frac{\sigma_A}{u} 100/K \quad (A-20)$$

where  $K$  is the number of altitudes for which  $\sigma_A$  is calculated.

Repeatability denotes the degree of disagreement between data sets (missions) separated by a significant amount of time and is defined at a given altitude as

$$\sigma_A = \sqrt{\frac{\sum_{i=1}^M (u_i - \bar{u})^2}{M-1}} \quad (A-21)$$

where

$u_i$  = the smoother radiometric data of mission  $i$  at a given altitude

$\bar{u}$  = the average of  $u_i$  over all missions

$M$  = the number of missions ( $M \geq 2$ ).

Repeatability is expressed in percent and is the average of the repeatability at overlapping altitudes:

$$\rho = \sum_{A=1}^L \frac{\sigma_A}{\bar{u}} 100/L \quad (A-22)$$

where  $L$  is the number of altitudes for which overlapping data (data taken at altitudes of mutual coverage) exist ( $L \geq 2$ ). These altitudes of mutual coverage have been interpolated to even altitudes at 2-km intervals. For data gaps greater than twice the smoothing interval, the interpolated value of  $\sigma_A$  has been omitted.

## APPENDIX B. CALIBRATION

### B.1 MEASUREMENTS

Following the mission, and prior to securing the GBM Sensor System from its operational cooled status, a postmission radiometric calibration is recorded. This calibration is used as a record of the detector responsibility for the mission, and is performed as closely as practical to the time of, and under the same conditions as, the mission being recorded. This calibration is verified by use of a premission calibration.

The radiometric calibration is performed using the calibration collimator designed especially for this purpose. Basically, the collimator consists of a graybody source controllable over the range from about 300 to 1200 K, a set of apertures that may be placed in front of the graybody, and a system of collimating optics that present to the sensor a virtual source at infinite range. While the GBM tracking pedestal is held at the central azimuth location and the GBM primary telescope is moved in elevation, the graybody image is slowly stepped up or down the focal plane over the elevation field of view.

The calibration coefficients have been derived using these data and various assumptions. Many of the assumptions have been verified to within limits by analysis of more extensive calibrations, such as those that were performed during laboratory tests prior to shipment of the GBM system to Roi Namur for installation.

One assumption used in calibration is that the GBM system is a linear system, since evidence accumulated thus far suggests that the sensor response is nearly linear over its full dynamic range. Another important assumption used in calibration is that the response of the system to a point target can be described by a triplet of voltage values. This is apparent from observations that the voltage values from a point target are frequently detected by more than one detector, while hits on three adjacent detectors are very common.

### B.2 THEORY

Calibration of the sensor is based on the premise that one can, through a combination of measurements, calculate the effective

irradiance present at the sensor. The calibration method applied requires only that the energy distributions in mission and calibration source images be similar. This allows data obtained with both focused and moderately defocused systems to be reduced. The method allows the total irradiance to be determined even when a portion of the energy falls on an inactive detector element.

The basic theory employed in computing the effective irradiance produced by an unresolved source is based on the condition that the source irradiance  $h_b$  during a single calibration run need only remain constant during the recording of any voltage triplet. These voltage triplets thus satisfy an equation of the form

$$\mathcal{H}_b[v_{b(j-1)i}, v_{bj}, v_{b(j+1)i}] = h_b = \text{constant}, \quad (B-1)$$

where

$v_{bj}$  = measured waveform voltage above the local baseline of the  $j$ th detector in spectral band  $b$  of the  $i$ th pulse

$h_b$  = source irradiance at the sensor in spectral band  $b$ .

This function  $\mathcal{H}_b$  has, assuming only linearity of detector response, the property

$$\mathcal{H}[\delta v_{b(j-1)}, \delta v_{bj}, \delta v_{b(j+1)}] = \delta \mathcal{H}_b[v_{b(j-1)}, v_{bj}, v_{b(j+1)}], \quad (B-2)$$

where  $\delta$  is any arbitrary factor. Choosing  $\delta$  equal to the square root of the sum of the squares of the triplet voltage yields

$$\mathcal{H}_b[v_{b(j-1)}, v_{bj}, v_{b(j+1)}] = |v|_{bj} \mathcal{H}_b(a_{bj}, \beta_{bj}, \gamma_{bj}), \quad (B-3)$$

where

$$|v|_{bj} = [v_{b(j-1)}^2 + v_{bj}^2 + v_{b(j+1)}^2]^{\frac{1}{2}}$$

$$a_{bj} = v_{b(j-1)} / |v|_{bj},$$

$$\beta_{bj} = v_{bj} / |v|_{bj},$$

$$\gamma_{bj} = v_{b(j+1)} / |v|_{bj}.$$

This choice of  $\delta$  permits  $\mathcal{K}_b$  to be expressed as the product of two factors, one of which depends only on the direction cosines in the voltage domain. Expressed in this manner  $\mathcal{K}_b$  represents a universal function that is independent of the particular irradiance used in obtaining the calibration data. The unknown irradiance can therefore be obtained by multiplying  $|v|_{bji}$  by  $\mathcal{K}_b$ .

### B.3 NOISE CONSIDERATIONS

Assuming that errors in the measurements caused by random fluctuations (noise) are additive and normally distributed about the mean value, then each member of a measured voltage triplet may be represented in the form  $V = \bar{V} + \Delta V$ , where  $\bar{V}$  is the true (mean) value and  $\Delta V$  is the random error, which is normally distributed having the variance  $\sigma_v^2$ . The variance may be different for each detector element.

This leads to the concept of a "resolution cell" in the voltage domain. The cell is ellipsoidal in shape and is described by the function

$$\frac{[v_{(j-1)} - \bar{v}_{(j-1)}]^2}{\sigma_{(j-1)}^2} + \frac{(v_j - \bar{v}_j)^2}{\sigma_j^2} + \frac{[v_{(j+1)} - \bar{v}_{(j+1)}]^2}{\sigma_{(j+1)}^2} = \text{constant} \quad (B-4)$$

where  $\sigma_j^2 = \sigma_v^2$  for detector J, etc. The value of the constant in Equation B-4 is somewhat arbitrary, but if the 50% point is selected, the value is 2.36606. and there is a 50% probability that the observed triplet  $v_{(j-1)}, v_j, v_{(j+1)}$  falls within the ellipsoid so defined.

The existence of a resolution cell of finite size in voltage space suggests that, within the allowed finite ranges of voltages, there are only a finite number of distinguishable resolution cells. In particular, if the number of voltage triplets measured during calibration exceeds the number of distinguishable resolution cells in voltage space as determined by random noise, it is justified to combine some of the measured triplets by averaging to reduce the total number.

Therefore, for each pair r, s ( $r < s$ ,  $s = 1$  to n, where n is the total number of voltage triplets for one detector triplet), the value of  $Q_{rs}$  is found by

$$Q_{rs} = \left\{ \frac{[v_{(j-1)r} - v_{(j-1)s}]^2}{\sigma_{(j-1)}^2} + \frac{(v_{jr} - v_{js})^2}{\sigma_j^2} + \frac{[v_{(j+1)r} - v_{(j+1)s}]^2}{\sigma_{(j+1)}^2} \right\} W_x .$$

B-5

where  $W_x$  is the smaller of  $W_r$  and  $W_s$ . The inclusion of the factor  $W_x$  in the formula for  $Q_{rs}$  reflects the shrinking size of the resolution cell when points are combined and makes it less likely that two points having large and nearly equal weights will be combined. The general effect is to cause "clusters" of points in voltage space to coalesce to a single point each, with the weights of the final set corresponding to the number of points in each original cluster. Let  $Q_{kl}$  denote the smallest  $Q_{rs}$  calculated above. If  $Q_{kl} \leq 2.36606$ , then the points  $k$  and  $l$  are combined by averaging according to the formulas

$$\begin{aligned}\bar{W} &= W_k + W_l , \\ \bar{v}_{(j-1)} &= [W_k v_{(j-1)k} + W_l v_{(j-1)l}] / \bar{W} , \\ \bar{v}_j &= (W_k v_{jk} + W_l v_{jl}) / \bar{W} , \\ \bar{v}_{(j+1)} &= [W_k v_{(j+1)k} + W_l v_{(j+1)l}] / \bar{W} .\end{aligned}\quad (B-6)$$

The two original points  $k$  and  $l$  are then replaced by the single average point, thereby reducing the total number by one. The process is repeated until  $Q_{kl} > 2.36606$ .

When no more points can be combined, the resulting triplet voltages are converted to direction cosines ( $\alpha_{bjk}, \beta_{bjk}, \gamma_{bjk}$ ) which together with the voltages  $v_{bjk}$  constitute the calibration table for the center detector.

#### B.4 CALIBRATION FACTORS

The calibration factors were derived by measuring the  $v_{bjk}$  value of the waveform voltage above the local baseline. These factors were obtained as the constant image of the collimating graybody source slowly moved down each detector in elevation. Different responsivities were measured when the secondary mirror scanned the image across the focal plane right to left and when it scanned left to right (see Figure 2-3

for focal plane detector arrangement). This direction-correlated effect was accounted for in extraction of the intensities.

Normally, mission data are converted to engineering units on the basis of calibration data recorded immediately before and/or after the mission. However, in the case of mission STM-13W, calibration data were recorded only on two detectors of the LWIR array and two detectors of the SWIR array. The reduction process requires a calibration for each detector separately; therefore, the calibration data recorded for mission GT 134M were substituted in the conversion of measured voltages to units of irradiance. This calibration file was selected because it was of good quality and was close in time to STM-13W.

To compensate for the relative responses of the detectors between the calibrations, it was necessary to develop and apply a set of correction factors. These procedures are outlined in Figure B-1. As shown in the figure, the substituted calibration data were processed in the normal manner to generate a calibration file. Voltage peaks for the mission calibrations were read by hand from strip charts and converted to irradiances by means of the substituted calibration file. Since the effective irradiances during the mission calibrations are known, the departure of the "calibration" irradiances from this value represents the error to be corrected using suitable correction factors.

Correction factor:  $C_i^{\pm}$  defined by

$$C_i^{\pm} = H_k \langle H_i^{\pm} \rangle$$

B-7

were developed, where  $i = 1, 2, \dots, 31$  identifies the particular LWIR detector and  $\pm$  indicates the direction of scanning. The symbol  $\langle H_i^{\pm} \rangle$  denotes the average value of the "calibration" irradiance for the  $i$ th detector and the  $\pm$  scan direction. Finally, the correction factors are used together with the calibration data file to convert the mission voltages to irradiance values.

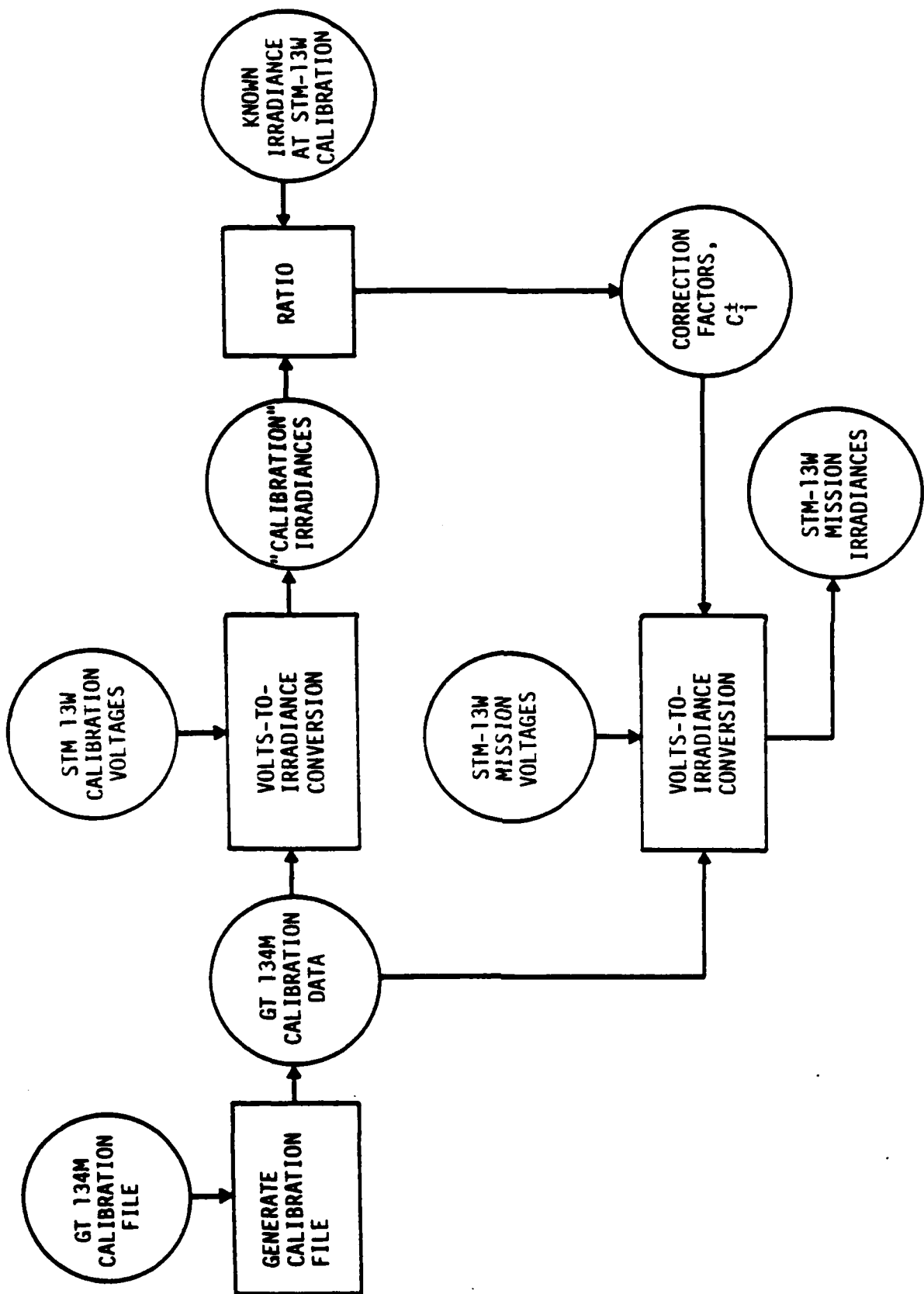


FIGURE B-1. SCHEMATIC DIAGRAM ILLUSTRATING THE METHOD OF DEVELOPING AND APPLYING CORRECTION FACTORS  $C_i^t$  TO COMPENSATE FOR CHANGE IN RELATIVE RESPONSE OF DETECTORS ON MISSION STM-13W

## APPENDIX C. METEOROLOGY

### C.1 RADIOSONDE BALLOON FLIGHTS

For each GBM mission, radiosonde balloon flights were conducted to collect meteorological data supporting the Army Optical Station. These data included: wind direction, wind speed, temperature, dew point, pressure, density, absolute and relative humidity, index of refraction, visibility, and wind shear as a function of altitude between 12 and 100,000 ft.

Those data of most interest in the analysis of clouds are the temperature and dew point profiles. These are plotted for the cases of interest between 0 and 40,000-ft altitude in Figures C-1 through C-18.

### C.2 CLOUD RANGE ESTIMATES

A rough estimate of the range to an observed cloud can be determined using the boresight tracking data of Appendix C and the Temperature and Dew Point Profiles. These estimates are determined assuming that the temperature and/or dew point inversions as illustrated in Figure C-19 indicate the average altitude for cloud formations. Then, using the boresight elevation of the cloud measurement and simple trigonometry, a rough estimate of the cloud range is made. The range error associated with such an estimate is given by,

$$\sigma_R = \frac{1}{\sin \theta} \sqrt{\sigma_h^2 + \sigma_\theta^2 \frac{h^2}{\tan^2 \theta}} , \quad (C-1)$$

where the elevation angle error  $\sigma_\theta$  is insignificant compared to the altitude error  $\sigma_h$ ; hence Equation C-1 reduces to

$$\sigma_R \approx \frac{\sigma_h}{\sin \theta} , \quad (C-2)$$

where

$\sigma_h$  = altitude error (1 sigma)

$\theta$  = measured elevation angle of cloud.

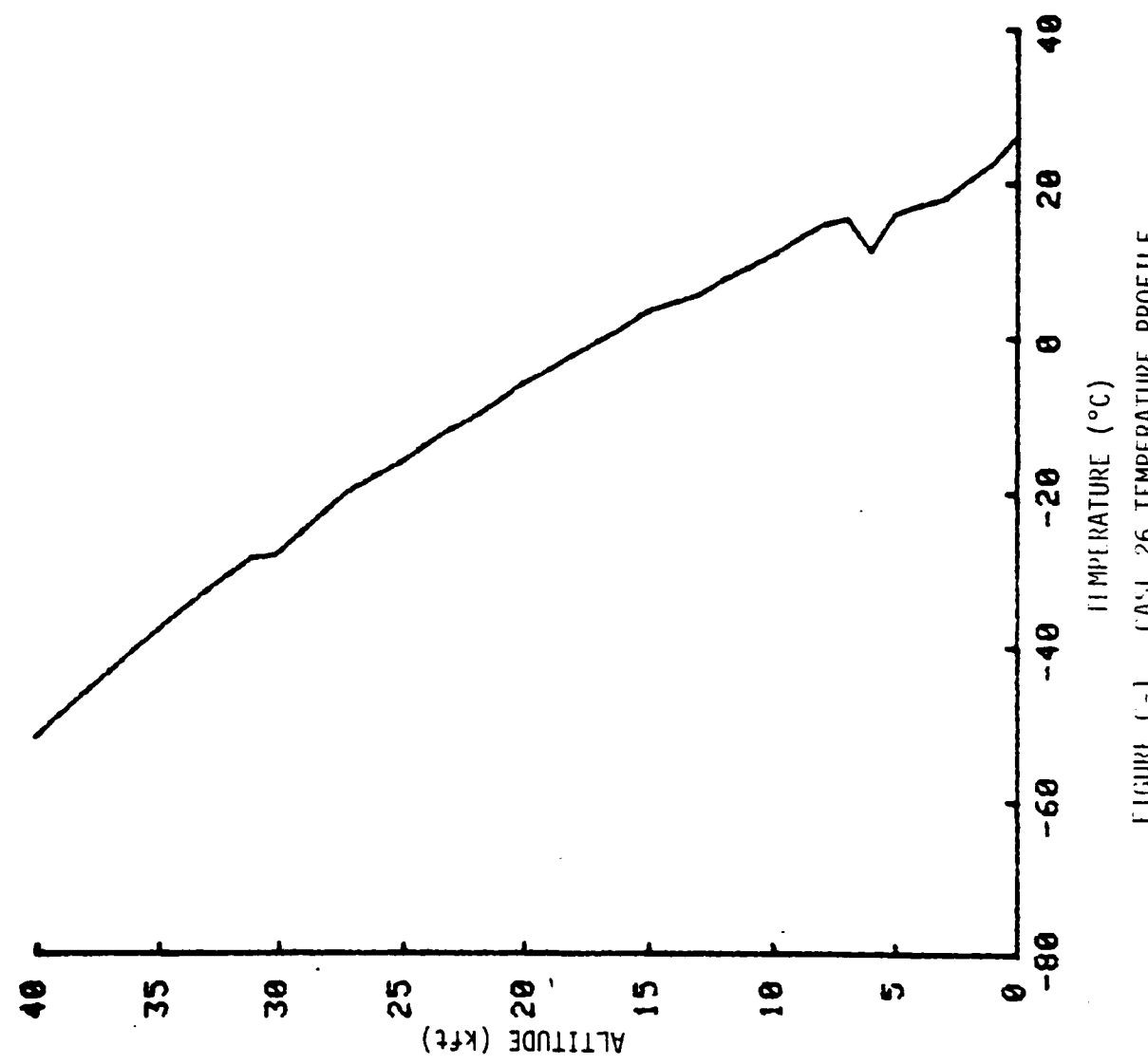


FIGURE C-1. CASI 26 TEMPERATURE PROFILE

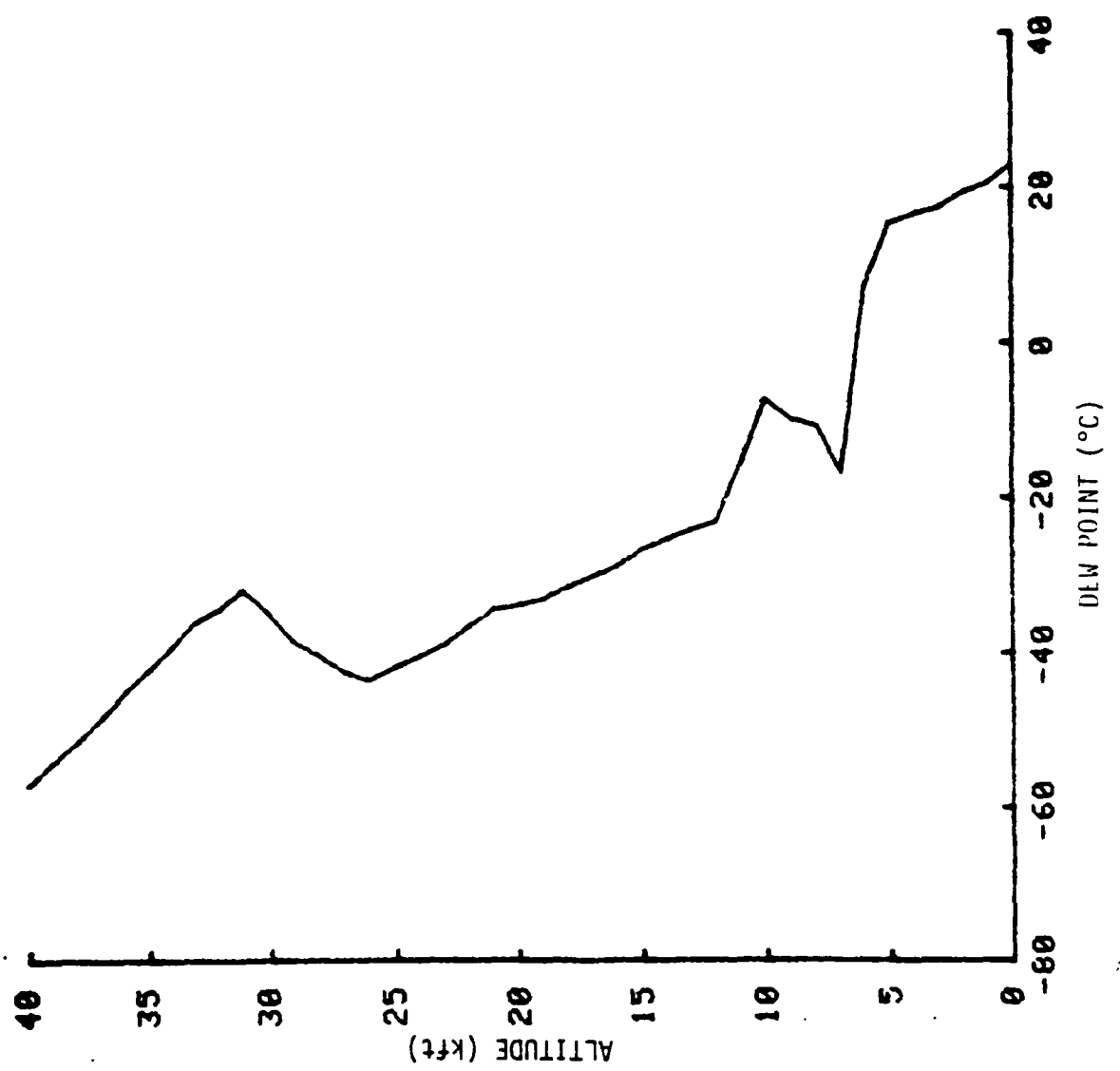


FIGURE C-2. CASE 26 DEW POINT vs ALTITUDE

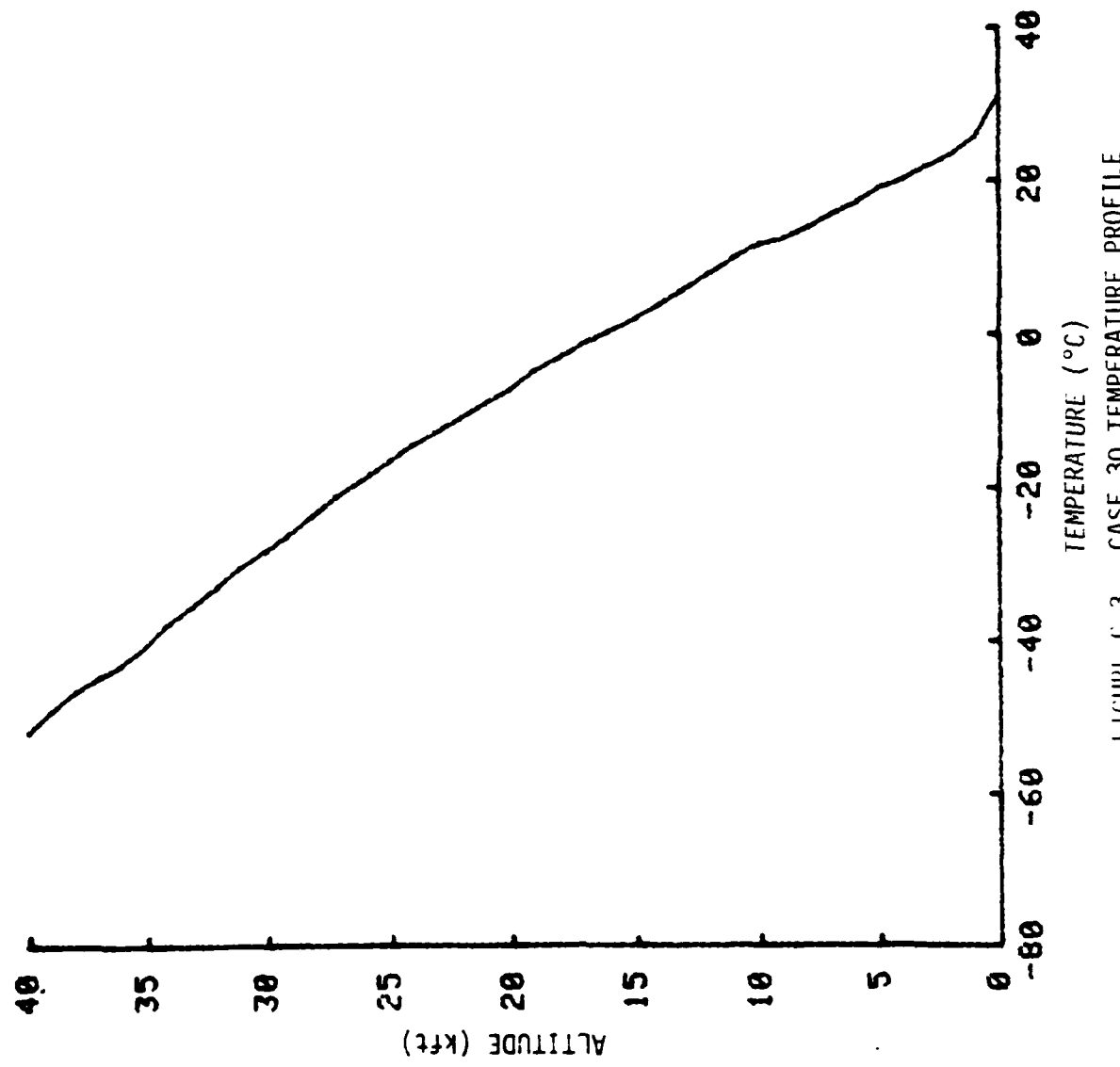


FIGURE C-3. CASE 30 TEMPERATURE PROFILE

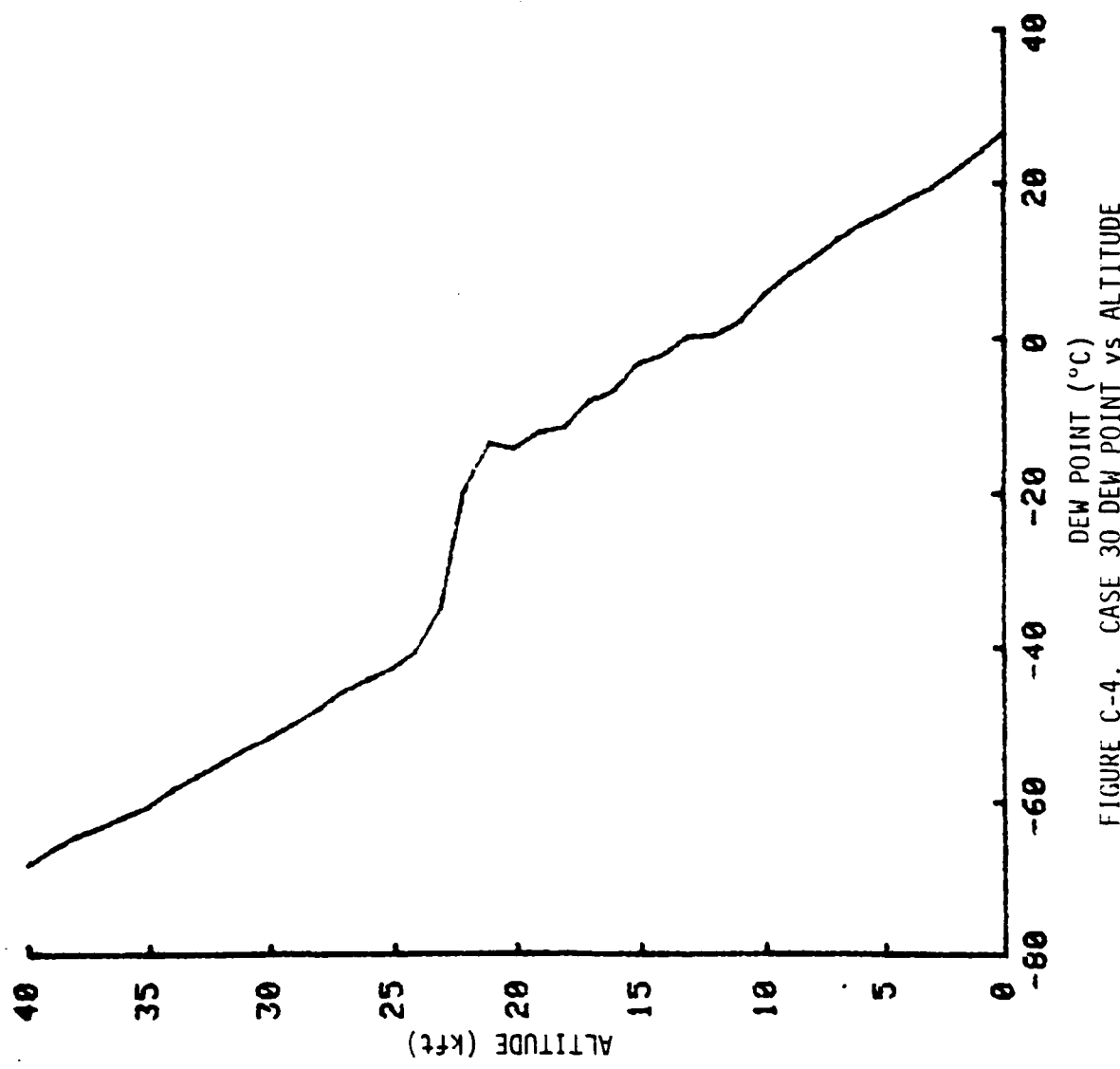


FIGURE C-4. CASE 30 DEW POINT vs ALTITUDE

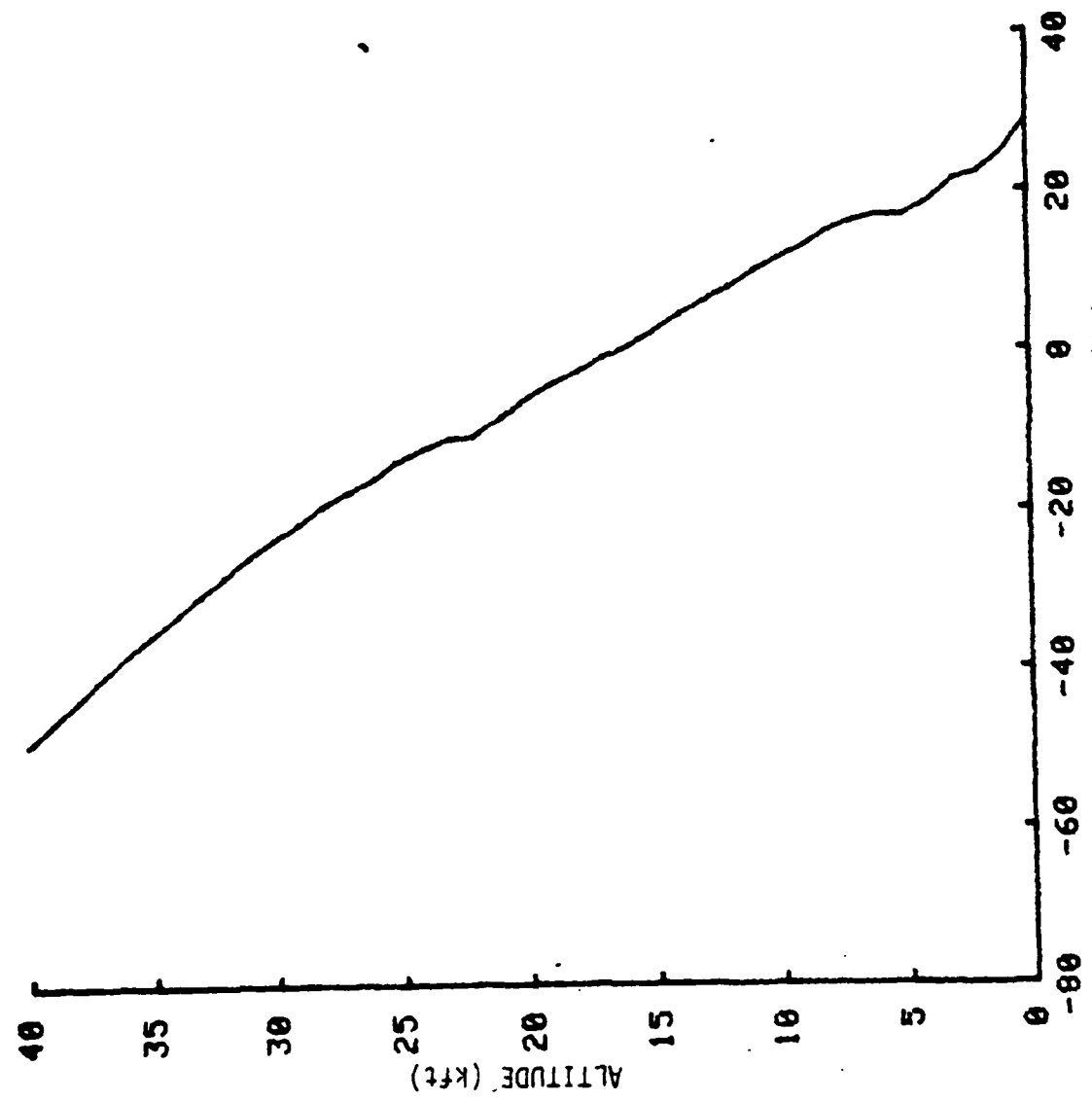


FIGURE C-5. CASE 34 TEMPERATURE PROFILE

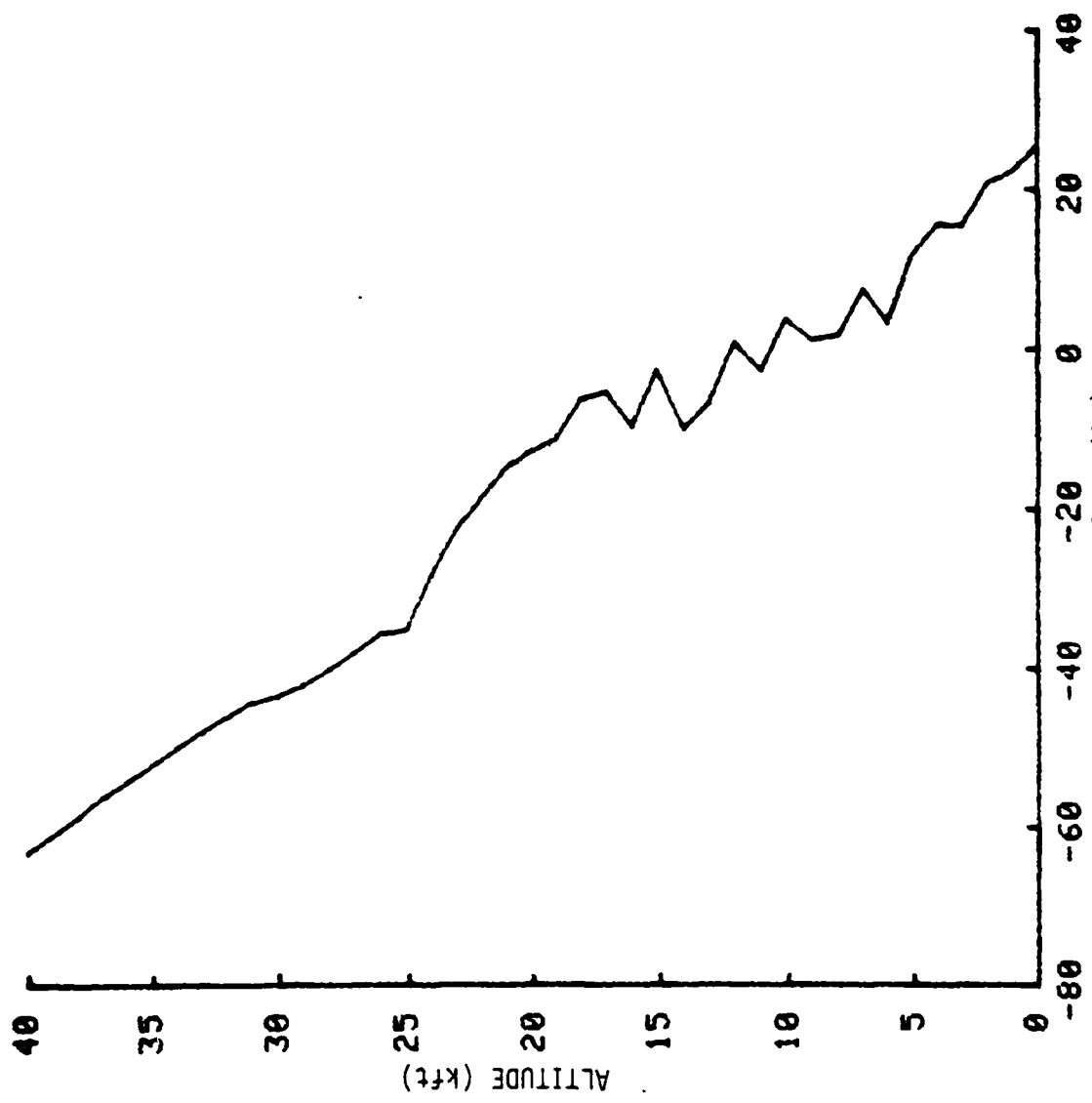


FIGURE C-6. CASE 34 DEW POINT VS ALTITUDE

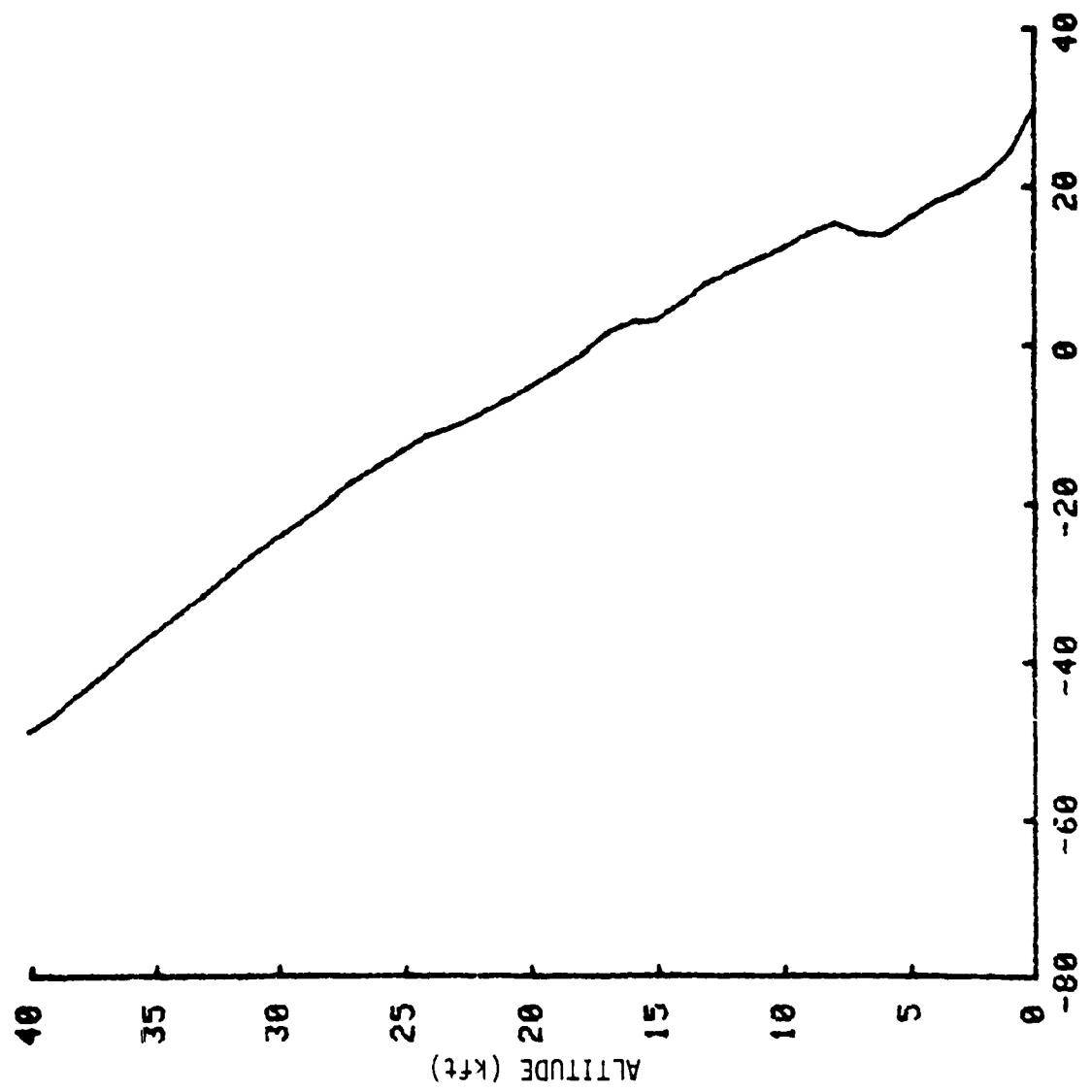
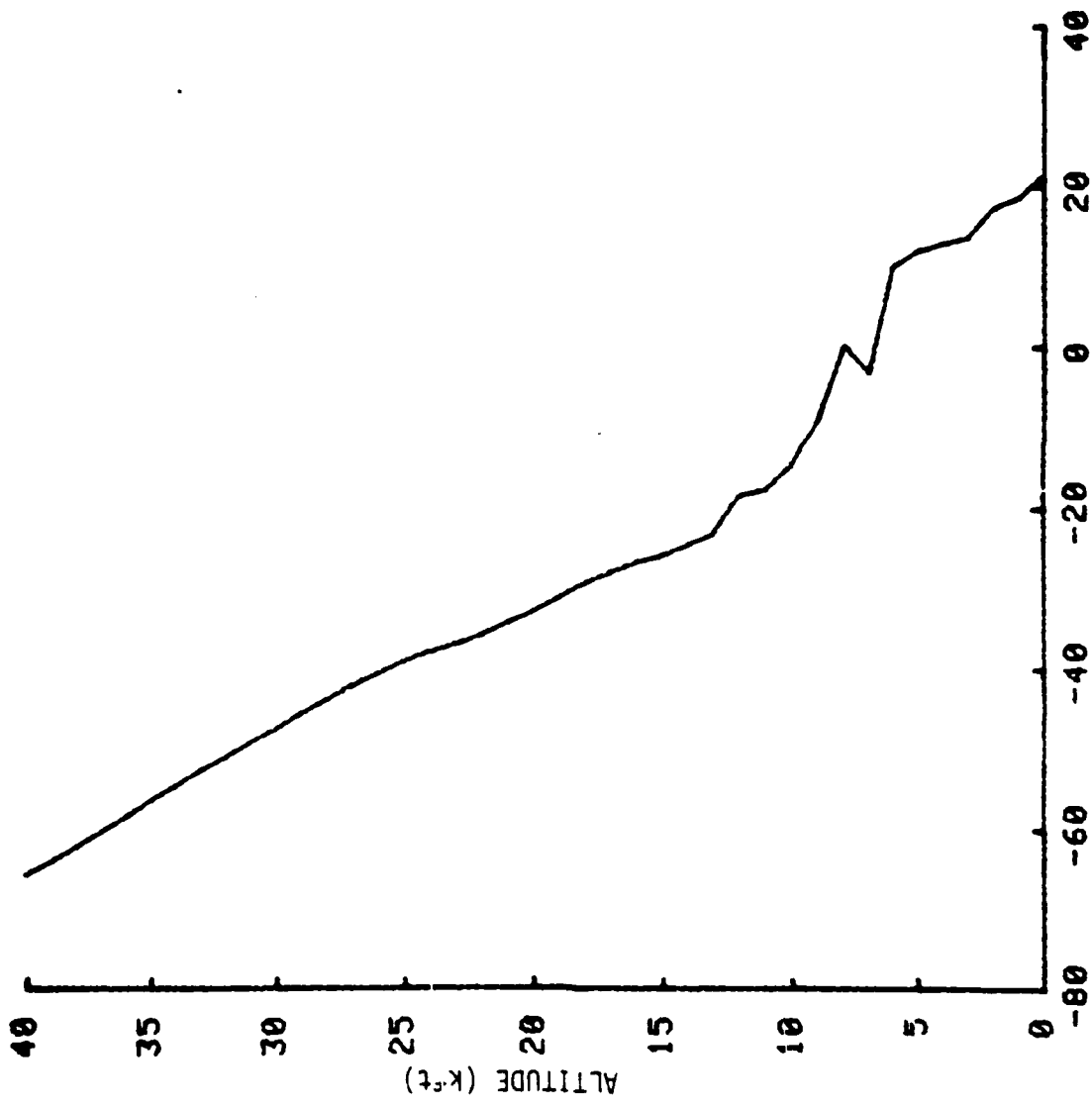


FIGURE C-7. CASE 42 TEMPERATURE PROFILE

FIGURE C-8. CAST 42 DEW POINT vs ALTITUDE



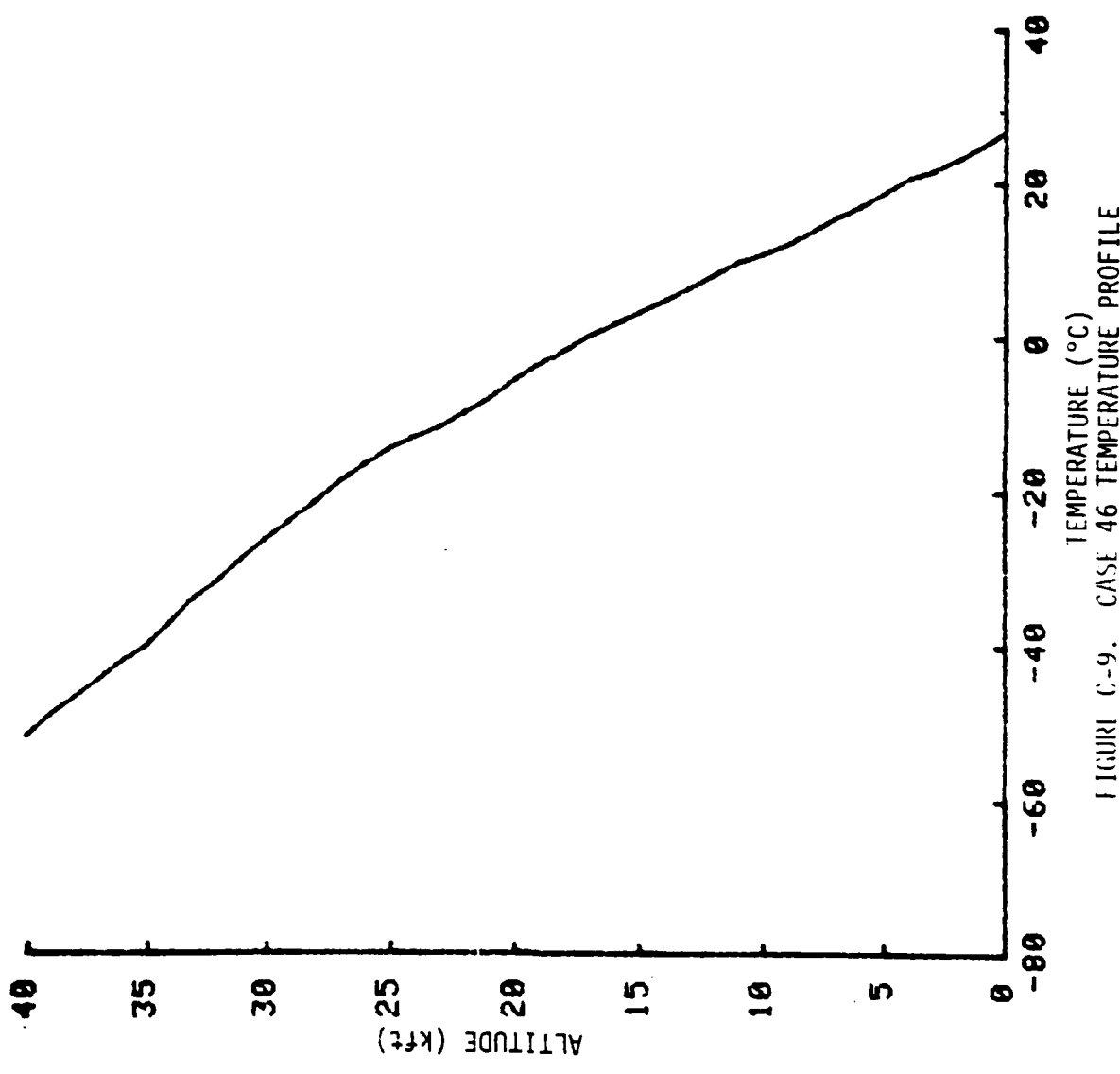


FIGURE C-9. CASE 46 TEMPERATURE PROFILE

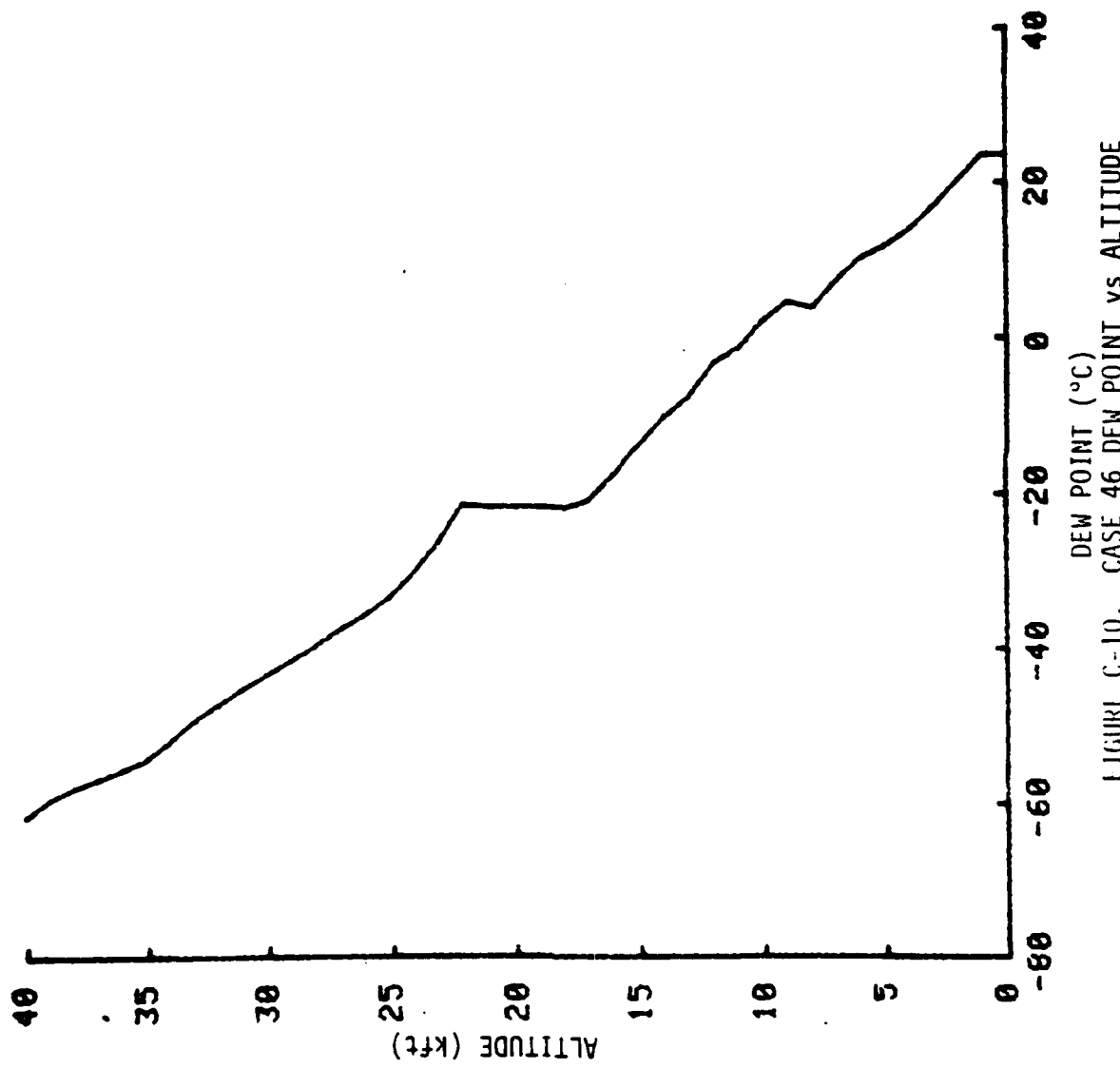


FIGURE C-10. CASE 46 DEW POINT vs ALTITUDE

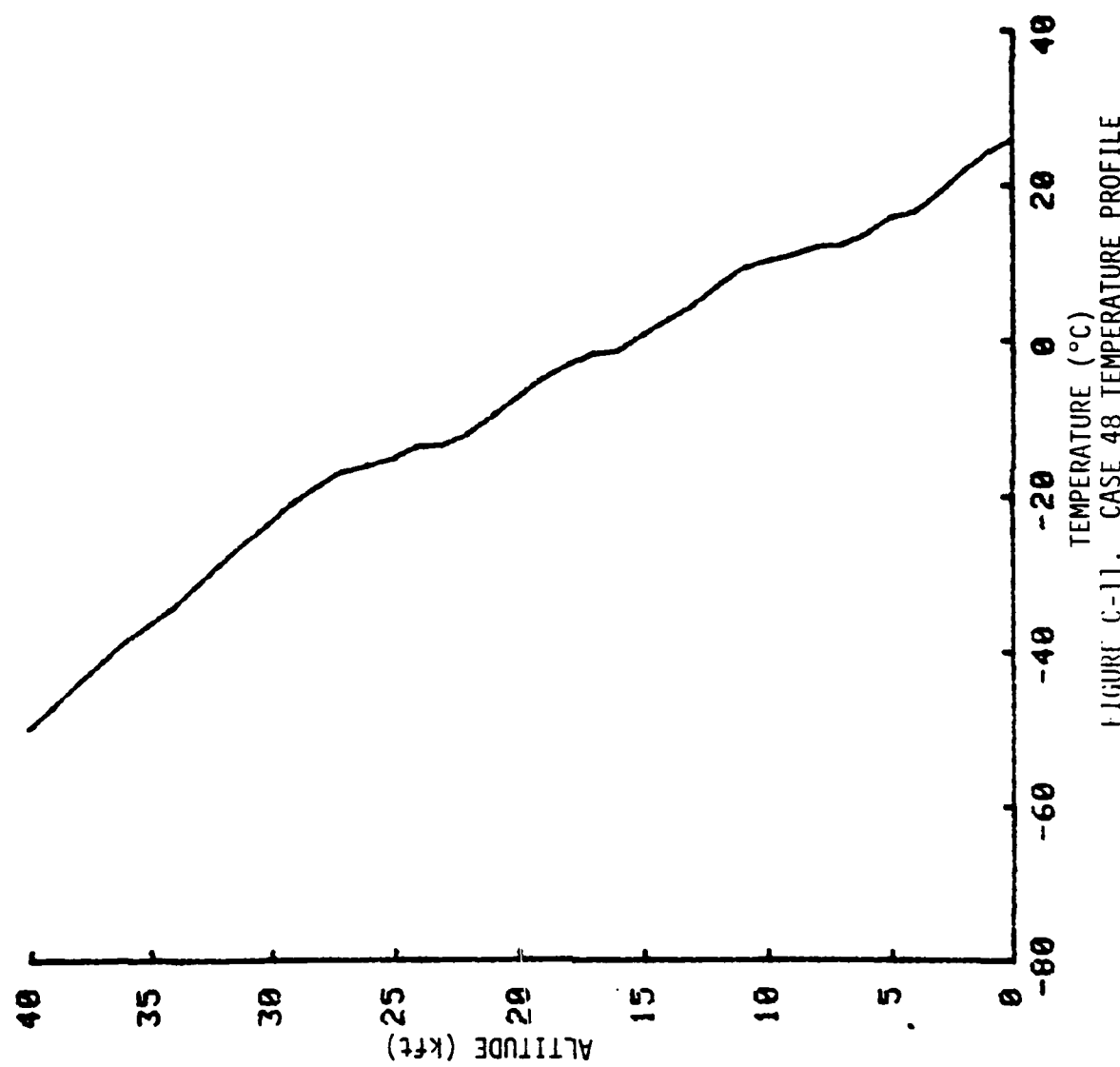


FIGURE C-11. CASE 48 TEMPERATURE PROFILE

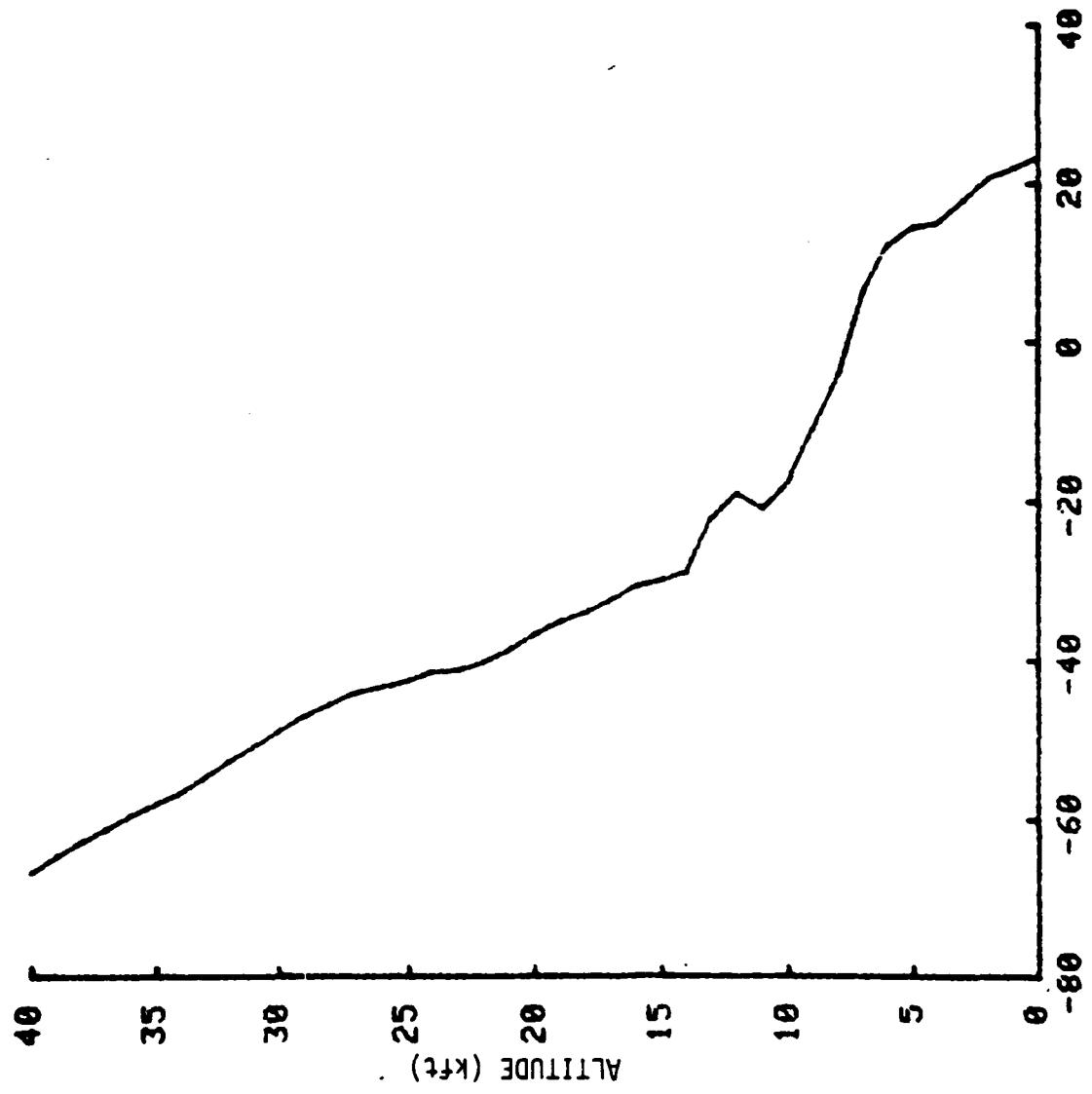
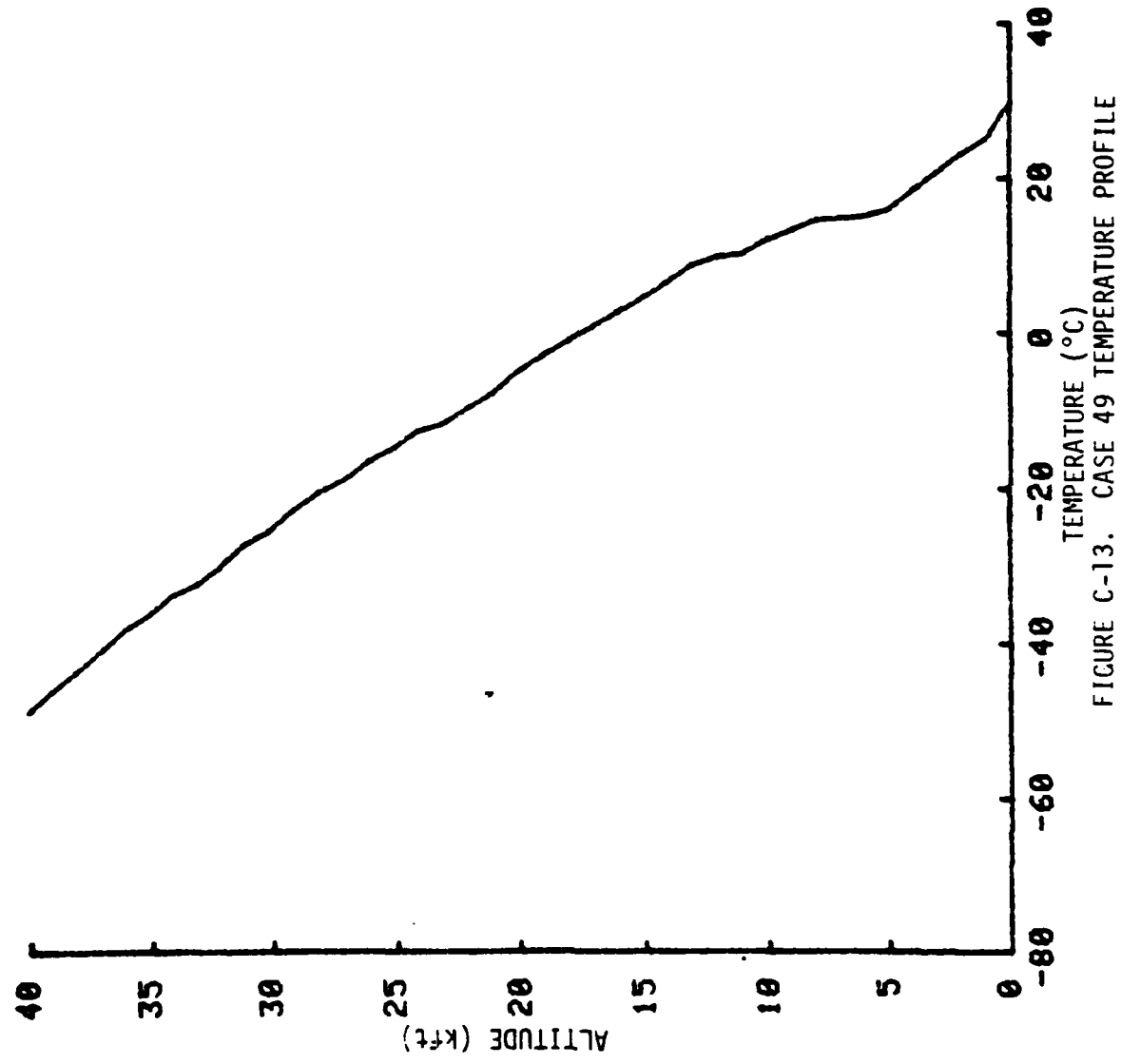


FIGURE C-12. CASE 48 DEW POINT vs ALTITUDE



C-14

FIGURE C-13. CASE 49 TEMPERATURE PROFILE

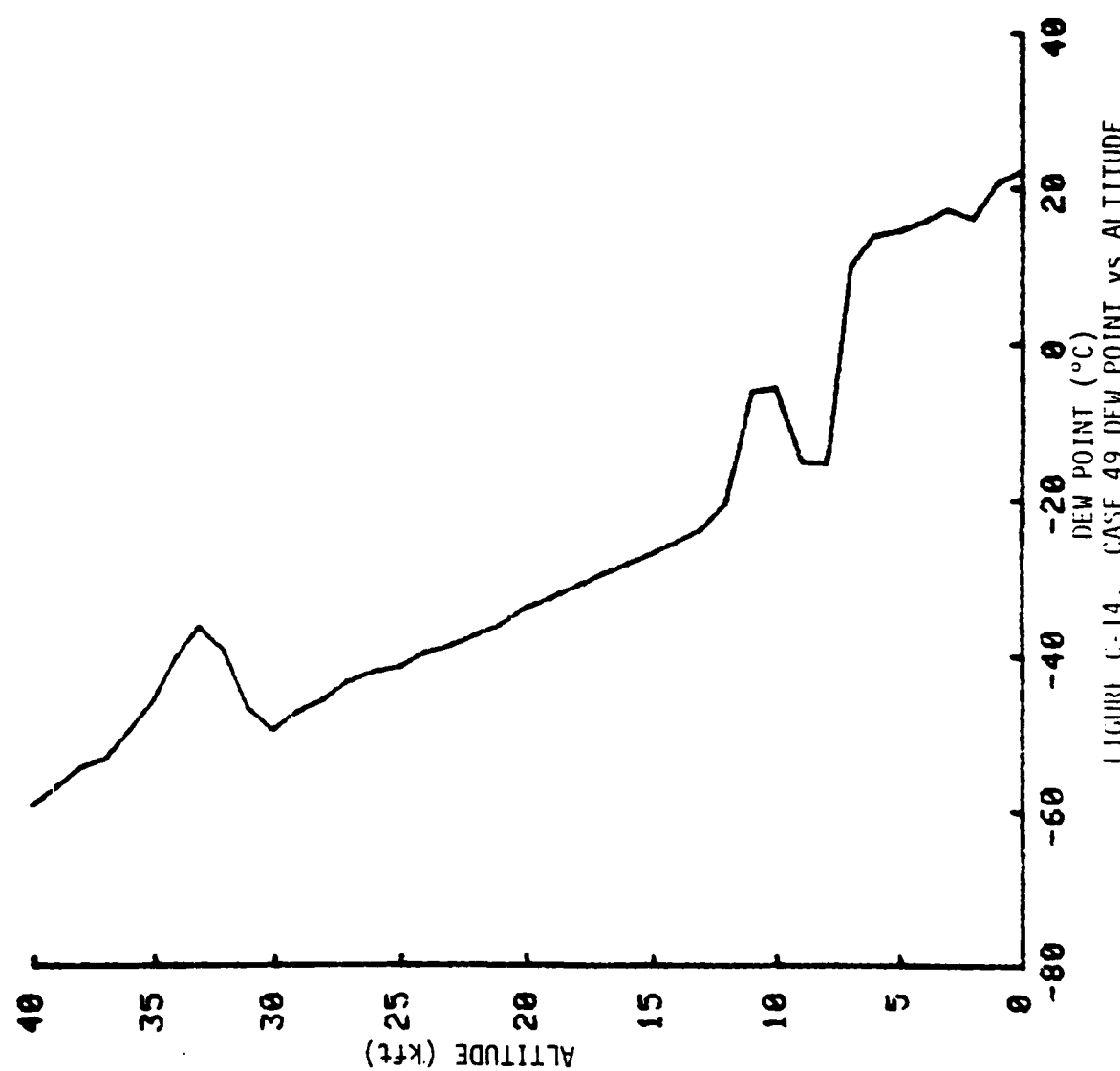


FIGURE C-14. CASE 49 DEW POINT vs ALTITUDE

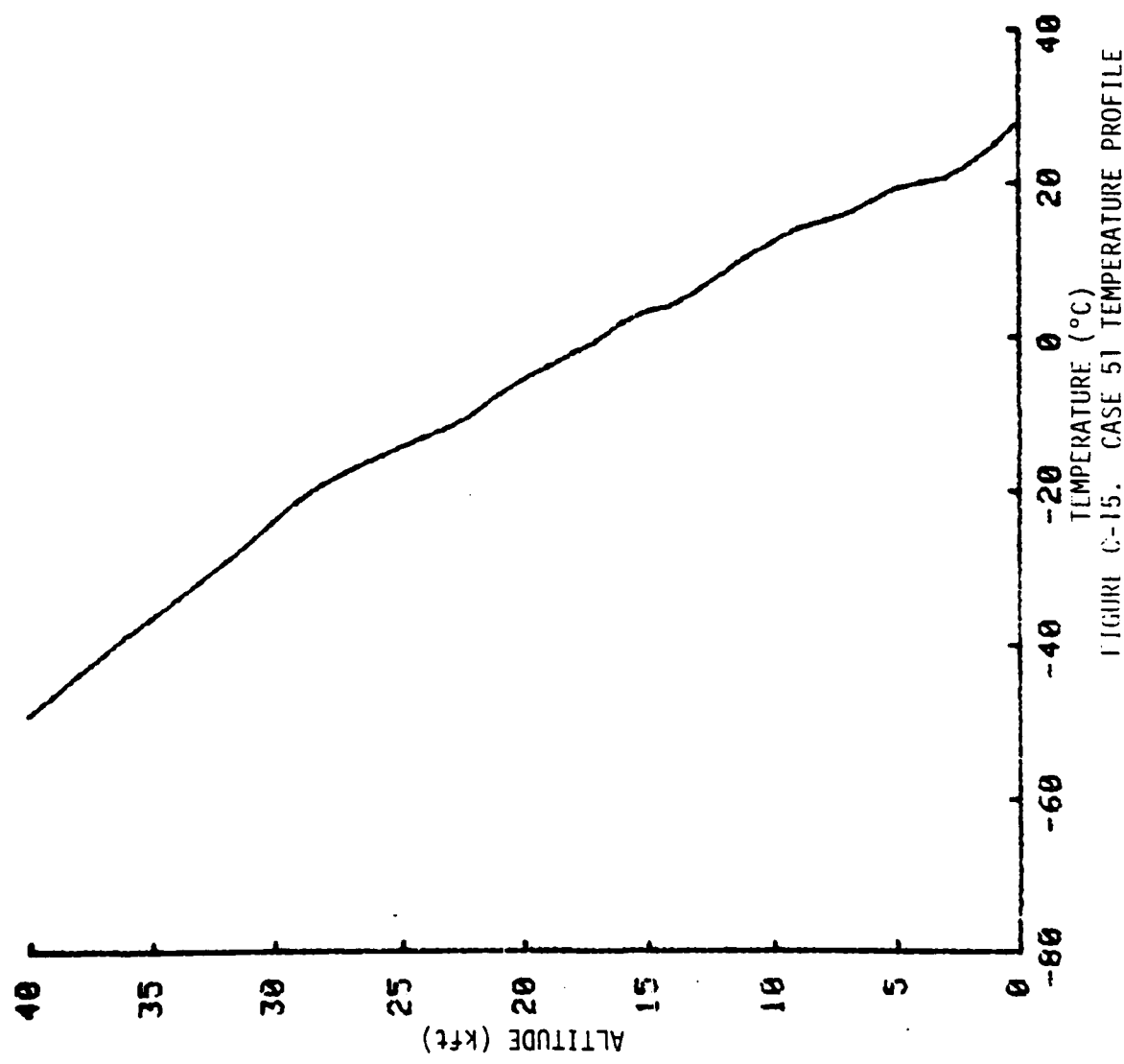


FIGURE C-15. CASE 51 TEMPERATURE PROFILE

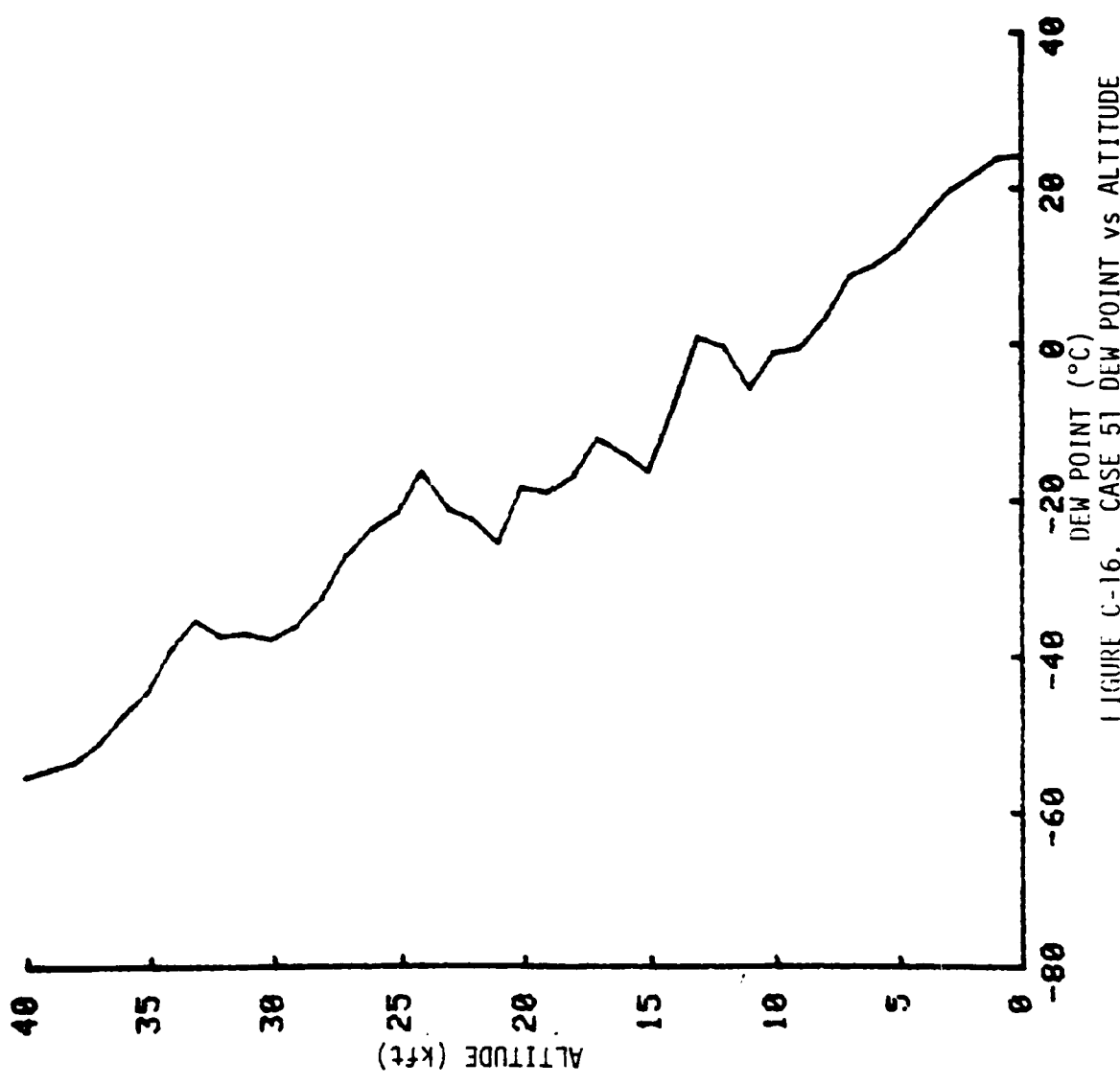


FIGURE C-16. CASE 51 DEW POINT vs ALTITUDE

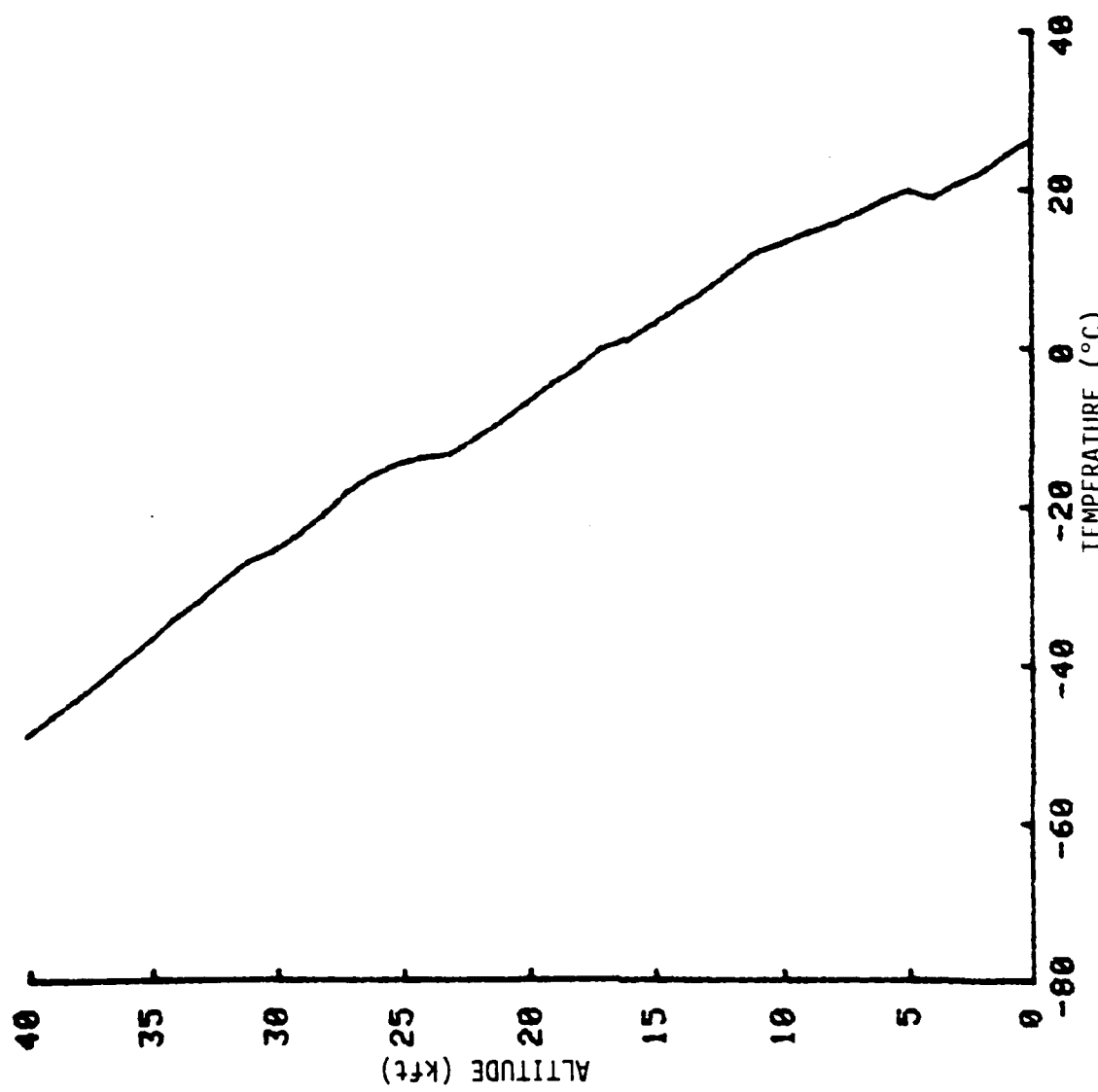


FIGURE C-17. CASE 52 TEMPERATURE PROFILE

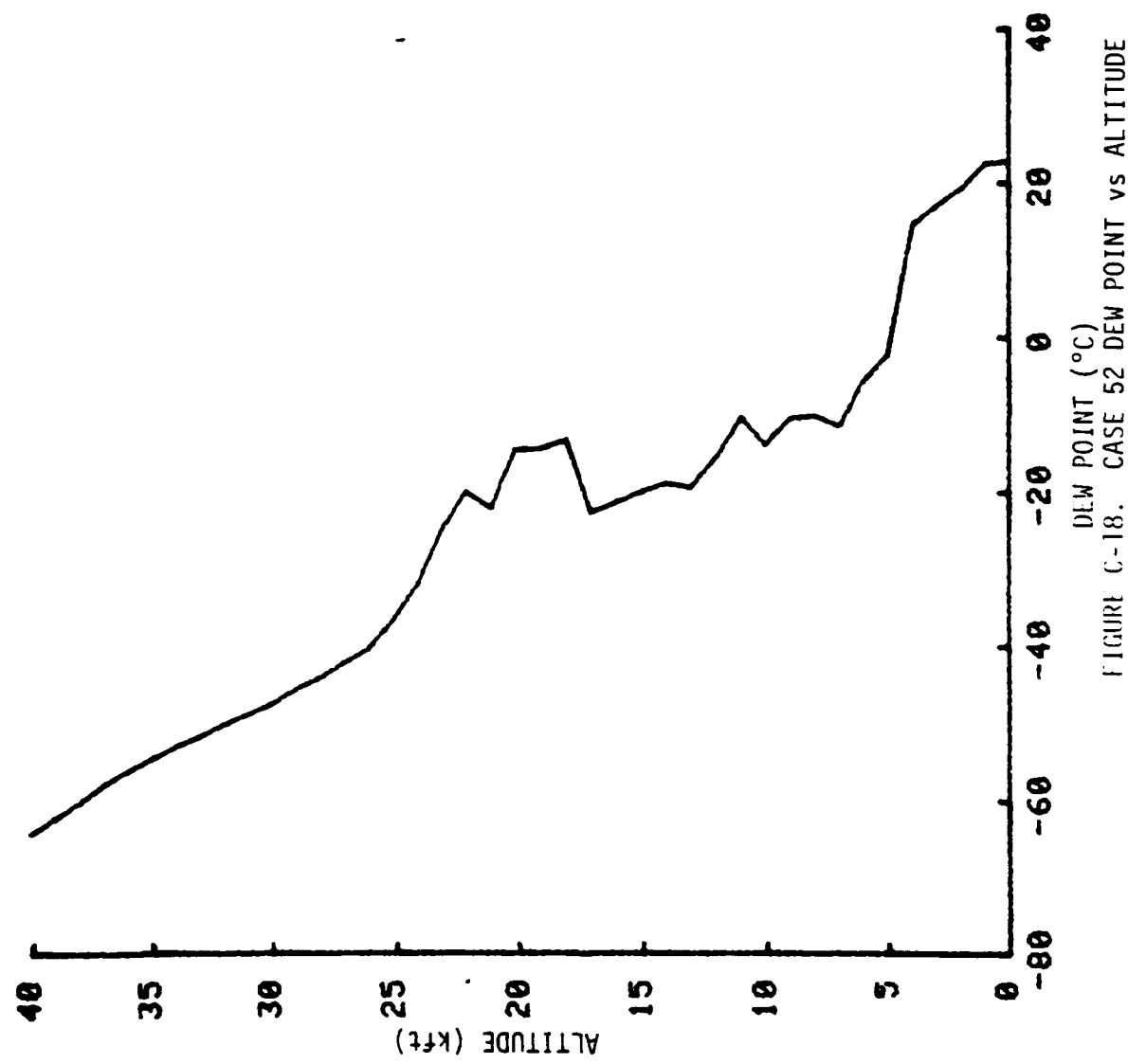


FIGURE C-18. CASE 52 DEW POINT vs ALTITUDE

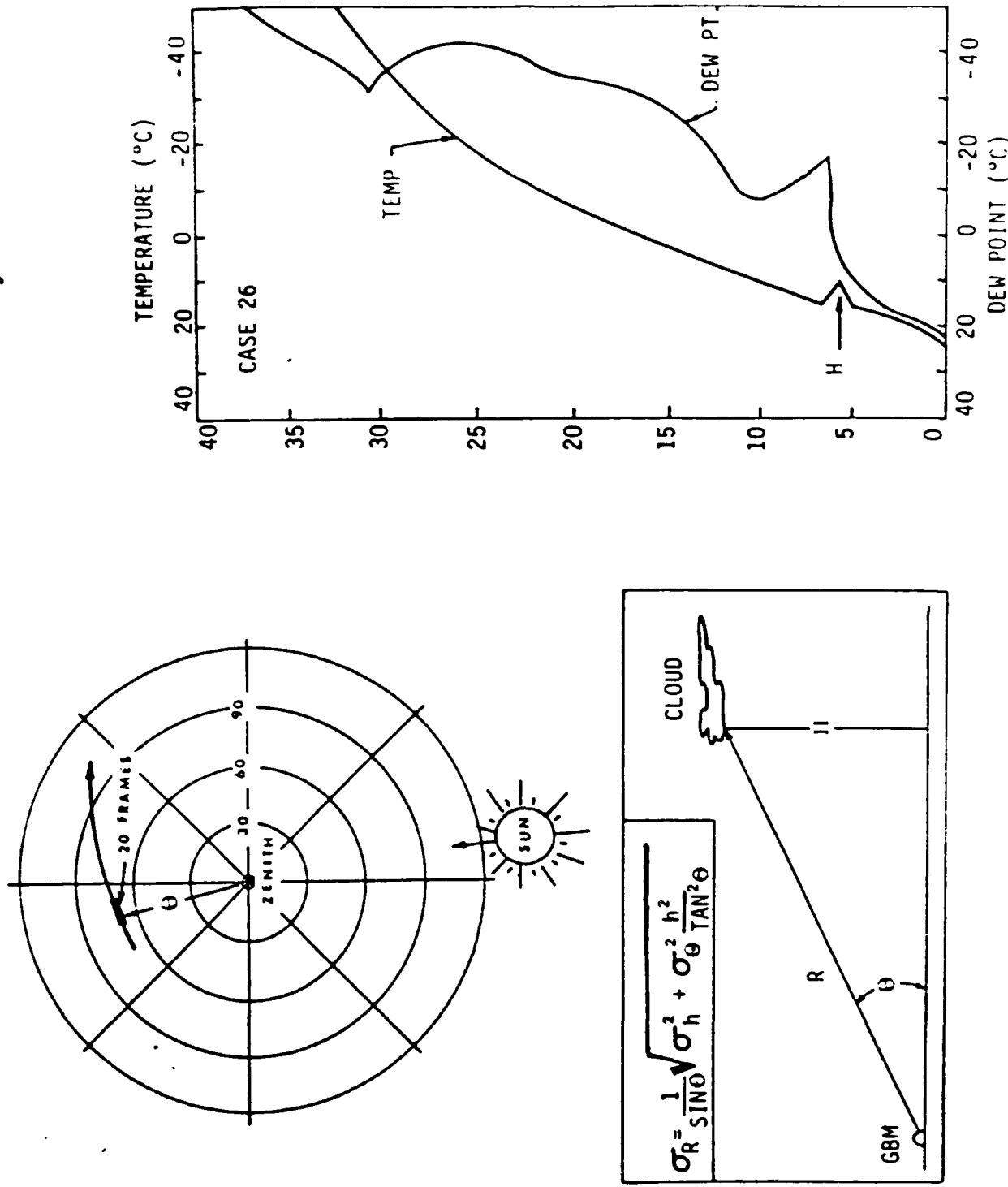


FIGURE C-19. CLOUD RANGE ESTIMATION

## APPENDIX B. CALIBRATION

### B.1 MEASUREMENTS

Following the mission, and prior to securing the GBM Sensor System from its operational cooled status, a postmission radiometric calibration is recorded. This calibration is used as a record of the detector responsivity for the mission, and is performed as closely as practical to the time of, and under the same conditions as, the mission being recorded. This calibration is verified by use of a premission calibration.

The radiometric calibration is performed using the calibration collimator designed especially for this purpose. Basically, the collimator consists of a graybody source controllable over the range from about 300 to 1200 K, a set of apertures that may be placed in front of the graybody, and a system of collimating optics that present to the sensor a virtual source at infinite range. While the GBM tracking pedestal is held at the central azimuth location and the GBM primary telescope is moved in elevation, the graybody image is slowly stepped up or down the focal plane over the elevation field of view.

The calibration coefficients have been derived using these data and various assumptions. Many of the assumptions have been verified to within limits by analysis of more extensive calibrations, such as those that were performed during laboratory tests prior to shipment of the GBM system to Roi Namur for installation.

One assumption used in calibration is that the GBM system is a linear system, since evidence accumulated thus far suggests that the sensor response is nearly linear over its full dynamic range. Another important assumption used in calibration is that the response of the system to a point target can be described by a triplet of voltage values. This is apparent from observations that the voltage values from a point target are frequently detected by more than one detector, while hits on three adjacent detectors are very common.

### B.2 THEORY

Calibration of the sensor is based on the premise that one can, through a combination of measurements, calculate the effective

irradiance present at the sensor. The calibration method applied requires only that the energy distributions in mission and calibration source images be similar. This allows data obtained with both focused and moderately defocused systems to be reduced. The method allows the total irradiance to be determined even when a portion of the energy falls on an inactive detector element.

The basic theory employed in computing the effective irradiance produced by an unresolved source is based on the condition that the source irradiance  $h_b$  during a single calibration run need only remain constant during the recording of any voltage triplet. These voltage triplets thus satisfy an equation of the form

$$\mathcal{K}_b[v_{b(j-1)i}, v_{bj}, v_{b(j+1)i}] = h_b = \text{constant}, \quad (B-1)$$

where

$v_{bj}$  = measured waveform voltage above the local baseline of the  $j$ th detector in spectral band  $b$  of the  $i$ th pulse

$h_b$  = source irradiance at the sensor in spectral band  $b$ .

This function  $\mathcal{K}_b$  has, assuming only linearity of detector response, the property

$$\mathcal{K}[\delta v_{b(j-1)}, \delta v_{bj}, \delta v_{b(j+1)}] = \delta \mathcal{K}_b[v_{b(j-1)}, v_{bj}, v_{b(j+1)}], \quad (B-2)$$

where  $\delta$  is any arbitrary factor. Choosing  $\delta$  equal to the square root of the sum of the squares of the triplet voltage yields

$$\mathcal{K}_b[v_{b(j-1)}, v_{bj}, v_{b(j+1)}] = |v|_{bj} \mathcal{K}_b(a_{bj}, \beta_{bj}, \gamma_{bj}), \quad (B-3)$$

where

$$|v|_{bj} = [v_{b(j-1)}^2 + v_{bj}^2 + v_{b(j+1)}^2]^{\frac{1}{2}}$$

$$a_{bj} = v_{b(j-1)} / |v|_{bj},$$

$$\beta_{bj} = v_{bj} / |v|_{bj},$$

$$\gamma_{bj} = v_{b(j+1)} / |v|_{bj}.$$

This choice of  $\delta$  permits  $\mathcal{K}_b$  to be expressed as the product of two factors, one of which depends only on the direction cosines in the voltage domain. Expressed in this manner  $\mathcal{K}_b$  represents a universal function that is independent of the particular irradiance used in obtaining the calibration data. The unknown irradiance can therefore be obtained by multiplying  $|V|_{bji}$  by  $\mathcal{K}_b$ .

### B.3 NOISE CONSIDERATIONS

Assuming that errors in the measurements caused by random fluctuations (noise) are additive and normally distributed about the mean value, then each member of a measured voltage triplet may be represented in the form  $V = \bar{V} + \Delta V$ , where  $\bar{V}$  is the true (mean) value and  $\Delta V$  is the random error, which is normally distributed having the variance  $\sigma_y^2$ . The variance may be different for each detector element.

This leads to the concept of a "resolution cell" in the voltage domain. The cell is ellipsoidal in shape and is described by the function

$$\frac{[V_{(j-1)} - \bar{V}_{(j-1)}]^2}{\sigma_{(j-1)}^2} + \frac{(V_j - \bar{V}_j)^2}{\sigma_j^2} + \frac{[V_{(j+1)} - \bar{V}_{(j+1)}]^2}{\sigma_{(j+1)}^2} = \text{constant} \quad (B-4)$$

where  $\sigma_j^2 = \sigma_V^2$  for detector J, etc. The value of the constant in Equation B-4 is somewhat arbitrary, but if the 50% point is selected, the value is 2.36606. and there is a 50% probability that the observed triplet  $V_{(j-1)}$ ,  $V_j$ ,  $V_{(j+1)}$  falls within the ellipsoid so defined.

The existence of a resolution cell of finite size in voltage space suggests that, within the allowed finite ranges of voltages, there are only a finite number of distinguishable resolution cells. In particular, if the number of voltage triplets measured during calibration exceeds the number of distinguishable resolution cells in voltage space as determined by random noise, it is justified to combine some of the measured triplets by averaging to reduce the total number.

Therefore, for each pair r, s ( $r < s$ ,  $s = 1$  to n, where n is the total number of voltage triplets for one detector triplet), the value of  $Q_{rs}$  is found by

$$Q_{rs} = \left\{ \frac{[v_{(j-1)r} - v_{(j-1)s}]^2}{\sigma_{(j-1)}^2} + \frac{(v_{jr} - v_{js})^2}{\sigma_j^2} + \frac{[v_{(j+1)r} - v_{(j+1)s}]^2}{\sigma_{(j+1)}^2} \right\} w_x .$$

B-5:

where  $w_x$  is the smaller of  $w_r$  and  $w_s$ . The inclusion of the factor  $w_x$  in the formula for  $Q_{rs}$  reflects the shrinking size of the resolution cell when points are combined and makes it less likely that two points having large and nearly equal weights will be combined. The general effect is to cause "clusters" of points in voltage space to coalesce to a single point each, with the weights of the final set corresponding to the number of points in each original cluster. Let  $Q_{kl}$  denote the smallest  $Q_{rs}$  calculated above. If  $Q_{kl} \leq 2.36606$ , then the points  $k$  and  $l$  are combined by averaging according to the formulas

$$\begin{aligned} \bar{w} &= w_k + w_l , \\ \bar{v}_{(j-1)} &= [w_k v_{(j-1)k} + w_l v_{(j-1)l}] / \bar{w} , \\ \bar{v}_j &= (w_k v_{jk} + w_l v_{jl}) / \bar{w} , \\ \bar{v}_{(j+1)} &= [w_k v_{(j+1)k} + w_l v_{(j+1)l}] / \bar{w} . \end{aligned} \quad (B-6)$$

The two original points  $k$  and  $l$  are then replaced by the single average point, thereby reducing the total number by one. The process is repeated until  $Q_{kl} > 2.36606$ .

When no more points can be combined, the resulting triplet voltages are converted to direction cosines ( $\alpha_{bjk}, \beta_{bjk}, \gamma_{bjk}$ ) which together with the voltages  $v_{bjk}$  constitute the calibration table for the center detector.

#### B.4 CALIBRATION FACTORS

The calibration factors were derived by measuring the  $v_{bjk}$  value of the waveform voltage above the local baseline. These factors were obtained as the constant image of the collimating graybody source slowly moved down each detector in elevation. Different responsivities were measured when the secondary mirror scanned the image across the focal plane right to left and when it scanned left to right (see Figure 2-3

for focal plane detector arrangement). This direction-correlated effect was accounted for in extraction of the intensities.

Normally, mission data are converted to engineering units on the basis of calibration data recorded immediately before and/or after the mission. However, in the case of mission STM-13W, calibration data were recorded only on two detectors of the LWIR array and two detectors of the SWIR array. The reduction process requires a calibration for each detector separately; therefore, the calibration data recorded for mission GT 134M were substituted in the conversion of measured voltages to units of irradiance. This calibration file was selected because it was of good quality and was close in time to STM-13W.

To compensate for the relative responses of the detectors between the calibrations, it was necessary to develop and apply a set of correction factors. These procedures are outlined in Figure B-1. As shown in the figure, the substituted calibration data were processed in the normal manner to generate a calibration file. Voltage peaks for the mission calibrations were read by hand from strip charts and converted to irradiances by means of the substituted calibration file. Since the effective irradiances during the mission calibrations are known, the departure of the "calibration" irradiances from this value represents the error to be corrected using suitable correction factors.

Correction factors  $C_i^{\pm}$  defined by

$$C_i^{\pm} = H_k \langle H_i^{\pm} \rangle$$

B-7

were developed, where  $i = 1, 2, \dots, 31$  identifies the particular LWIR detector and  $\pm$  indicates the direction of scanning. The symbol  $\langle H_i^{\pm} \rangle$  denotes the average value of the "calibration" irradiance for the  $i$ th detector and the  $\pm$  scan direction. Finally, the correction factors are used together with the calibration data file to convert the mission voltages to irradiance values.

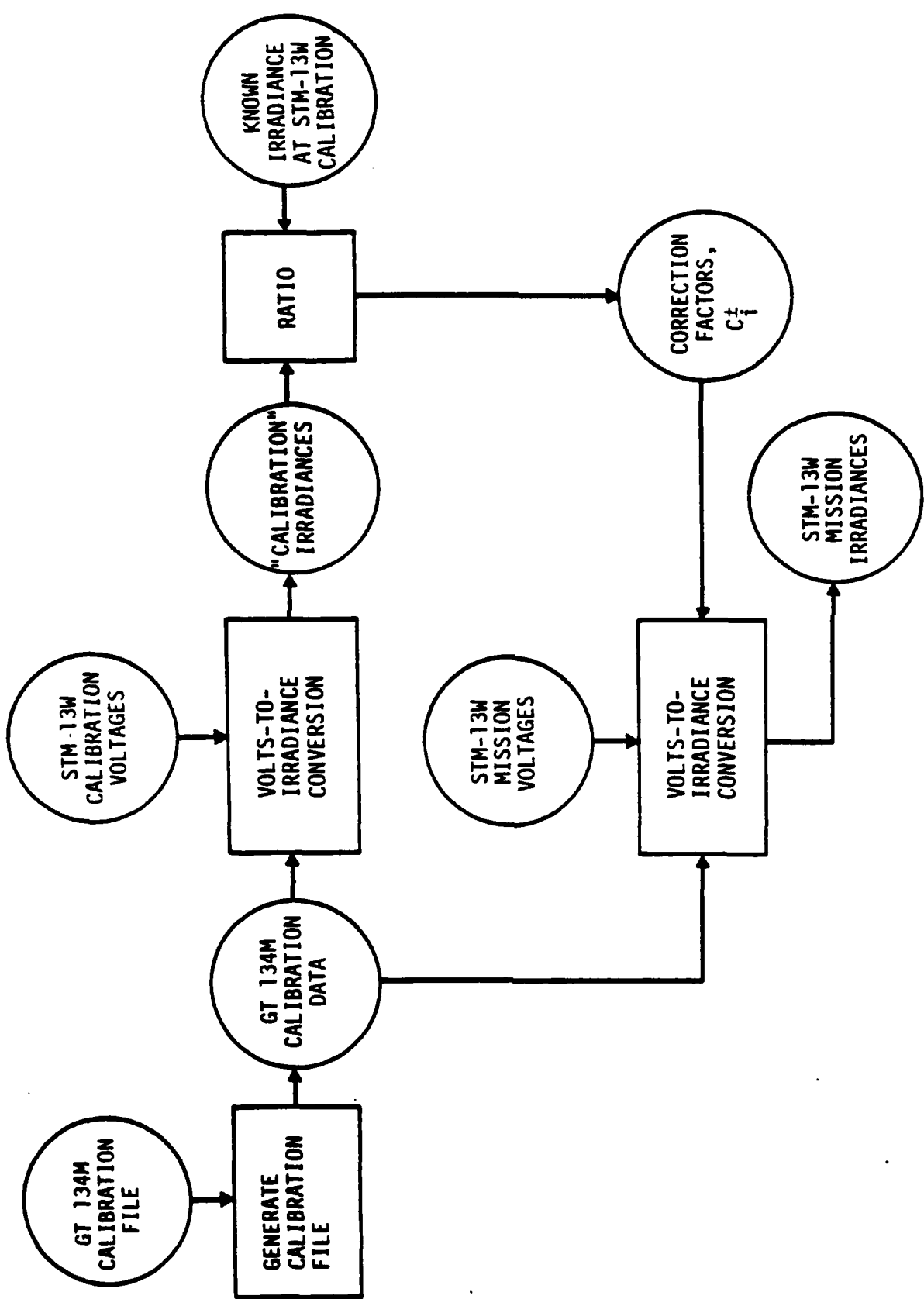


FIGURE B-1. SCHEMATIC DIAGRAM ILLUSTRATING THE METHOD OF DEVELOPING AND APPLYING CORRECTION FACTORS  $C_i^t$  TO COMPENSATE FOR CHANGE IN RELATIVE RESPONSE OF DETECTORS ON MISSION STM-13W

## APPENDIX C. METEOROLOGY

### C.1 RADIOSONDE BALLOON FLIGHTS

For each GBM mission, radiosonde balloon flights were conducted to collect meteorological data supporting the Army Optical Station. These data included: wind direction, wind speed, temperature, dew point, pressure, density, absolute and relative humidity, index of refraction, visibility, and wind shear as a function of altitude between 12 and 100,000 ft.

Those data of most interest in the analysis of clouds are the temperature and dew point profiles. These are plotted for the cases of interest between 0 and 40,000-ft altitude in Figures C-1 through C-18.

### C.2 CLOUD RANGE ESTIMATES

A rough estimate of the range to an observed cloud can be determined using the boresight tracking data of Appendix C and the Temperature and Dew Point Profiles. These estimates are determined assuming that the temperature and/or dew point inversions as illustrated in Figure C-19 indicate the average altitude for cloud formations. Then, using the boresight elevation of the cloud measurement and simple trigonometry, a rough estimate of the cloud range is made. The range error associated with such an estimate is given by,

$$\sigma_R = \frac{1}{\sin\theta} \sqrt{\sigma_h^2 + \sigma_\theta^2 \frac{h^2}{\tan^2\theta}} , \quad (C-1)$$

where the elevation angle error  $\sigma_\theta$  is insignificant compared to the altitude error  $\sigma_h$ ; hence Equation C-1 reduces to

$$\sigma_R \approx \frac{\sigma_h}{\sin\theta} , \quad (C-2)$$

where

$\sigma_h$  = altitude error (1 sigma)

$\theta$  = measured elevation angle of cloud.

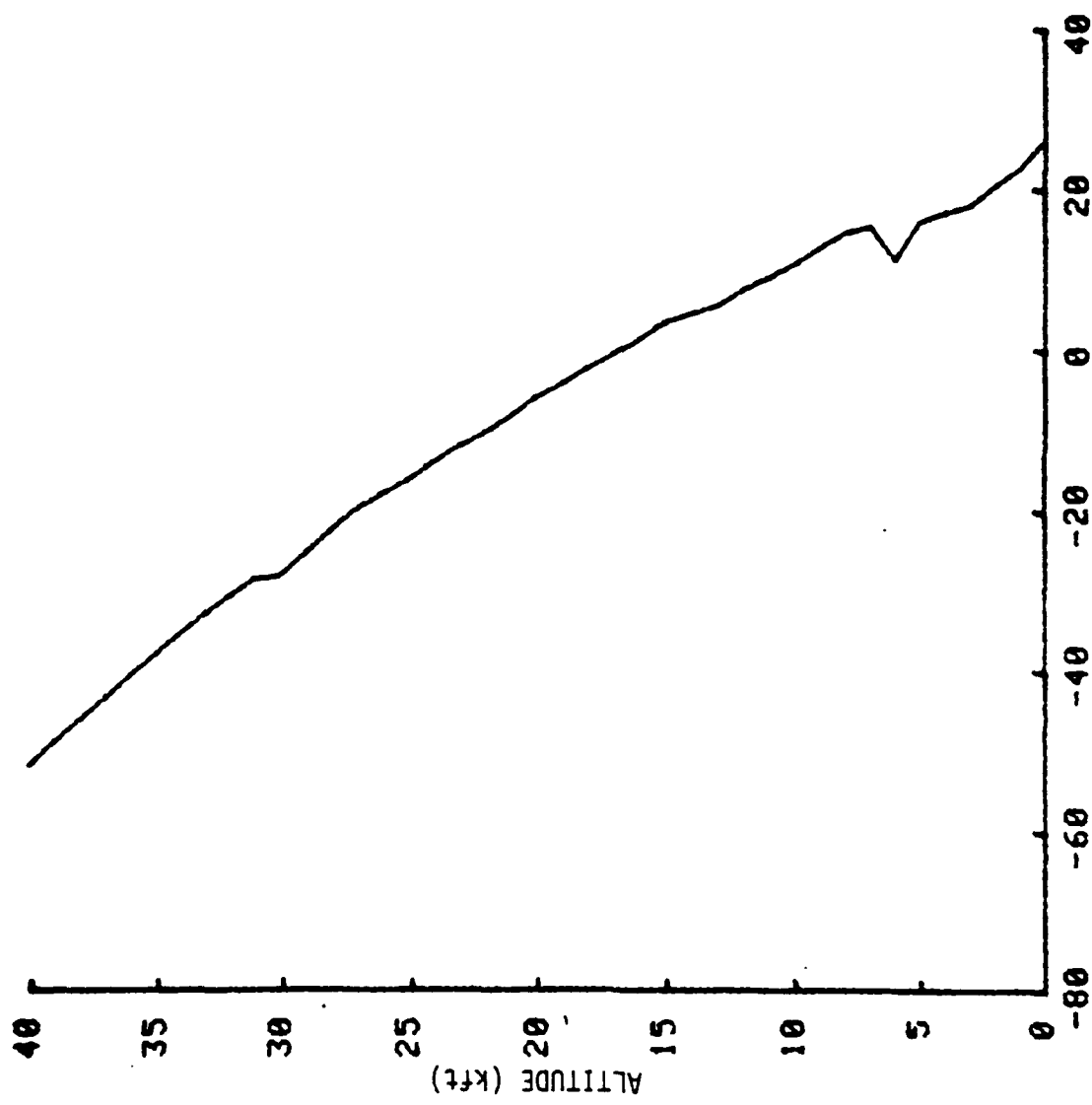
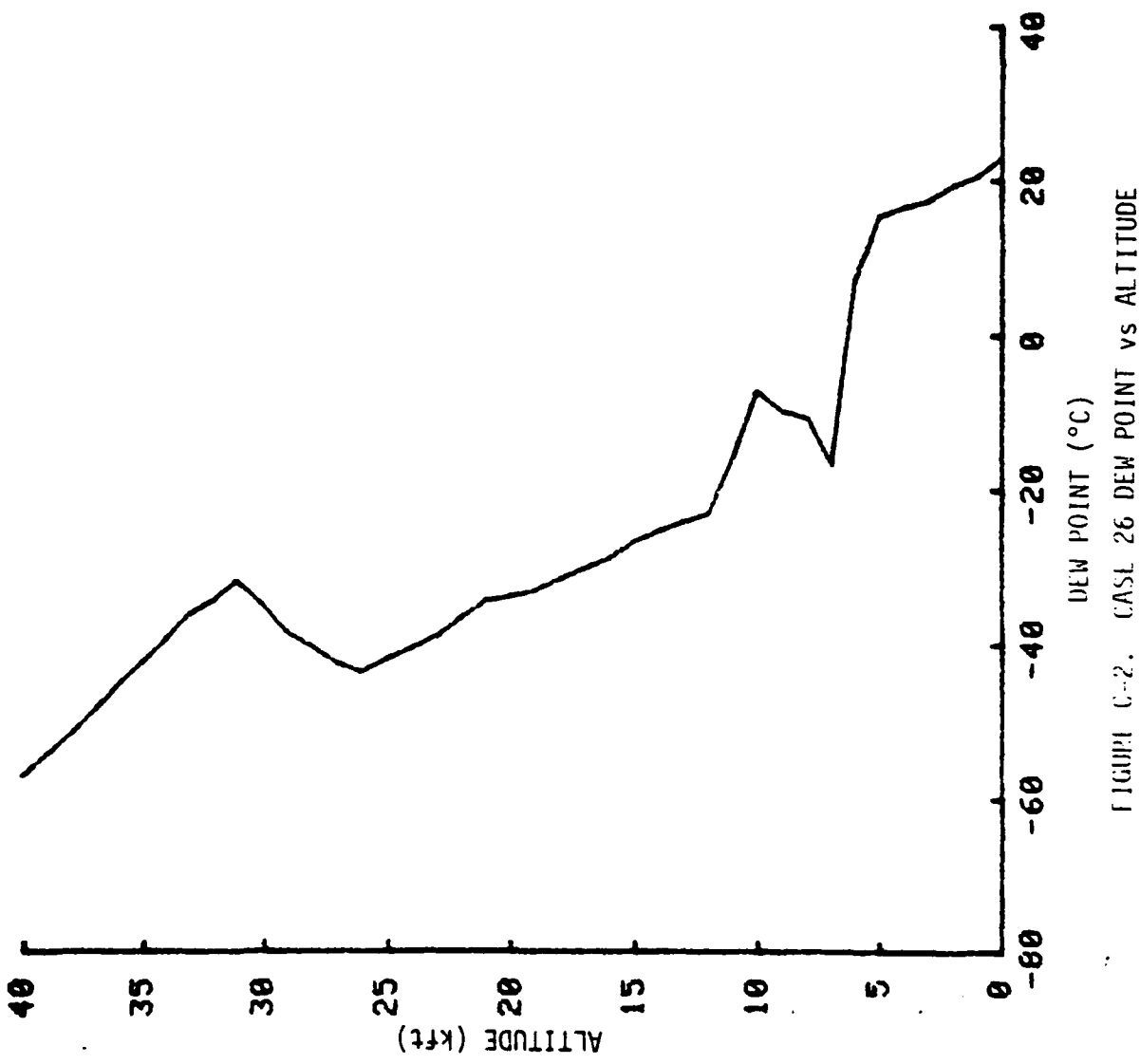


FIGURE C-1. CASE 26 TEMPERATURE PROFILE



FLIGHT C-2. CASE 26 DEW POINT vs ALTITUDE

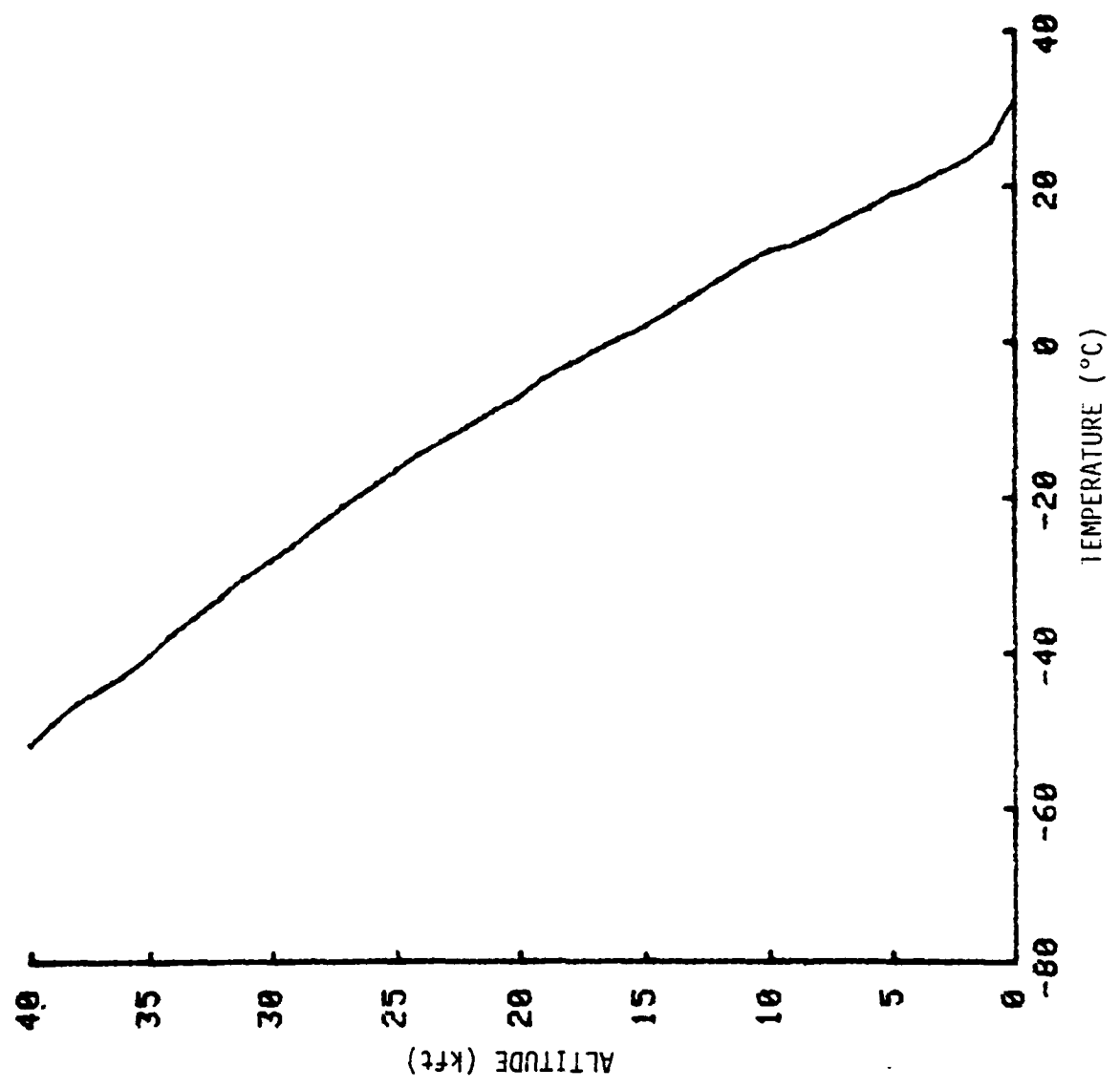


FIGURE 1-3. CASE 30 TEMPERATURE PROFILE

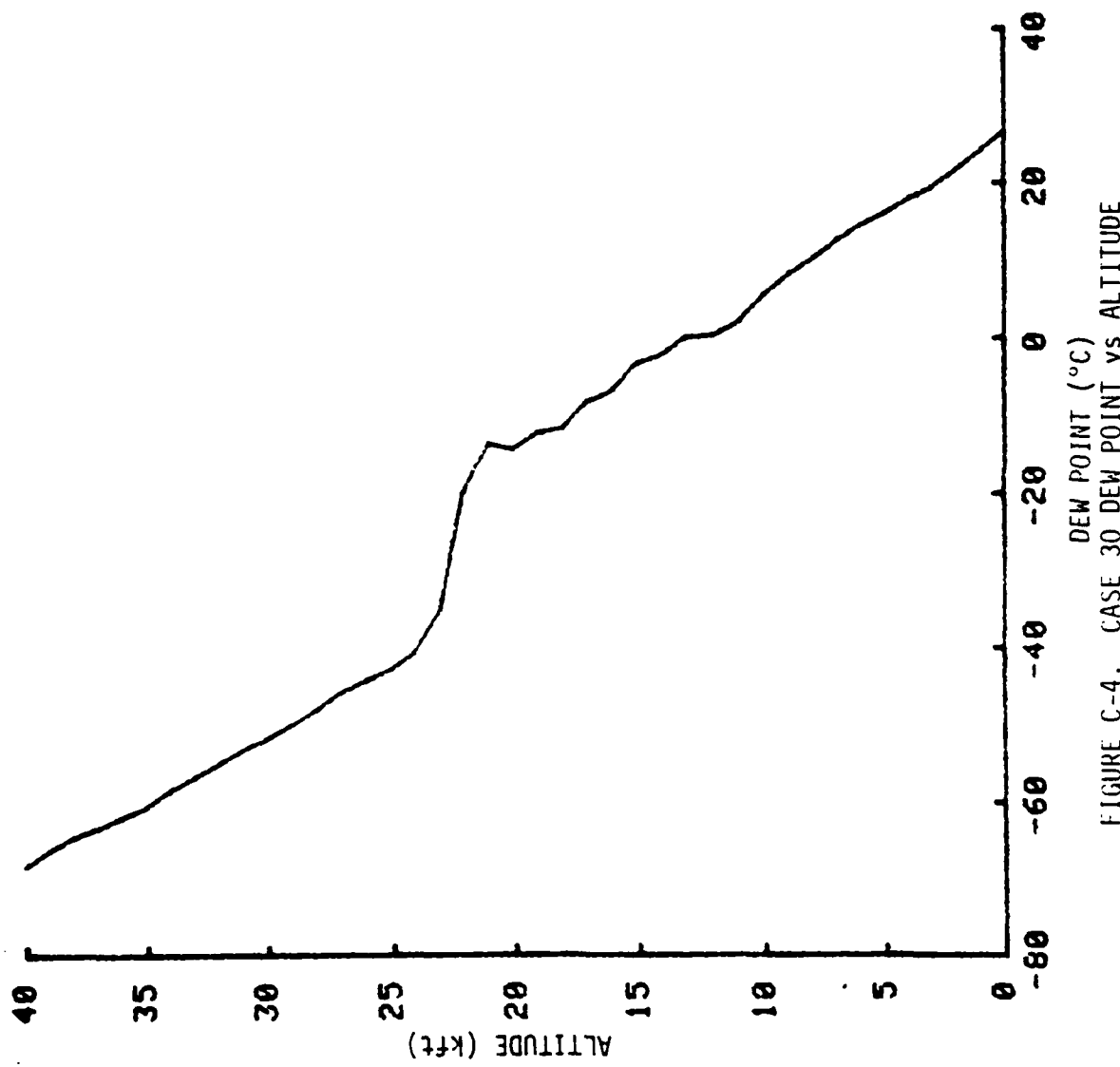


FIGURE C-4. CASE 30 DEW POINT vs ALTITUDE

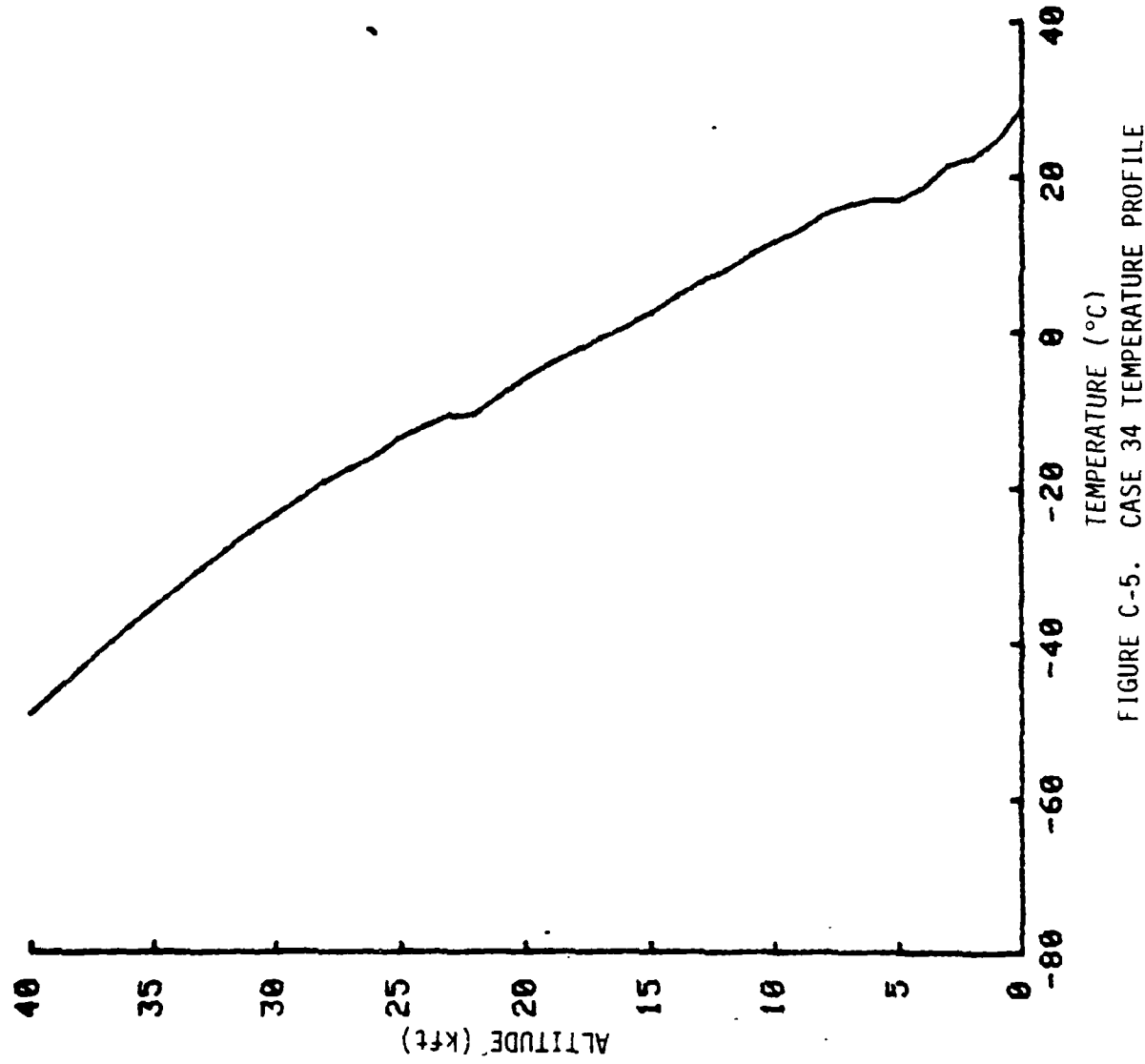


FIGURE C-5.  
CASE 34 TEMPERATURE PROFILE

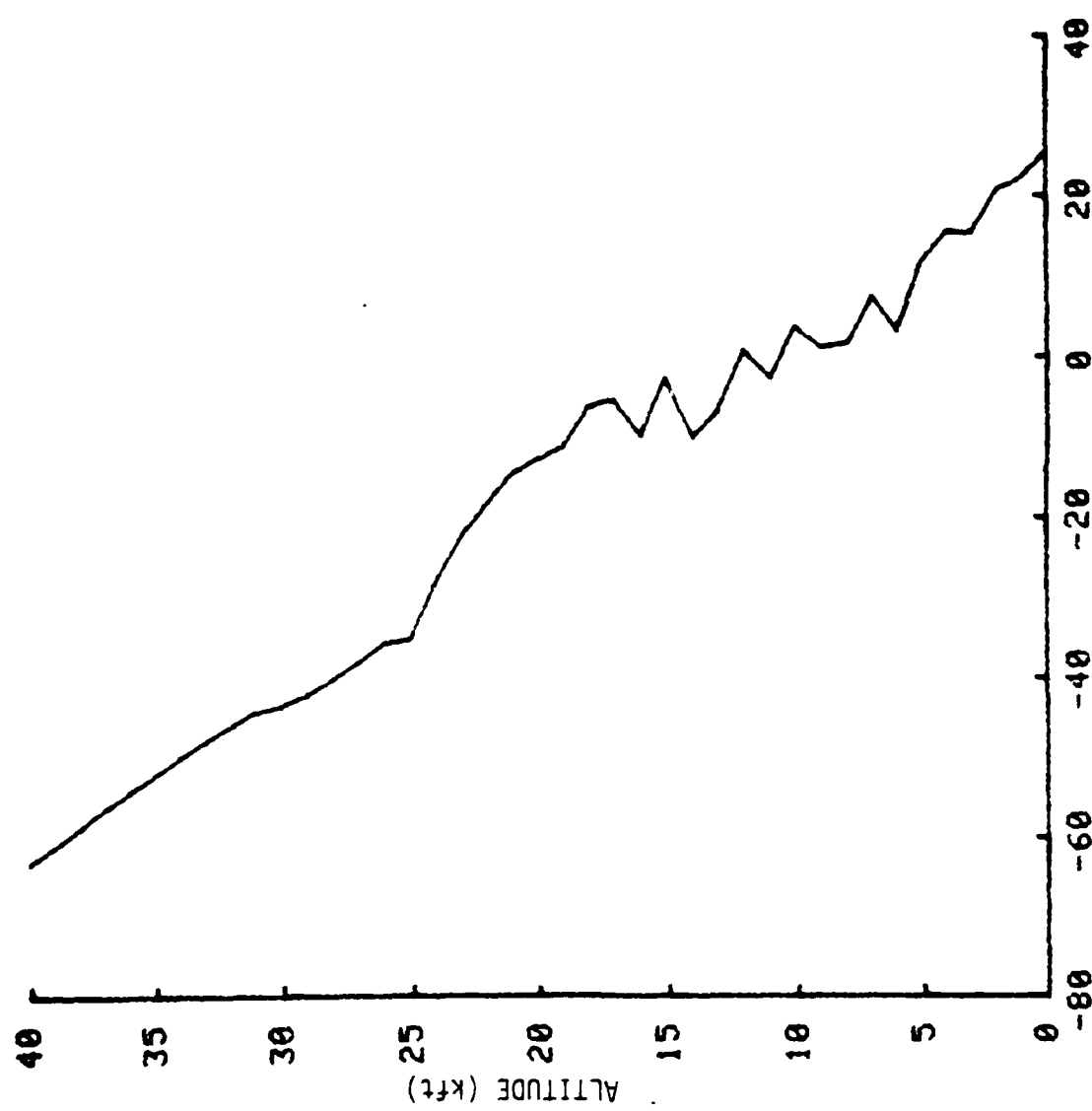


FIGURE C-6. CAST 34 DEW POINT vs ALTITUDE

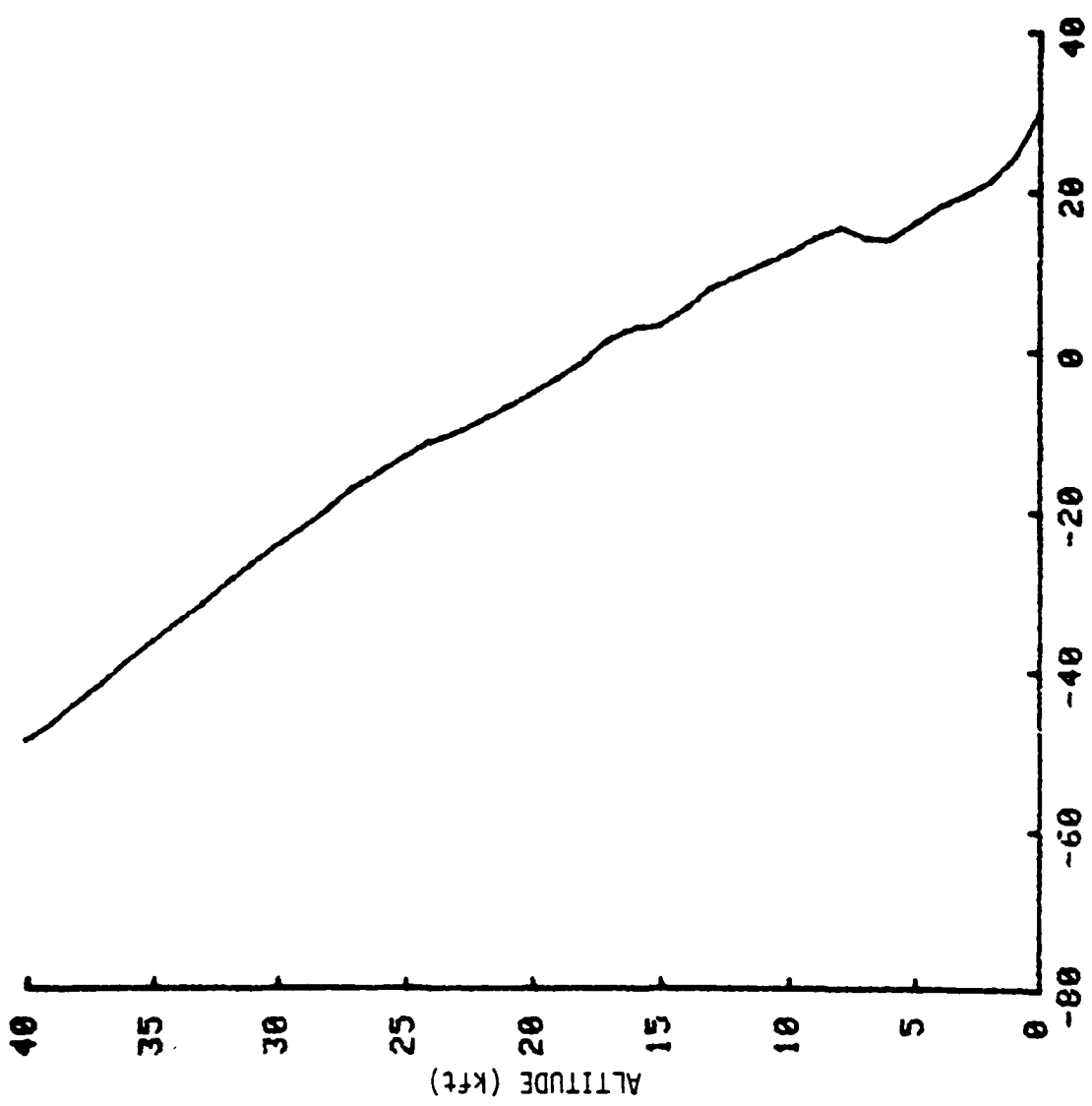


FIGURE C-7. CASE 42 TEMPERATURE PROFILE

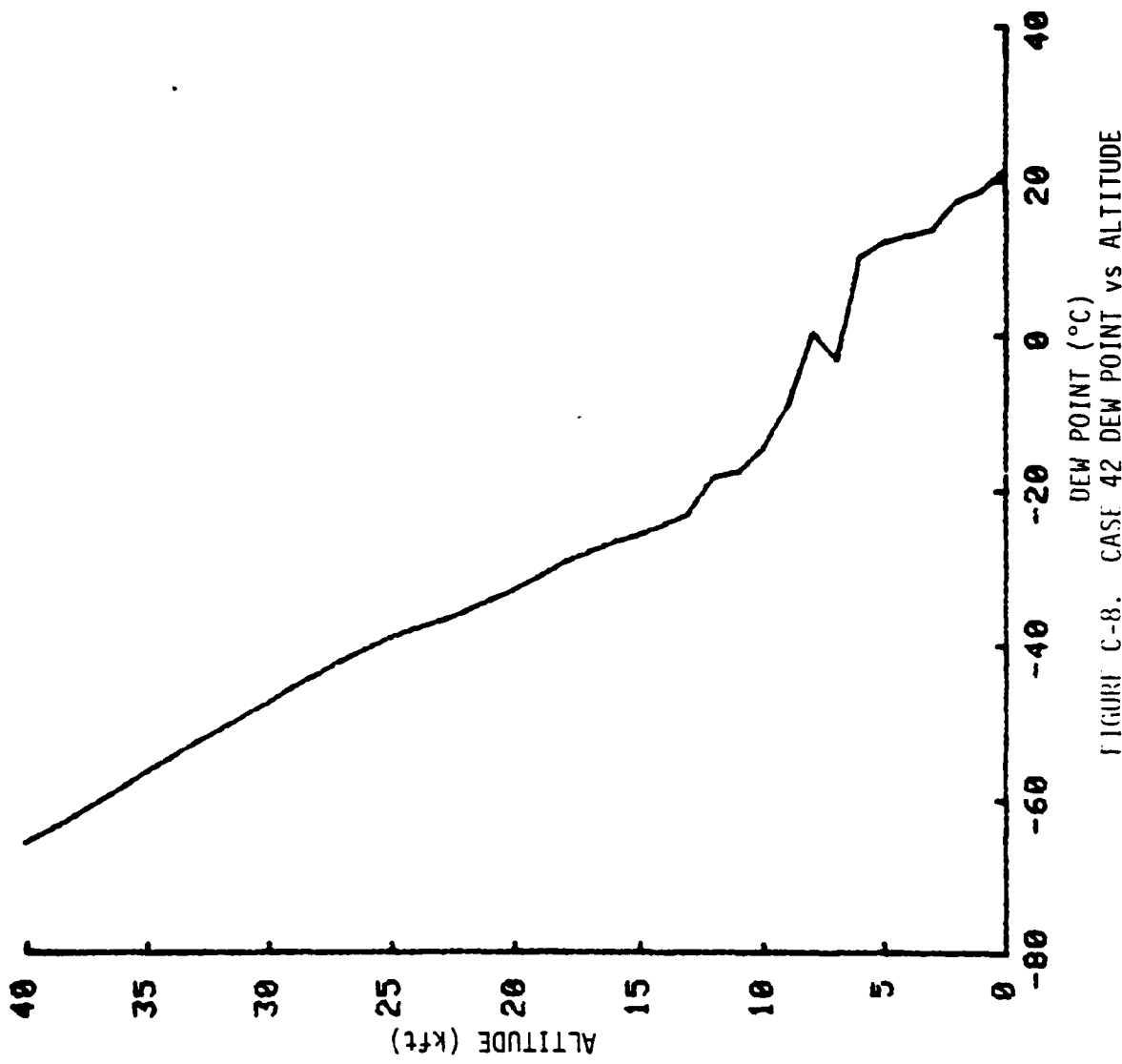


FIGURE C-8. CASE 42 DEW POINT vs ALTITUDE

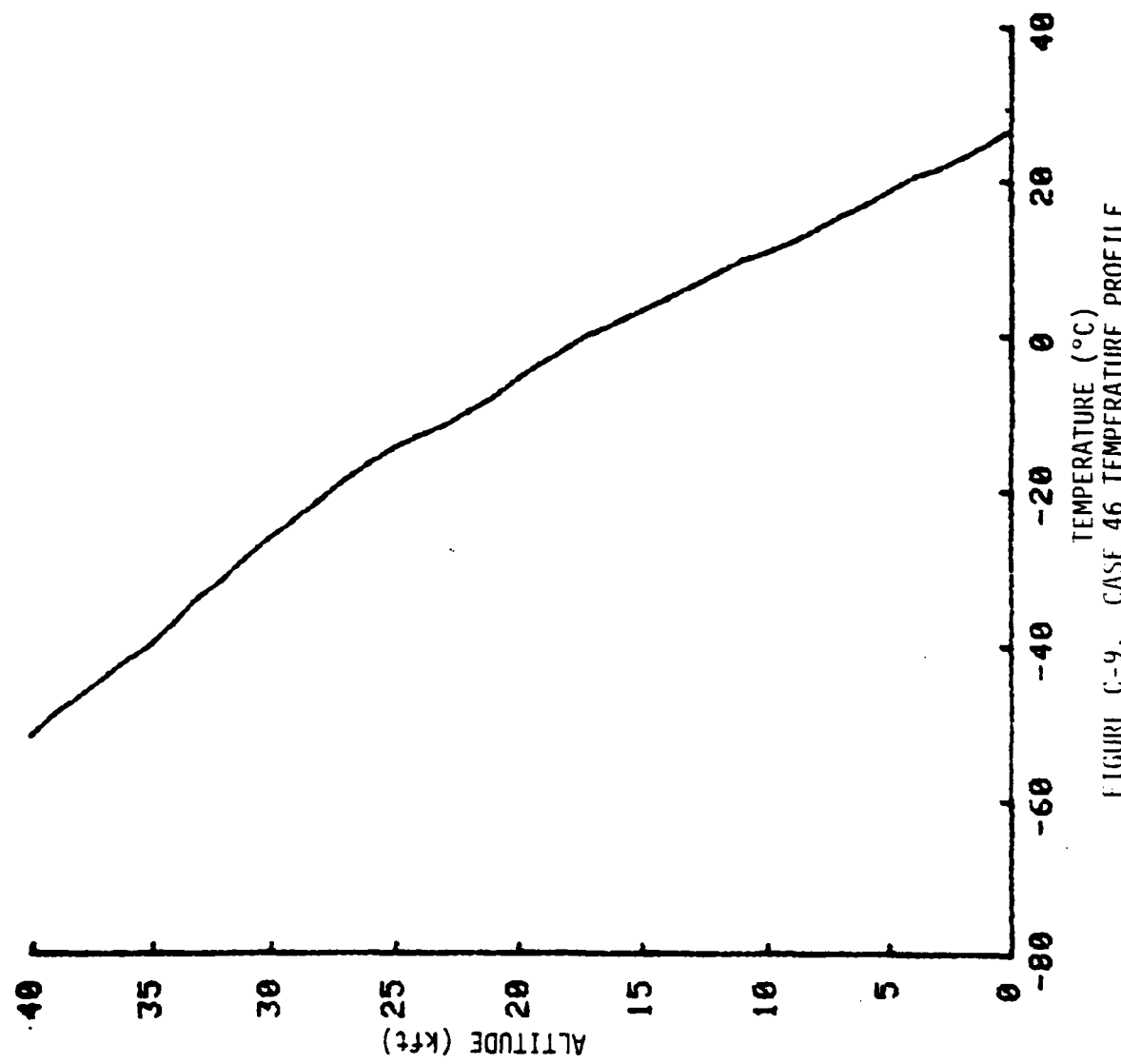


FIGURE C-9. CASE 46 TEMPERATURE PROFILE

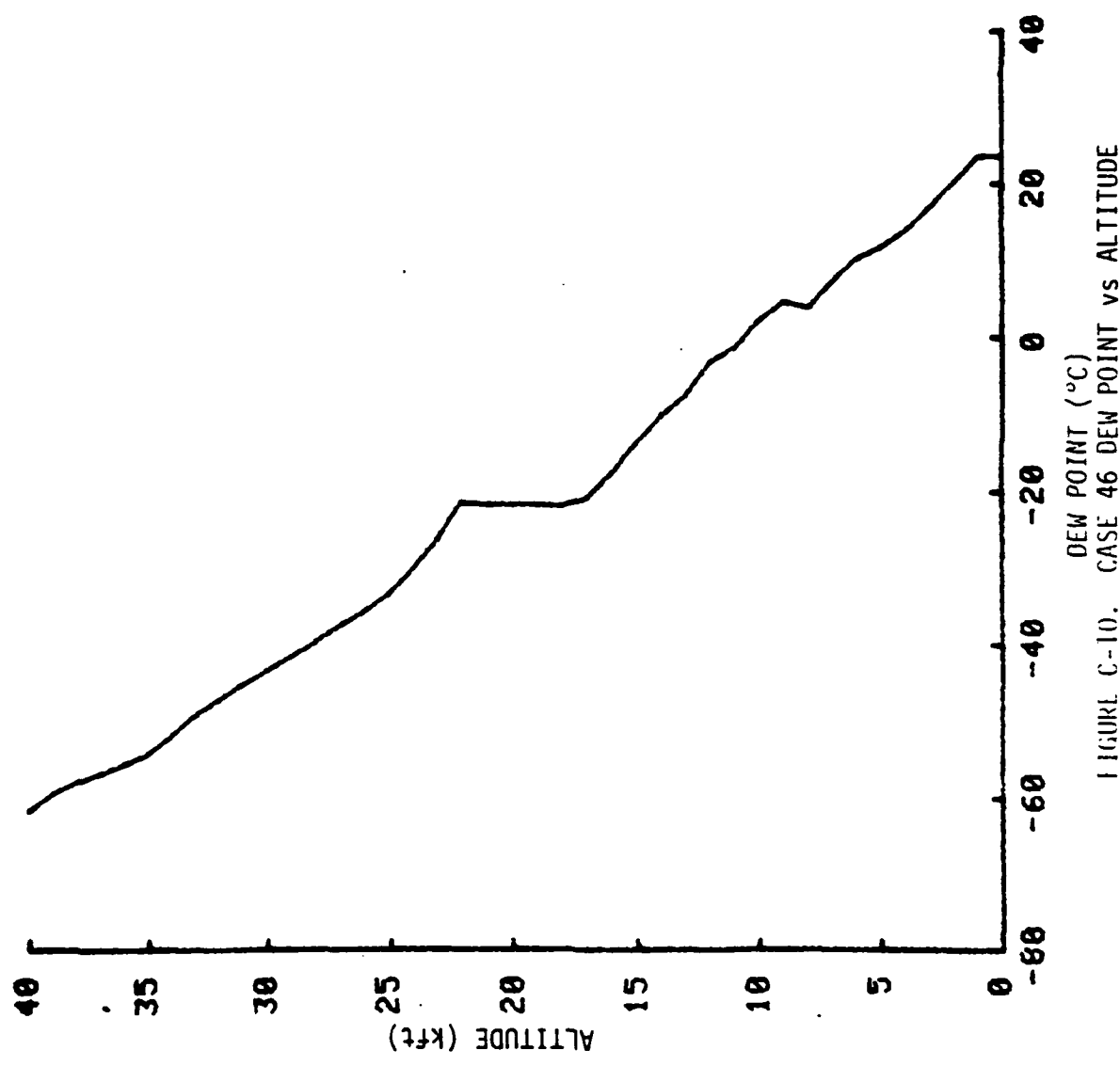


FIGURE C-10. CASE 46 DEW POINT vs ALTITUDE

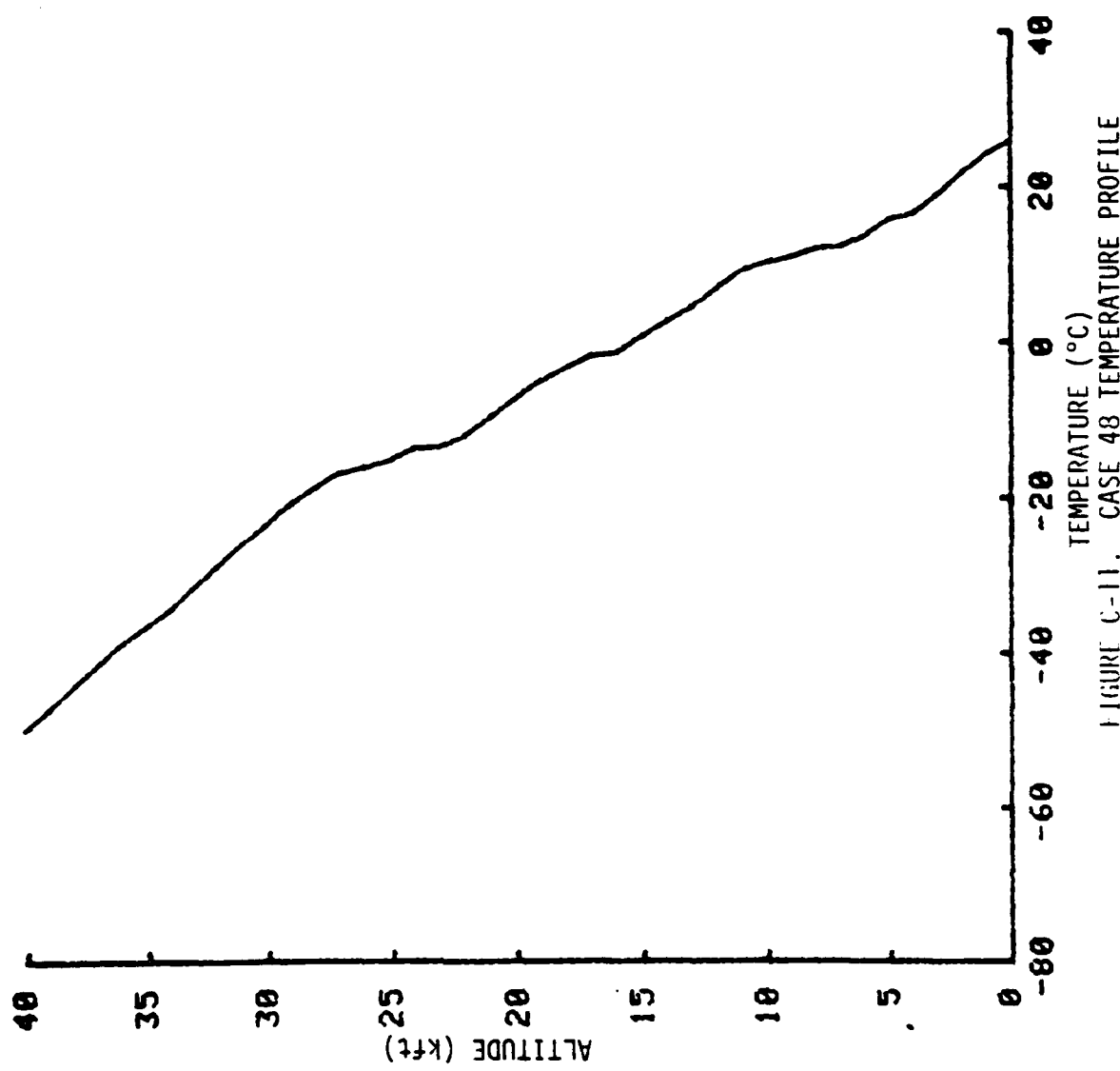


FIGURE C-11. CASE 48 TEMPERATURE PROFILE

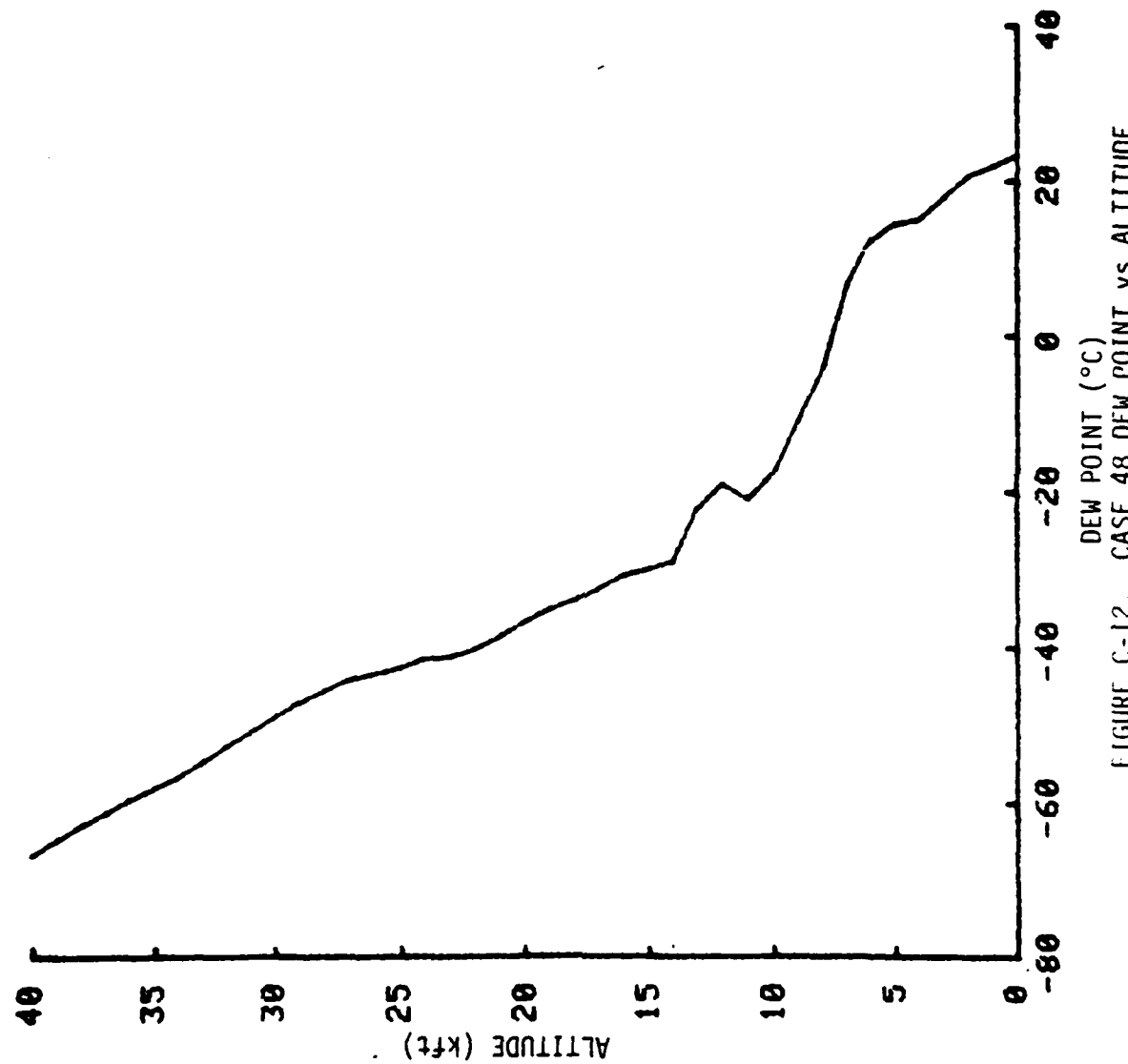


FIGURE C-12. CASE 48 DEW POINT vs ALTITUDE

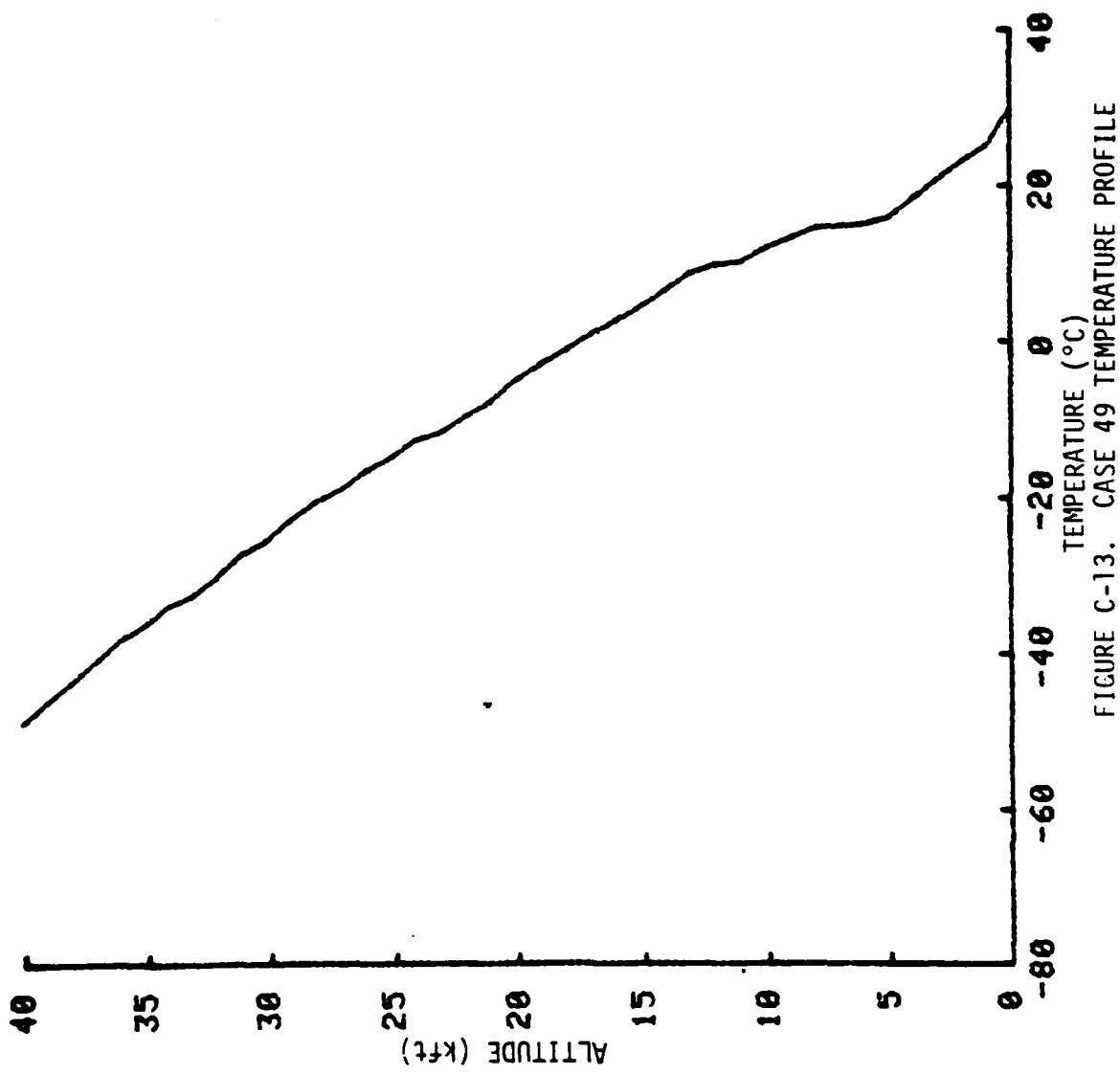


FIGURE C-13. CASE 49 TEMPERATURE PROFILE

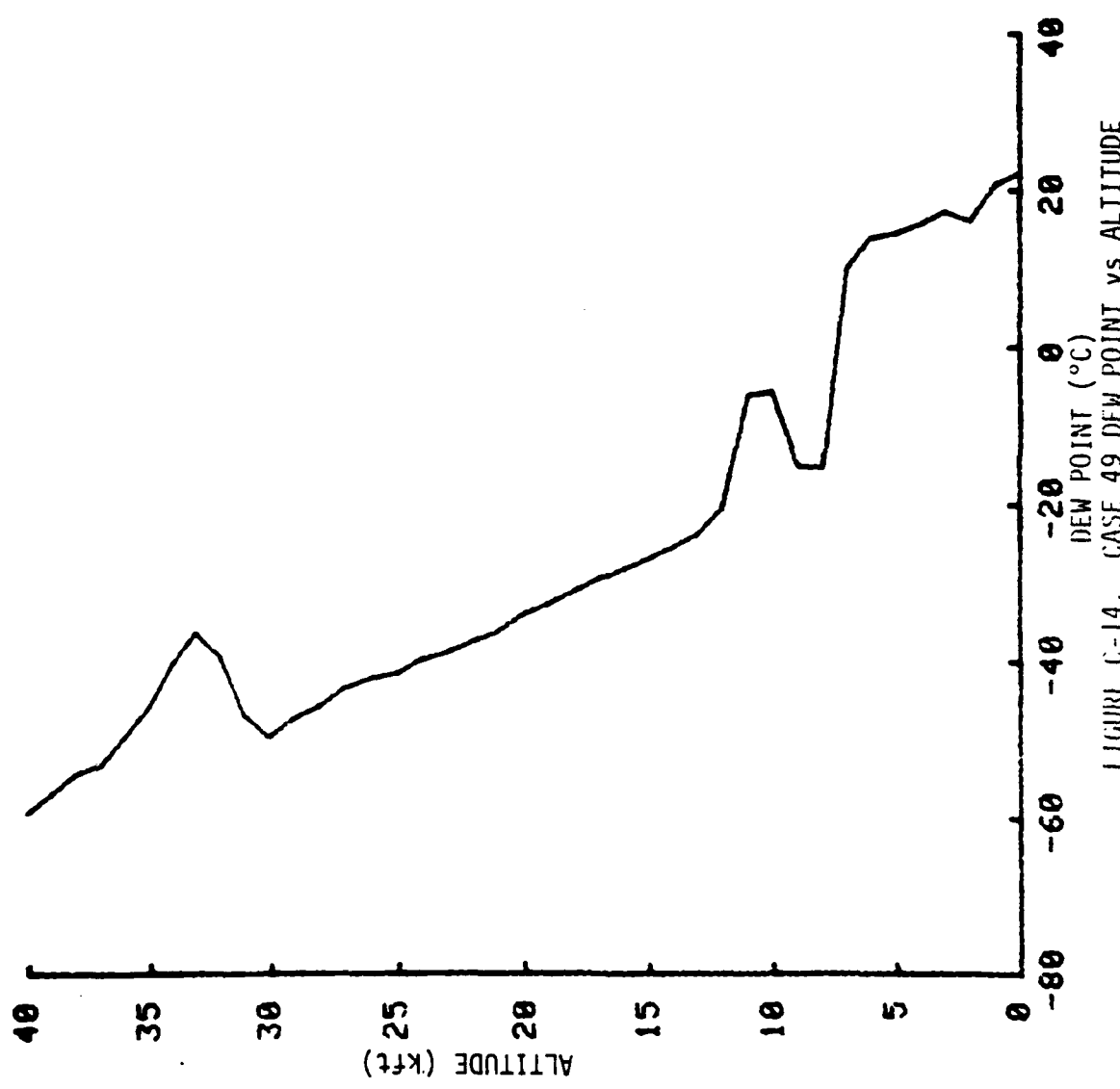


FIGURE C-14. CASE 49 DEW POINT vs ALTITUDE

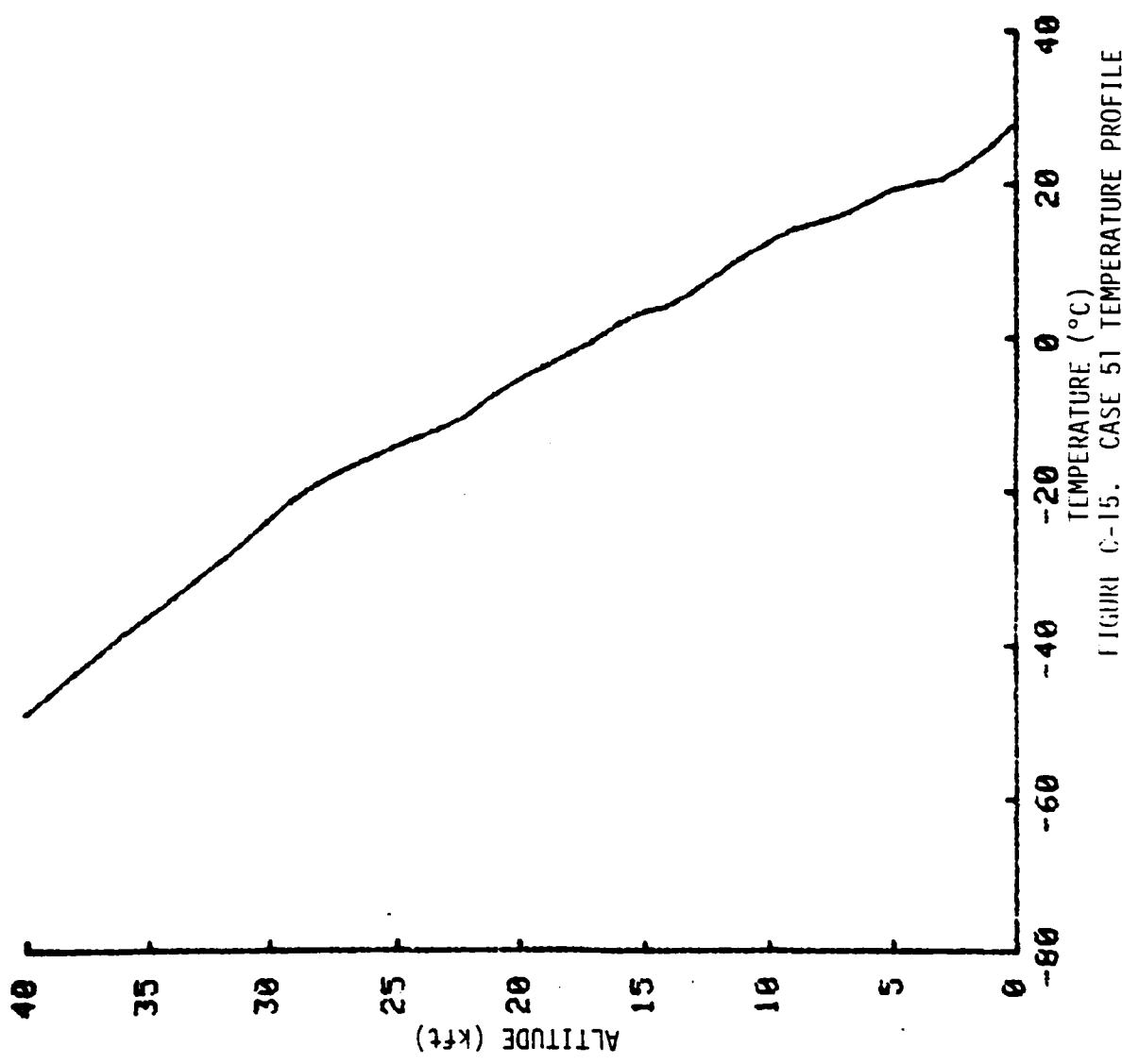


FIGURE C-15. CASE 51 TEMPERATURE PROFILE

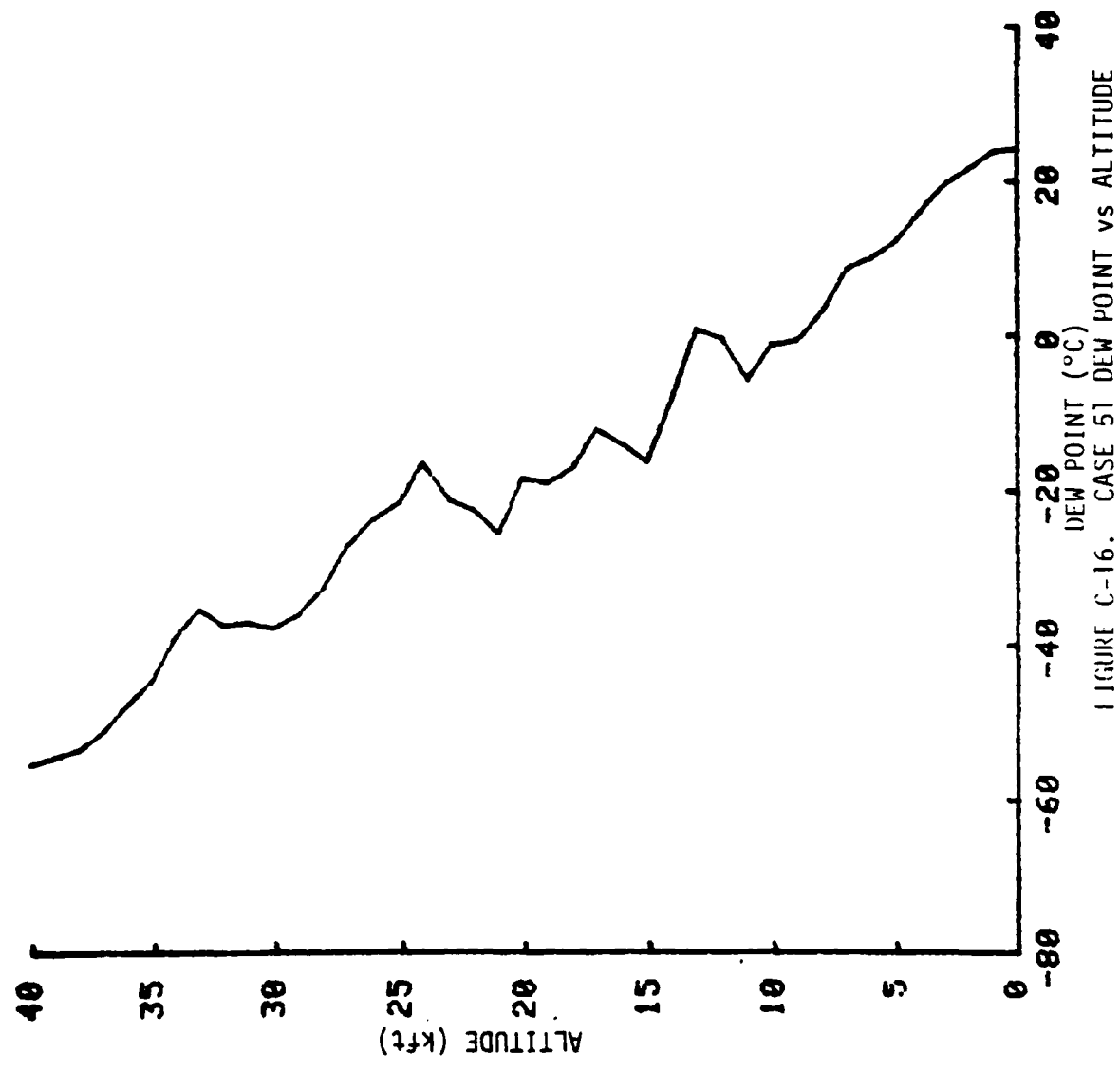


FIGURE C-16. CASE 51 DEW POINT vs ALTITUDE

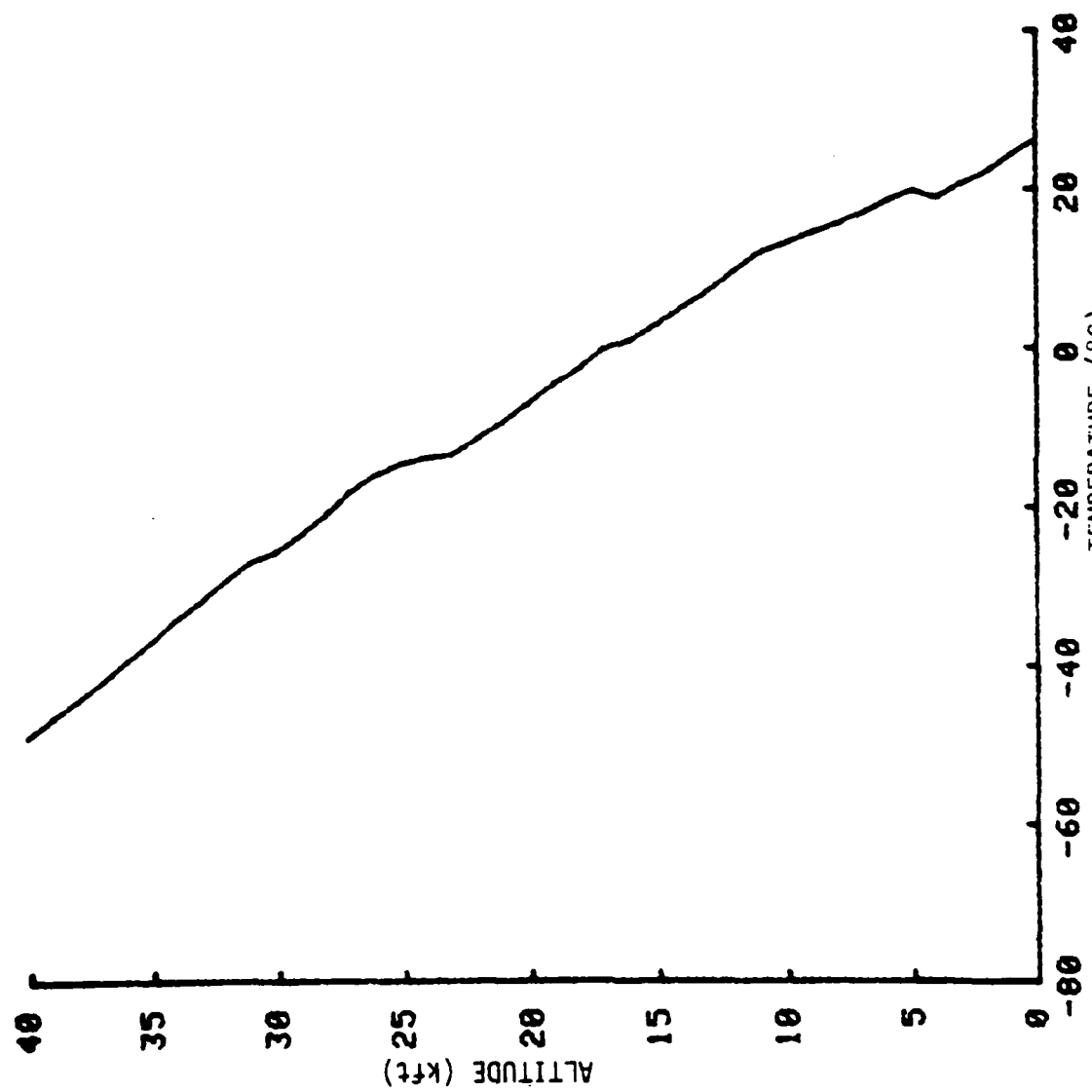


FIGURE C-17. CASE 52 TEMPERATURE PROFILE

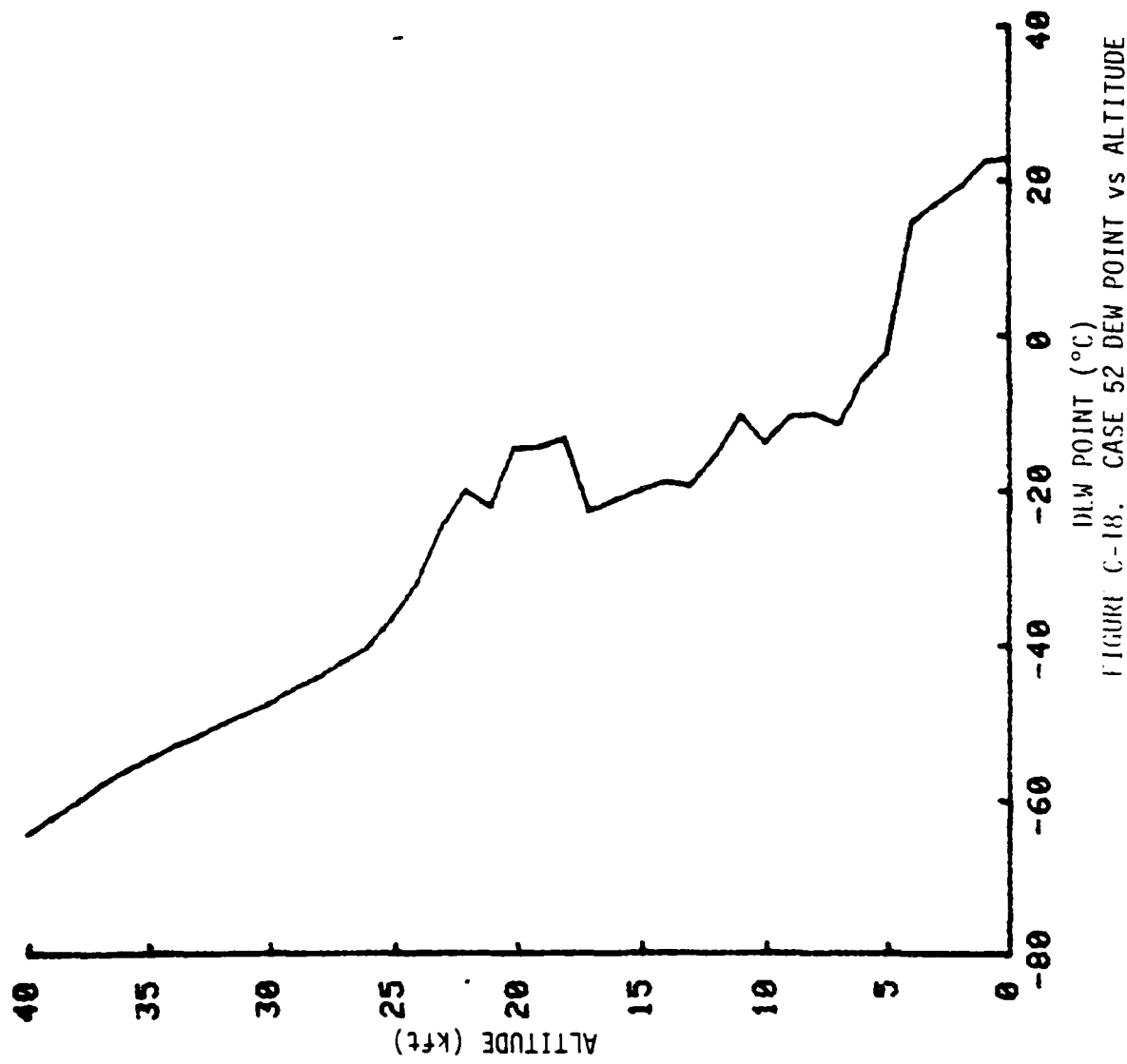


FIGURE C-18. CASE 52 DEW POINT vs ALTITUDE

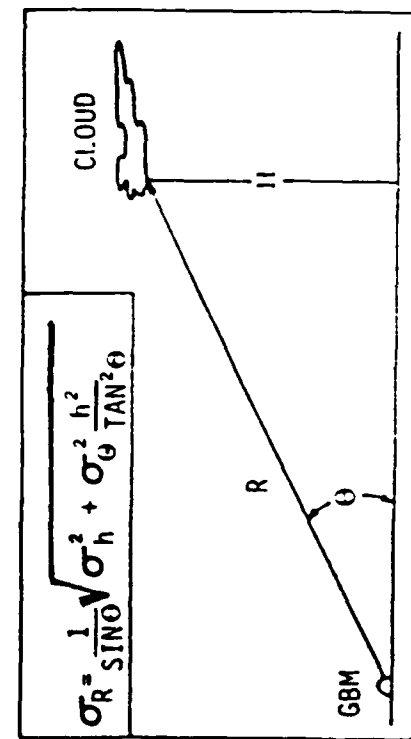
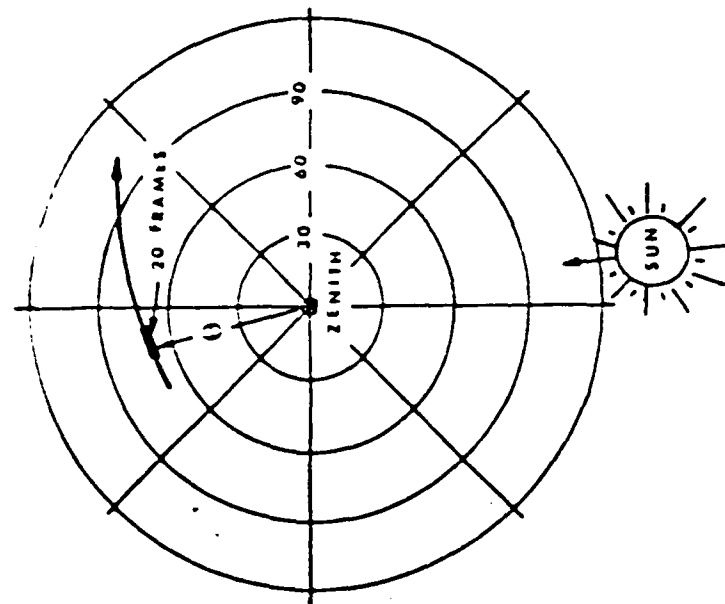
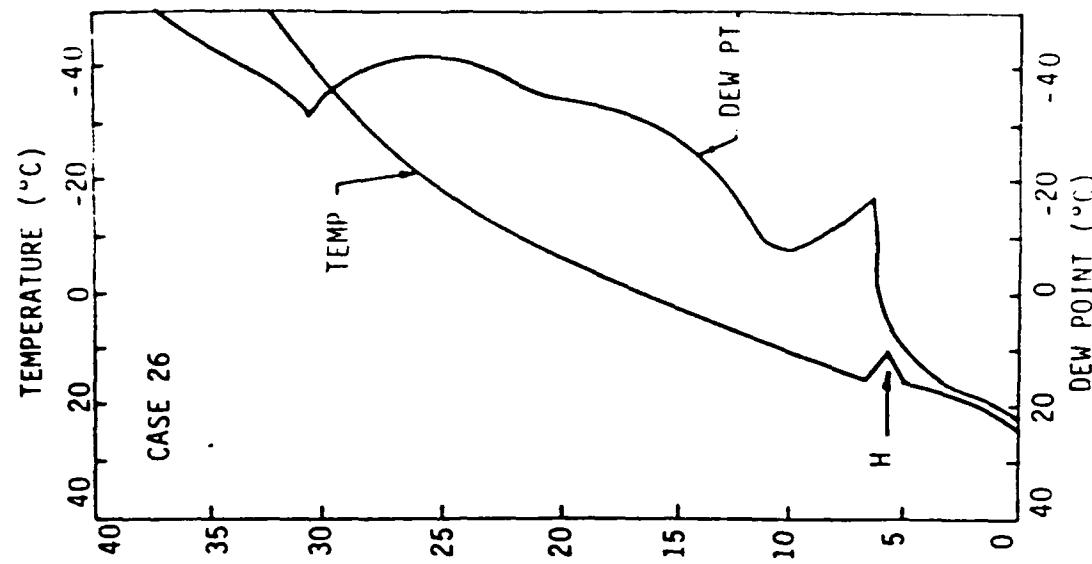


FIGURE C-19. CLOUD RANGE ESTIMATION

## **APPENDIX D. GEOMETRY**

This appendix contains polar plots (Figures D-1 through D-8) of the boresight track and sun position for the cases of interest. The plot center represents the sensor position and the boresight zenith. Each bold circle represents a declination of 10 deg from the zenith, with the horizontal represented by a dashed line. The sun position is also shown on those cases for which it appears less than 108 deg from the zenith.

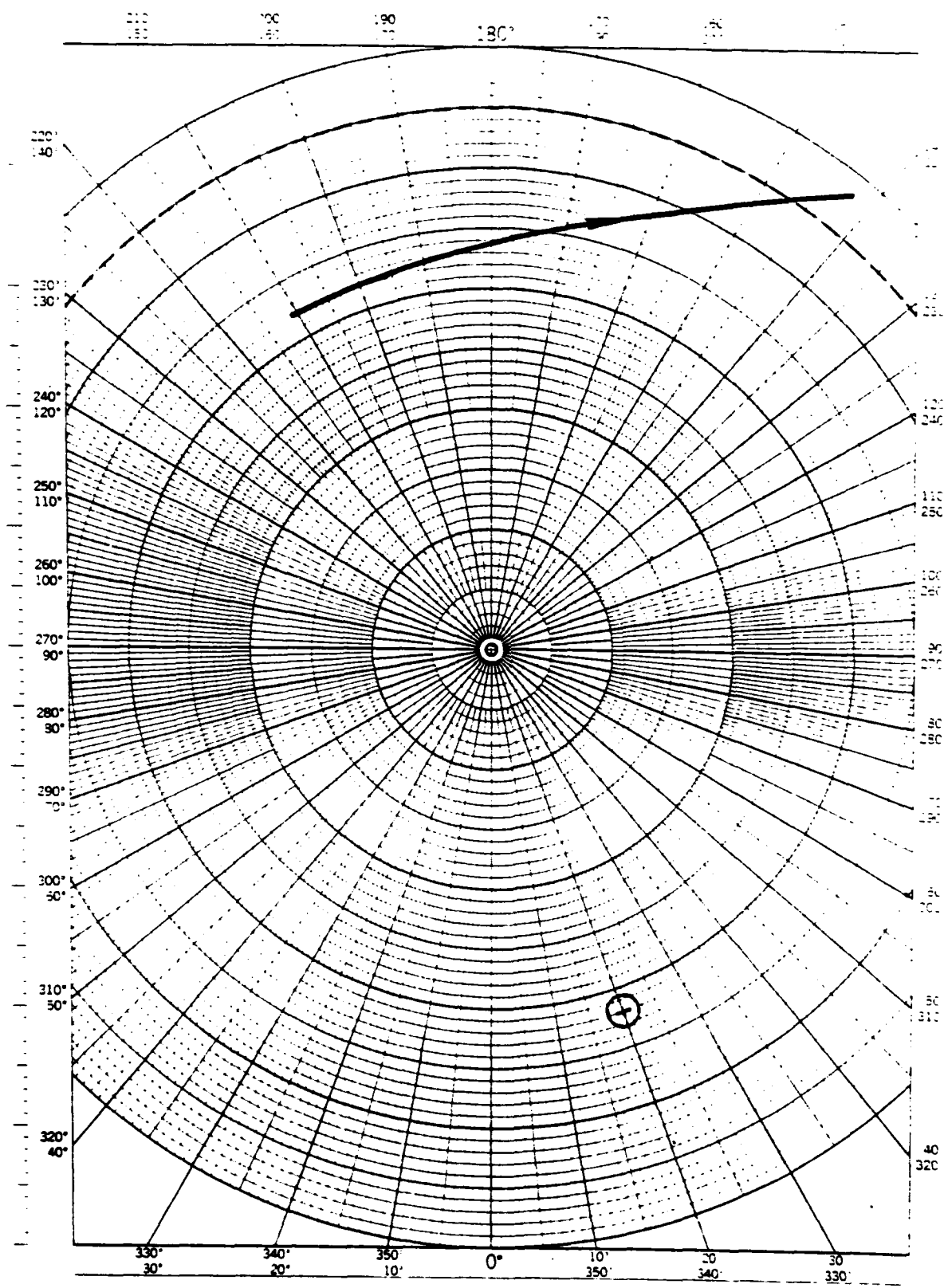


FIGURE D-1. BORESIGHT TRAJECTORY, CASE 26

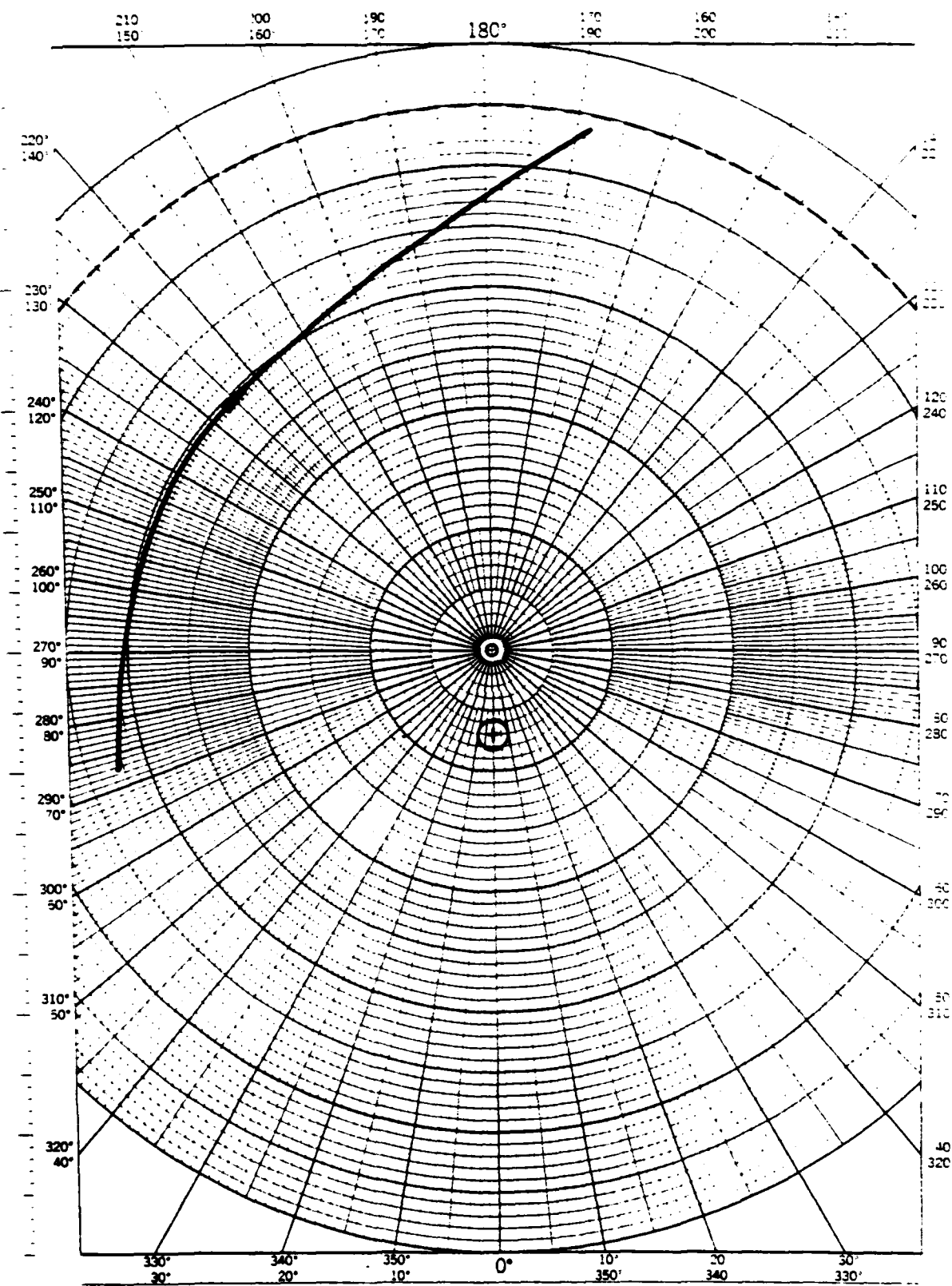


FIGURE D-2. BORESIGHT TRAJECTORY, CASE 30

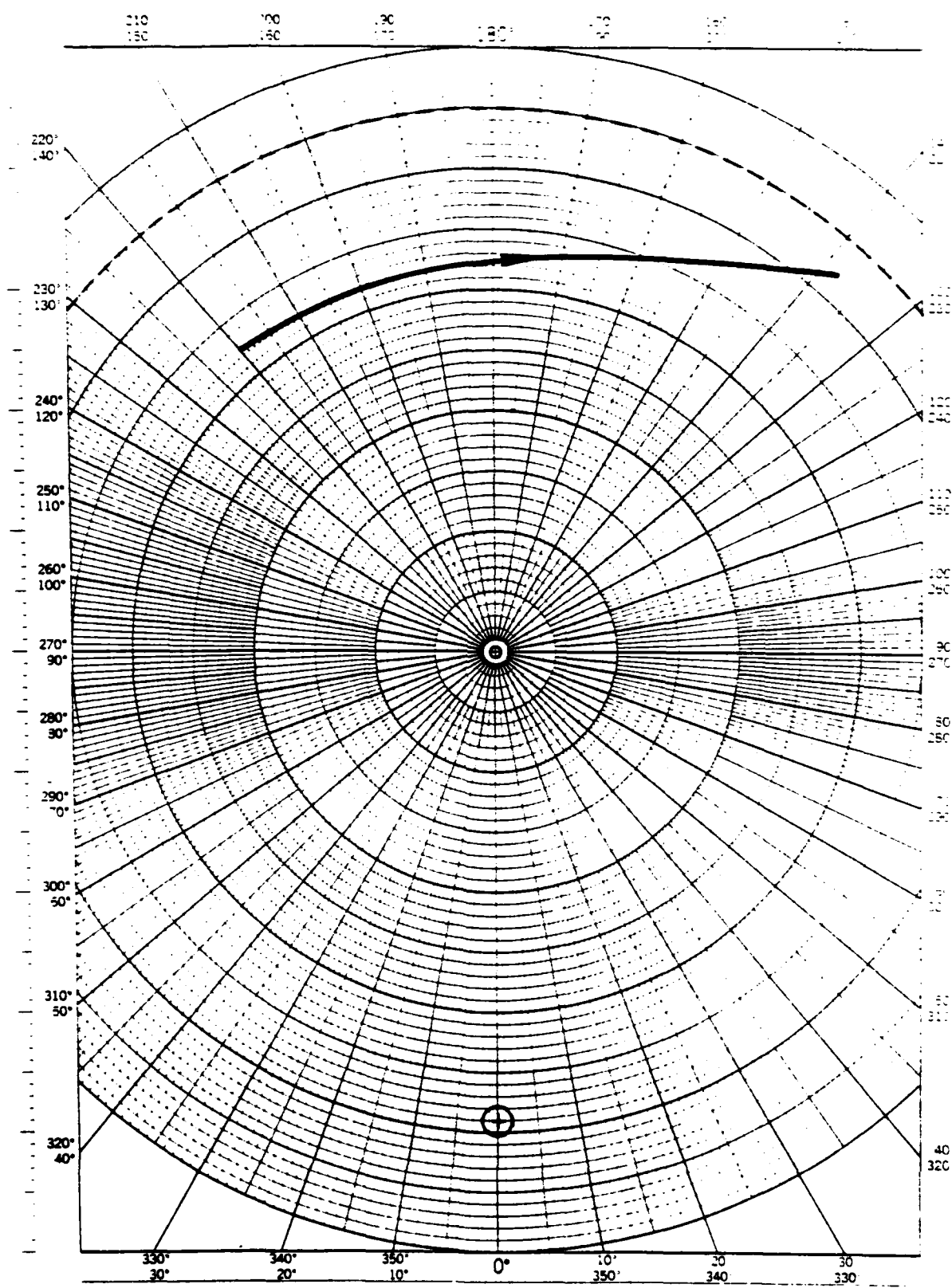
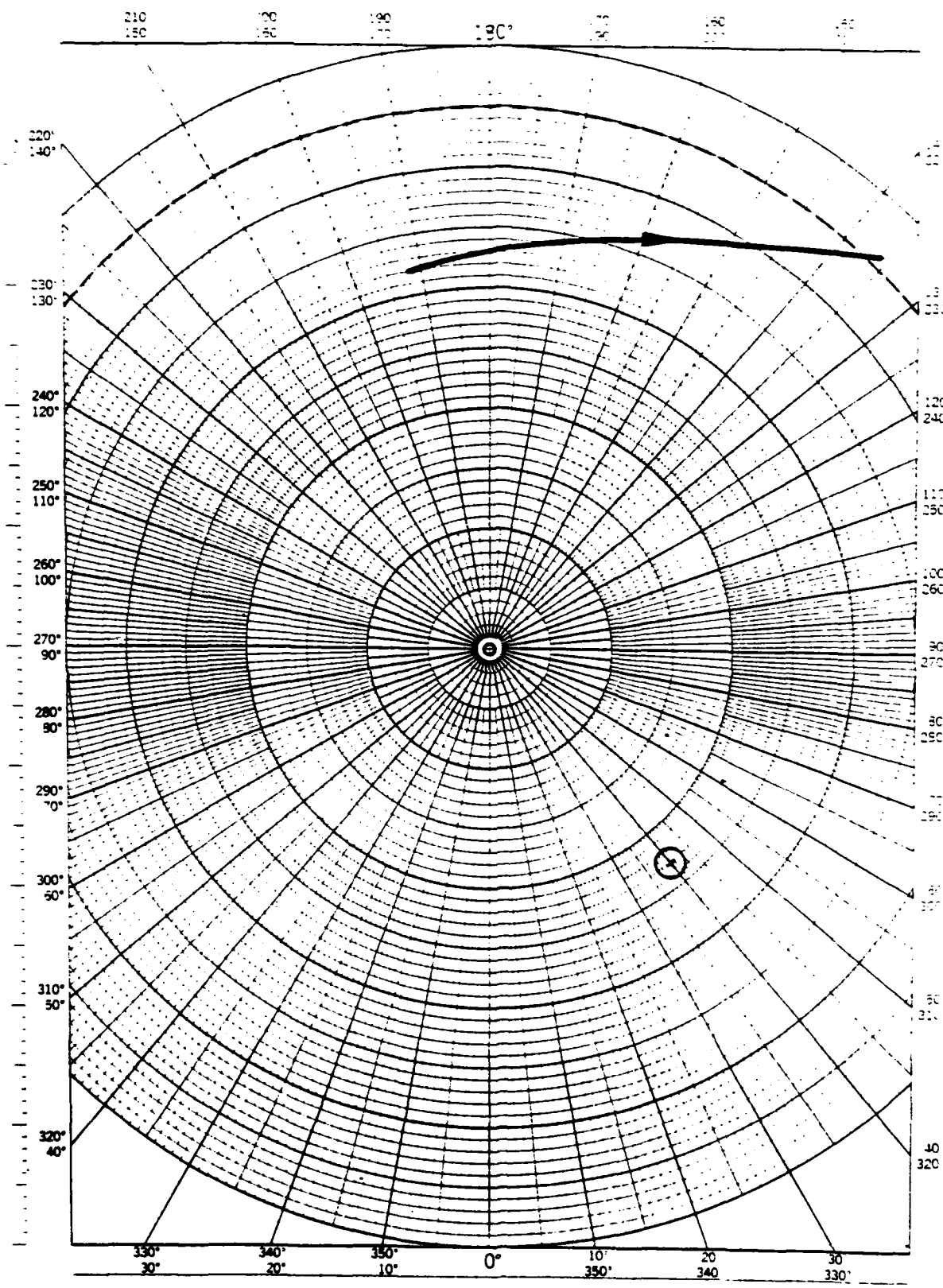


FIGURE D-3. BORESIGHT TRAJECTORY, CASE 32



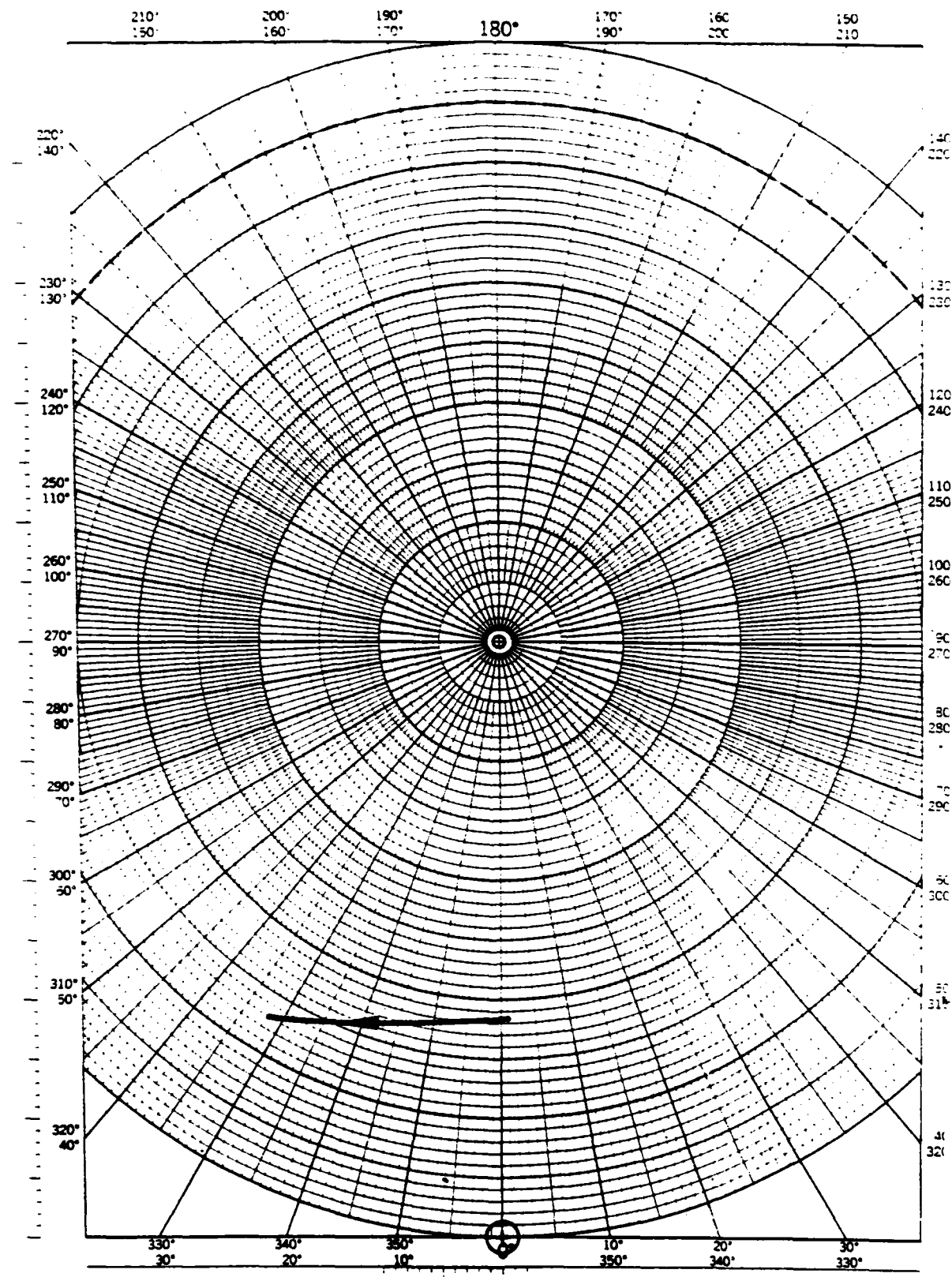


FIGURE D-5. BORESIGHT TRAJECTORY, CASE 46

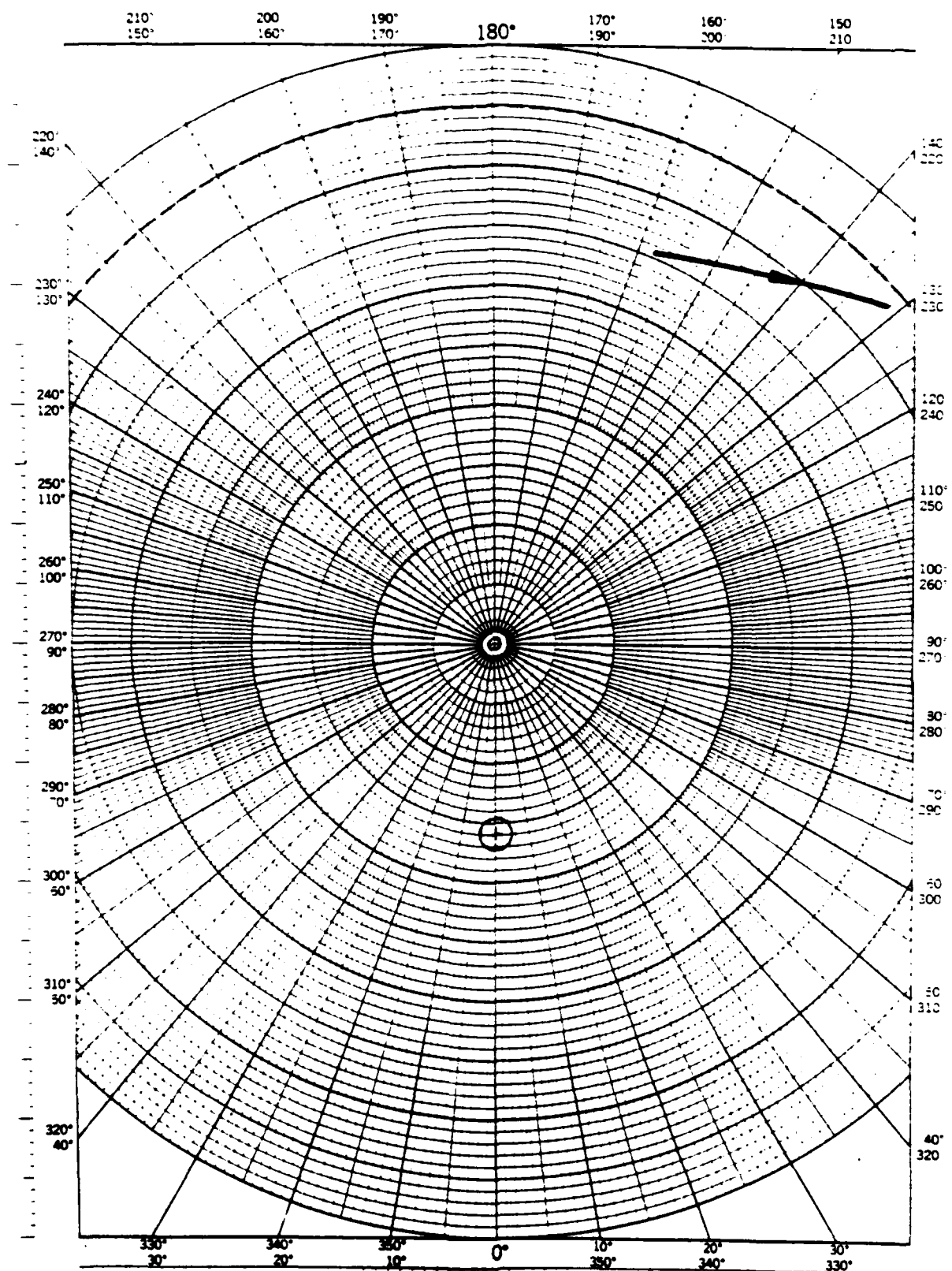


FIGURE D-6. BORESIGHT TRAJECTORY, CASE 49

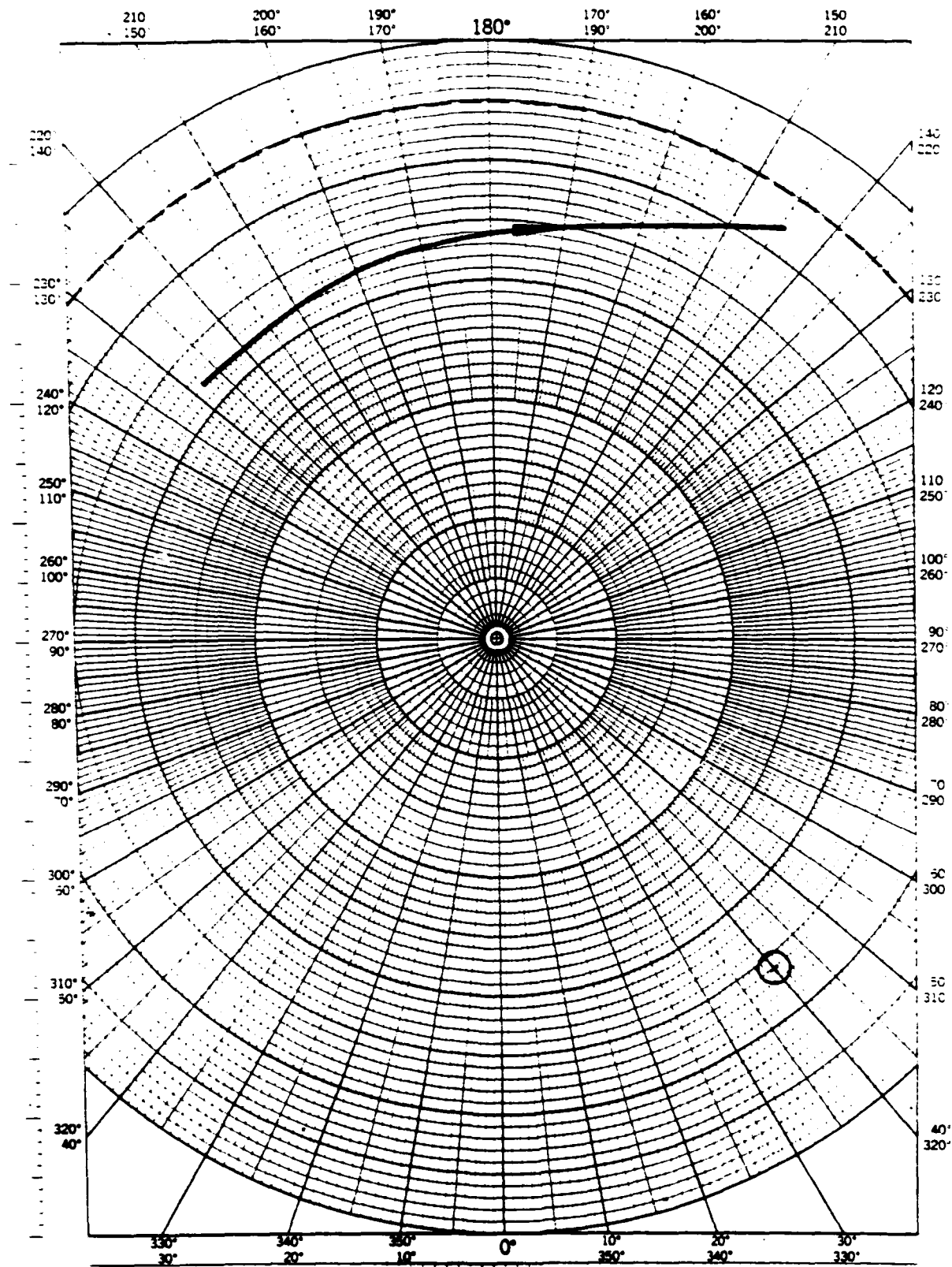


FIGURE D-7. BORESIGHT TRAJECTORY, CASE 51

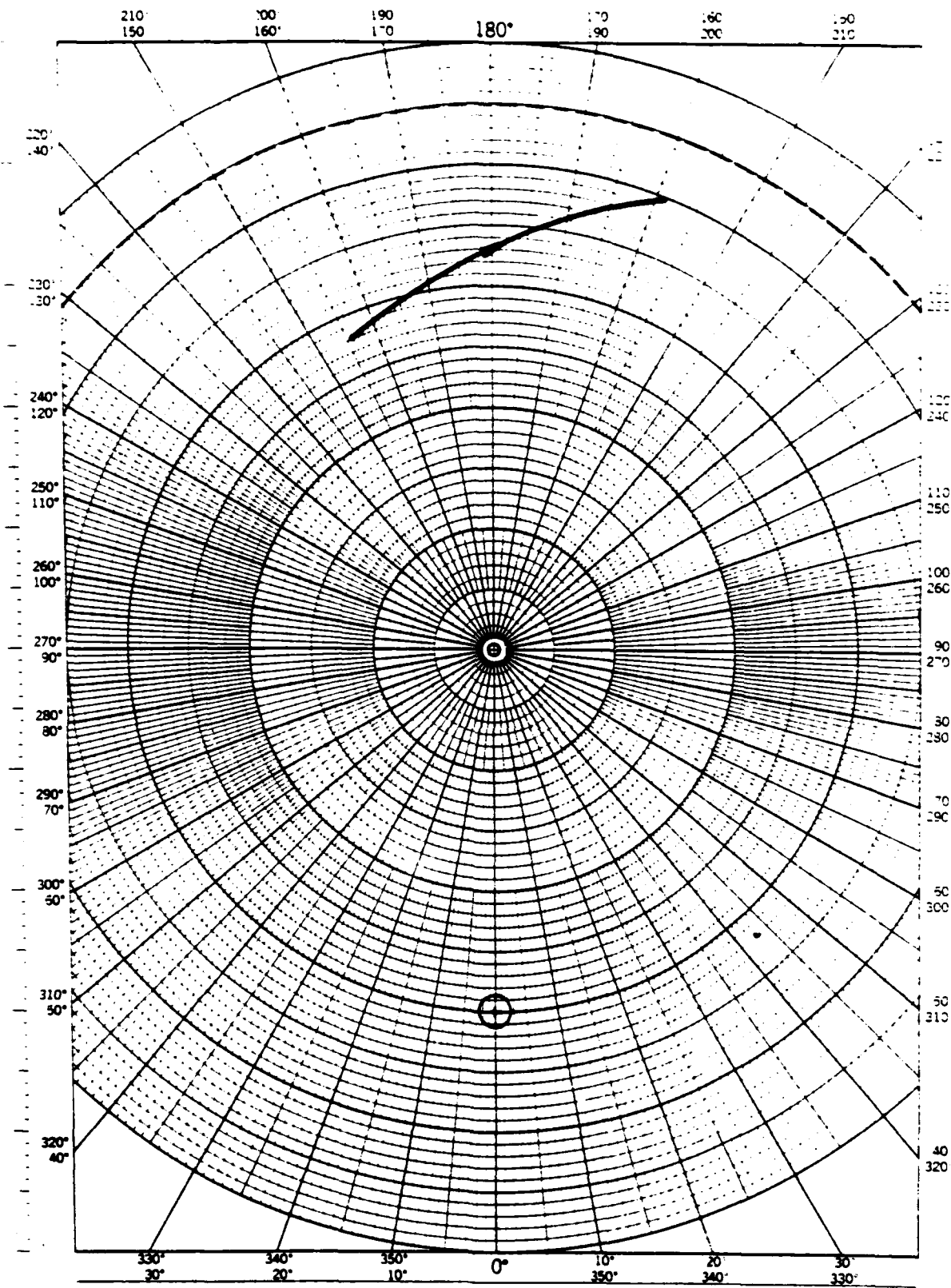


FIGURE D-8. BORESIGHT TRAJECTORY, CASE 60